Supporting Information for:

Network-Forming Liquids from Metal–Bis(acetamide) Frameworks with Low Melting Temperatures

*Mengtan Liu, Ryan D. McGillicuddy, Hung Vuong, Songsheng Tao, Adam H. Slavney, Miguel I. Gonzalez, Simon J. L. Billinge, Jarad A. Mason**

*E–mail: mason@chemistry.harvard.edu

J. Am. Chem. Soc.

List of Contents

Materials and Methods

Anhydrous diethyl ether and acetonitrile were obtained from a Pure Process Technology anhydrous solvent system. Anhydrous methanol and ethanol were purchased from a commercial vendor and used as received. *N*,*N*′-1,4-butylenebis(acetamide) (bba) was synthesized following a procedure adapted from a previous report.[1] All other reagents were purchased from commercial vendors and used as received. For any reactions performed under a N_2 atmosphere, organic ligands were first dried by heating to above 60 °C for at least 6 hours. Mechanochemistry syntheses was conducted using a MM 400 Retsch ball mill. Differential scanning calorimetry (DSC) experiments were performed using a TA Instruments DSC2500. Thermogravimetric analysis (TGA) experiments were performed using a TA Instruments TGA550. Powder X-ray diffraction data was collected using a Bruker D2 Phaser benchtop powder X-ray diffraction instrument. Single crystal diffraction data at 100 K and ambient temperature was collected using a Bruker D8, SMART APEX II, APEX DUO instrument or using the synchrotron X-ray source at ChemMatCARS at the Advanced Photon Source, Argonne National Laboratory. Variable-temperature viscosity measurements were performed using a Kyoto Electronics Electromagnetically Spinning Viscometer (EMS-1000S). IR spectra were obtained on a Bruker ALPHA II Platinum ATR with a variable temperature stage. NMR spectra were collected on a Varian Mercury NMR operating at 500 MHz.

Synthesis of Metal–Bis(acetamide) Networks

Synthesis of *N*,*N*′-1,4-butyelenebis(acetamide) (bba)

N,*N*′-butylenebis(acetamide) (bba) was synthesized following a procedure adapted from a previous report.[1] Specifically, CuO (495 mg, 6.2 mmol), 1,4-diaminobutane (1.0 mL, 10 mmol), acetonitrile (MeCN, 1.6 mL, 30 mmol), and H_2O (1.1 mL, 60 mmol) were combined in a Teflon autoclave under a N_2 atmosphere. The sealed autoclave was then heated in an oven at 180 °C with rotation for at least 3 h. After cooling to room temperature, the resulting mixture was thoroughly washed with chloroform to extract the organic components. The resulting light brown solution was the passed through a thin layer of silica and the solvent was removed under reduced pressure to obtain a yellow solid mixture of bba and acetamide. Acetamide was removed via sublimation (50–60 °C, high vacuum, 2–4 h), yielding pure bba as a light-yellow powder (950 mg, 60% yield). The successful synthesis of the bba ligand is confirmed by ^{1}H NMR spectrum (Figure S50). ^{1}H NMR (500 mHz, DMSO): δ/ppm 7.8 (s, 2H), 3.0 (dt, J = 7.0, 5.6 Hz, 4H), 1.8 (s, 6H), 1.4 (m, 4H). TGA indicates that any residual CuO is less than 0.23 mol % (see Figure S26)

Synthesis of M(hmba)$_3$[MX$_4$]

Co(hmba)$_3$[Co(NCS)$_4$] was synthesized following a procedure adopted from a previous report.[2] Specifically, $Co(NCS)_2$ (58.3 mg, 0.33 mmol) was dissolved in 2 mL of warm ethanol (EtOH) in a 20-mL scintillation vial. In a 100-mL round-bottom flask, *N*,*N*′-1,6-hexamethlyenebis(acetamide) (hmba; 200.3 mg, 1 mmol) was dissolved in a solution of 1 mL of EtOH, 1 mL of 2,2-dimethoxypropane (DMP), and 10 mL of ethyl acetate (EtOAc) under stirring and reflux. The metal solution was then added dropwise to the reaction flask. After addition, a small amount of a

blue oil formed on the wall of the reaction flask, which was dissolved back into the reaction mixture by adding 12 mL of nitromethane to obtain a blue solution. After cooling to ambient temperature, slow evaporation yielded dark blue crystals over a period of 2–4 days. The crystals were removed from the mother liquor, thoroughly washed with diethyl ether (Et_2O), and stored in fresh Et_2O until further characterization. The successful synthesis of the framework was confirmed by comparing the unit cell parameters determined from single crystal X-ray diffraction (SCXRD) and X-ray powder diffraction pattern to those previously reported (Table S4, Figure S8). For DSC experiments, crystals were removed from Et_2O, dried and then hermetically sealed under a N_2 atmosphere.

$Co(hmba)_3[CoBr_4]$ was synthesized following a procedure adapted from a previous report.[3] Specifically, $CoBr_2$ (150.5 mg, 0.7 mmol) was dissolved in 4 mL of warm ethanol (EtOH) in a 20-mL scintillation vial. In a 100-mL round-bottom flask, hmba (266.7 mg, 1.3 mmol) was dissolved in 3 mL of EtOH and 27 mL of EtOAc under stirring and reflux. The metal solution was then added dropwise to the reaction flask and a clear, blue solution was obtained. After cooling to ambient temperature, slow evaporation over 12 h yielded large purple crystals, which were determined to be isostructural to a the previously reported 3-D $Co(hmba)_3(CoCl_4)\cdot 2EtOH$ framework by SCXRD (Table S4). The crystals were then removed from the mother liquor, washed thoroughly with Et_2O, and transferred to a new vial. The head space of the vial was purged with N_2, capped, and stored at ambient temperature. Over 1–2 weeks, the lattice EtOH was released (see Figure S49), and single crystallinity was lost. Unit cell parameters determined by indexing and Le Bail refinement of PXRD patterns show that the resulting solvent-free structure is isostructural to the previously reported 2-D framework $Mn(hmba)_3(MnBr_4)$[3] (Figures S11, S12; Table S11). For DSC experiments, samples were hermetically sealed under a N_2 atmosphere.

$Mn(hmba)_3[MnBr_4]$ was synthesized following a procedure adapted from a previous report.[3] Specifically, $MnBr_2\cdot 4H_2O$ (143.4 mg, 0.5 mmol) was suspended in 2 mL of warm methanol (MeOH) in a 20-mL scintillation vial. In a 100-mL round-bottom flask, hmba (300.4 mg, 1.5 mmol) was dissolved in 1.5 mL of EtOH and 13.5 mL of EtOAc in a 100 mL round bottle flask under stirring and reflux. The metal suspension was then added to the ligand solution dropwise. An off-white precipitate was formed immediately and remained insoluble upon the addition of 12 mL of nitromethane. After stirring for 1–2 h, the reaction mixture was allowed to cool to ambient temperature. The precipitate was filtered, washed thoroughly with Et_2O, dried and sealed under a N_2 atmosphere. The successful formation of the 2-D $Mn(hmba)_3(MnBr_4)$ framework was confirmed by powder X-ray diffraction (Figures S11, S12; Table S11). For DSC experiments, samples were hermetically sealed under a N_2 atmosphere.

$Mn(hmba)_3[MnCl_4]$. $MnCl_2$ (41.5 mg, 0.33 mmol) was dissolved in 2 mL of warm MeOH in a 20-mL scintillation vial. In a second 20-mL scintillation vial, hmba (200.3 mg, 1 mmol) was dissolved in 5 mL of warm EtOH. The metal solution was added to the hmba solution dropwise while stirring, and a clear, colorless solution was obtained. After cooling to ambient temperature, vapor diffusion of Et_2O yielded colorless crystals over 2–4 days, which were determined to be isostructural to a previously reported framework 3-D $Co(hmba)_3(CoBr_4)\cdot 2EtOH$ framework by SCXRD (Table S4). The crystals were then isolated by decanting the supernatant and washing thoroughly with Et_2O. The head space of the vial was purged with N_2, capped, and stored at ambient temperature. Over 1–2 weeks, the lattice EtOH was released, and single crystallinity was

lost. Unit cell parameters determined by indexing and Le Bail refinement of PXRD patterns show that the resulting solvent-free structure is isostructural to the previously reported 2-D $Mn(hmba)_3(MnBr_4)$ framework (Figures S11, S12; Table S11). For DSC experiments, samples were hermetically sealed under a N_2 atmosphere.

Synthesis of $M(bba)_3[M'X_4]$

$Mn(bba)_3[MnCl_4]$. $MnCl_2$ (25.1 mg, 0.2 mmol) was dissolved in 3 mL of warm MeOH in a 20-mL scintillation vial under a N_2 atmosphere. In a second 20-mL scintillation vial, bba (103.3 mg, 0.6 mmol) was dissolved in 8 mL of warm MeCN. The metal solution was then added dropwise to the ligand solution at 60 °C and stirred for 0.5–2 h. After cooling the resulting pale-yellow solution to ambient temperature, vapor diffusion of Et_2O yielded clear, pale yellow crystals overnight. The crystals were then removed from the mother liquor, washed thoroughly with Et_2O, and stored in fresh Et_2O. For DSC experiments, crystals were dried under flowing N_2 and hermetically sealed under a N_2 atmosphere.

$Mn(bba)_3[ZnCl_4]$. $MnCl_2$ (12.5 mg, 0.1 mmol) was dissolved in 1 mL of warm MeOH in a 20-mL scintillation vial and $ZnCl_2$ (13.5 mg, 0.1 mmol) was dissolved in 1 mL of warm EtOH in a separate 20-mL scintillation vial. Both solutions were combined, then added dropwise to a 20-mL scintillation vial containing bba (51.5 mg, 0.3 mmol) dissolved in 6 mL of warm MeCN. The metal solution was then added dropwise to the ligand solution at 60 °C and stirred for 0.5–2 h. After stirring for 0.5–2 h, the resulting pale-yellow solution was cooled to ambient temperature. Vapor diffusion of Et_2O yielded clear, pale yellow crystals overnight. The crystals were then removed from the mother liquor, washed thoroughly with Et_2O, and stored in fresh Et_2O. For DSC experiments, crystals were dried under flowing N_2 and hermetically sealed under a N_2 atmosphere.

$Co(bba)_3[CoCl_4]$. $CoCl_2$ (26.0 mg, 0.2 mmol) was dissolved in 2 mL of warm EtOH in a 20-mL scintillation vial under a N_2 atmosphere. In a second 20-mL scintillation vial, bba (51 mg, 0.3 mmol) was dissolved in 4 mL of warm MeCN. The metal solution and 1 mL of MeOH was then added dropwise to the ligand solution sequentially at 60 °C and stirred for 0.5–2 h. After cooling the resulting blue solution to ambient temperature, vapor diffusion of Et_2O yielded blue crystals over 3–4 days. The crystals were then removed from the mother liquor, washed thoroughly with Et_2O, and stored in fresh Et_2O. For DSC experiments, crystals were dried under flowing N_2 and hermetically sealed under a N_2 atmosphere.

$Fe(bba)_3[FeCl_4]$. $FeCl_2$ (25.4 mg, 0.2 mmol) was dissolved in 2 mL of warm EtOH and 1 mL of warm MeOH in a 20-mL scintillation vial under a N_2 atmosphere. In a second 20-mL scintillation vial, bba (51.5 mg, 0.3 mmol) was dissolved in 4 mL of warm MeCN. The metal solution was then added dropwise to the ligand solution at 60 °C and stirred for 0.5–2 h. After cooling the resulting pale-yellow solution to ambient temperature, vapor diffusion of Et_2O yielded clear, pale yellow crystals over 2–3 days. The crystals were then removed from the mother liquid, washed thoroughly with Et_2O, and stored in fresh Et_2O. For DSC experiments, the crystals were dried under flowing N_2 and hermetically sealed under a N_2 atmosphere..

$Mg(bba)_3[M'Cl_4]$ (M' = Co, Zn). Under a N_2 atmosphere, $MgCl_2$ (9.5 mg, 0.1 mmol) was dissolved in 1 mL of warm MeOH in a 20-mL scintillation vial. $CoCl_2$ or $ZnCl_2$ (13.5 mg, 0.1

mmol) was dissolved in 1 mL of warm EtOH in a separate 20-mL scintillation vial, and then both solutions were combined and added dropwise to a solution of bba (51.5 mg, 0.3 mmol) dissolved in 5–6 mL of warm MeCN at 60 °C. A precipitate formed initially but soon redissolved upon stirring. A light blue (M′ = Co) or light yellow (M′ = Zn) solution was obtained and stirred for 0.5 h. After cooling to ambient temperature, vapor diffusion of Et_2O yielded clear, pale blue (M′ = Co) or off-white (M′ = Zn) crystals overnight. The crystals were then removed from the mother liquor, washed thoroughly with Et_2O, and stored in fresh Et_2O. The identity of the metal in the cationic framework is determined to be Mg by SCXRD. The fact that Mg outcompetes Co and Zn to form M–O is consistent with a stronger Mg–O bond strength. For DSC experiments, the crystals were dried under flowing N_2 and hermetically sealed under a N_2 atmosphere. Note that larger batch to batch variations were observed in the DSC baseline for $Mg(bba)_3[M'Cl_4]$ relative to other bis(amide)-networks, but ΔH_{fus} values for the melting endotherm vary by less than 3% for 3 representative batches.

Synthesis of $M(bba)_3X_2$

$Co(bba)_3Br_2$ was synthesized following a procedure adapted from a previous report.[3] Specifically, $CoBr_2$ (43.6 mg, 0.2 mmol) was dissolved in 4 mL of warm MeCN and 4 mL of warm DMP in a 20-mL scintillation vial. In a second scintillation vial, bba (103.3 mg, 0.6 mmol) was dissolved in 6 mL of warm MeCN. The metal solution was then added dropwise to the ligand solution at ~60 °C and stirred for 0.5–2 h. The resulting clear blue solution was allowed to cool to ambient temperature, and slow evaporation of the reaction solvent yielded purple crystals in 12–24 h. For DSC experiments, the crystals were dried under flowing N_2 and hermetically sealed under a N_2 atmosphere.

$Mg(bba)_3Cl_2$. To avoid the formation of solvent-containing network, $Mg(bba)_3Cl_2$ was synthesized via mechanochemistry. Specifically, a 5-mL stainless steel cell was loaded with one 7-mm diameter stainless steel milling ball, $MgCl_2$ (19.4 mg, 0.2 mmol), bba (103.3 mg, 0.6 mmol), and MeCN (20 μL). The milling cell was sealed under a N_2 atmosphere and then milled for 99 minutes at 30 Hz in a MM 400 Retsch ball mill. The milling cell was opened under a N_2 atmosphere, and the resulting powder was dried under vacuum at 60 °C for at least 6 h. For DSC experiments, samples were hermetically sealed under a N_2 atmosphere. The crystal structure was determined by SCXRD of a single crystal obtained after one heating and cooling cycle on DSC.

Additional Mechanochemical Syntheses

In addition to solution crystallizations, $Co(hmba)_3[Co(NCS)_4]$, $Mn(hmba)_3[MnCl_4]$, and $Mn(bba)_3(MnCl_4)$ were also successfully synthesized via mechanochemistry, which was beneficial for scaling up syntheses. In a typical mechanochemistry reaction, a 5-mL stainless steel cell with one 7-mm diameter stainless steel milling balls was loaded with $Co(NCS)_2$ (52.5 mg, 0.3 mmol), hmba (93.13 mg, 0.3 mmol), and EtOH (17.5 μL) for the synthesis of $Co(hmba)_3[Co(NCS)_4]$; $MnCl_2$ (125.8 mg, 1 mmol), hmba (300.2 mg, 1.5 mmol), and EtOH (46 μL) for the synthesis of $Mn(hmba)_3[MnCl_4]$; and $MnCl_2$ (49.34 mg, 0.4 mmol), bba (103.3 mg, 0.6 mmol), and MeCN (20 μL) for the synthesis of $Mn(bba)_3[MnCl_4]$. The milling cell was sealed under a N_2 atmosphere and then milled for 99 minutes at 30 Hz in a MM 400 Retsch ball mill. The milling cell was opened under a N_2 atmosphere, and the resulting powders were dried under vacuum at 40–60 °C for at

least 6 h. For DSC experiments, samples were hermetically sealed under a N_2 atmosphere. The successful formation of each phase was confirmed by PXRD and DSC (Figures S15, S24).

General Comments on Stability of Solid Metal–Bis(acetamide) Networks
All metal–bis(acetamide) compounds reported here can be manipulated in air and are not sensitive to oxygen based on PXRD. For instance, we observed no changes to the PXRD pattern of $Fe(bba)_3[FeCl_4]$ over multiple measurements taken over a 30 min period (Figure S10). The compounds are highly stable in nonpolar common solvents, such as Et_2O and hexane, and are typically stored in Et_2O after synthesis. Due to the weak coordination strength between the metal and neutral bis(acetamide) ligand, compounds are soluble in large excesses of polar solvents, such as water and many alcohols. Extensive exposure to humid air (on the order of days to weeks depending on the humidity and sample) can lead to structural changes and/or degradation, but the compounds are generally stable for handling on the benchtop for several hours.

X-ray Crystallography

X-ray diffraction analyses were performed on a single crystal coated with Paratone-N oil and mounted on a MiTeGen microloops. The intensities of the reflections were primarily collected by a Bruker D8 diffractometer with CMOS area detector or APEX II diffractometer with CCD area detector ($Mo_{K\alpha}$ radiation, λ = 0.71073 Å).

For unit cell determination, the crystal was either cooled to 100 K or held at 298 K using an Oxford Cryosystems nitrogen cryostream. The collection method for all crystals involved 0.5° scans in ω at 20° in 2θ°, with 60 frames being collected. Data integration was carried out using SAINT V8.37A with reflection spot size optimization.[4] The 100 K unit cell parameters were primarily used to confirm the successful synthesis of previously reported phases. The 298 K unit cell parameters were used to calculate crystallographic densities, which were used to convert gravimetric ΔH_{fus} (J/g) into volumetric ΔH_{fus} (kJ/L) (Table S14).

For structure determination, crystals were cooled to 100 K or held at 298 K using an Oxford Cryosystems nitrogen cryostream. The collection method for structures determined with the Bruker D8 diffractometer with CMOS area detector involved 0.5° scans in ω and φ at 12° in 2θ°. An additional φ fast scan was collected when necessary. The collection method for structures determined with APEX II diffractometer with CCD area detector involved 0.5° scans in ω and φ at 26 or 28° in 2θ°.

For crystals that diffracted weakly using our home $Mo_{K\alpha}$ radiation source at 298 K, the diffractions were collected at ChemMatCARS at the Advanced Photon Source, Argonne National Laboratory using synchrotron radiation (λ = 0.41328 Å) on a Huber three circles diffractometer with Pilatus 1M(CdTe) detector. The collection method for all crystals involved 0.5° scans in φ at 0° in 2θ°.

Reflection data collected at 100 and 298 K were analyzed similarly. Data integration was carried out down to ≤ 0.84 Å resolution using SAINT V8.37A with reflection spot size optimization. Most crystals were either single or merohedrally twinned and absorption corrections were made with the program SADABS. All single crystal structures were solved using Intrinsic Phasing method in SHELXT-2014, and all merohedrally twinned structures were solved using the Direct method in

SHELXS.[5, 6] All structures were refined by least-square methods using SHELXL-2014.[7] Structure solution and refinement was done in the OLEX 2 interface.[8] After the initial solution and refinement, when applicable, the twin law for merohedral twinning was found using the TwinRotMat routine in Platon and applied in subsequent refinements. No significant crystal decay was observed during data collection. Thermal parameters were refined anisotropically for all non-hydrogen atoms. Hydrogen atoms were placed geometrically and refined using a riding model for all structures.

Crystallographic Tables and Ellipsoid Plots

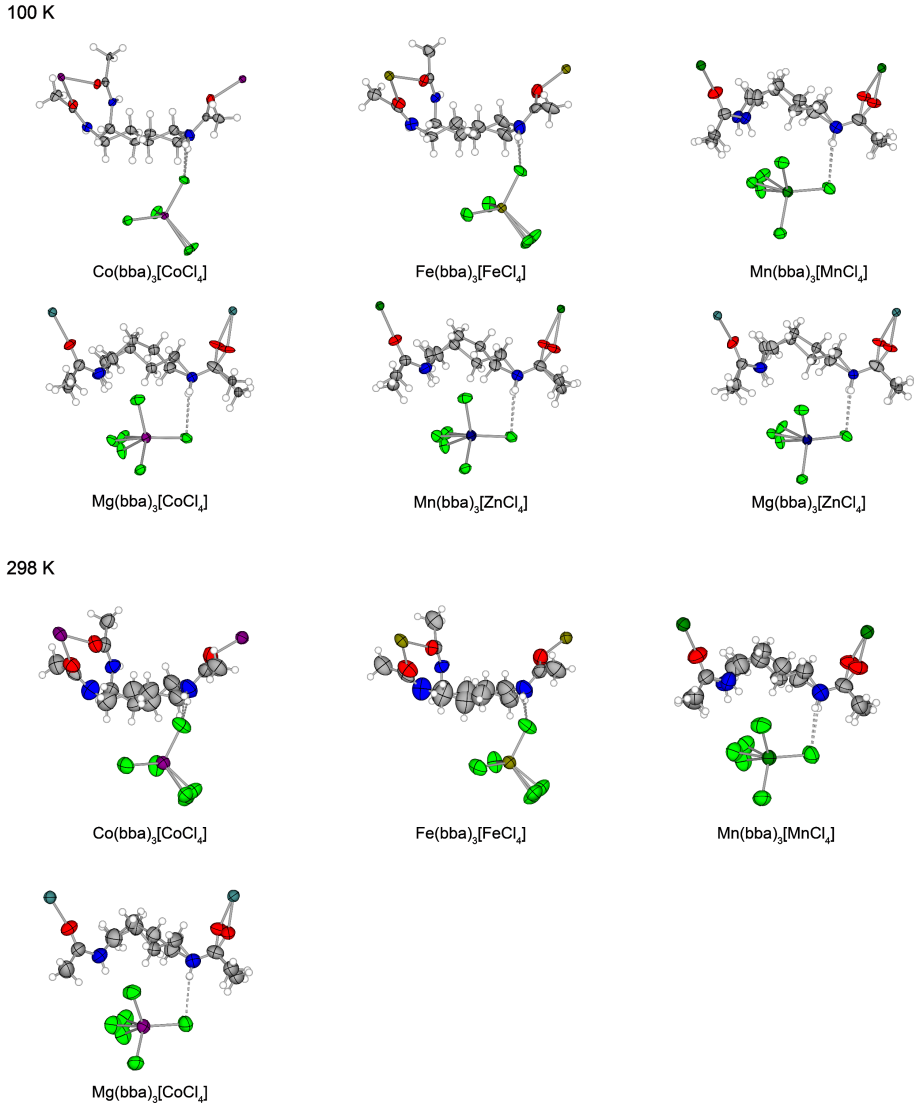

Figure S1. Atomic displacement parameters of the asymmetric unit cell of $M(bba)_3[M'Cl_4]$ at 100 K and ambient temperature drawn at a 50% probability level as determined by single-crystal X-ray diffraction. Purple, brown, green, teal, dark blue, green, red, blue, grey, represent Co, Fe, Mn, Mg, Zn, Cl, O, N, and C atoms, respectively. Hydrogen atoms (white spheres) are refined by allowing them to ride on the C and N atoms they attached to, and their atomic displacement parameters are omitted for clarity. The bba ligand is modeled as disordered over two positions with combined occupancy of 1. While 3 out of the 4 Cl atoms in the MCl_4 are symmetry related, the crystallographically independent Cl is modeled as disordered near a special position over 3 positions, each with individual occupancy of 0.33.

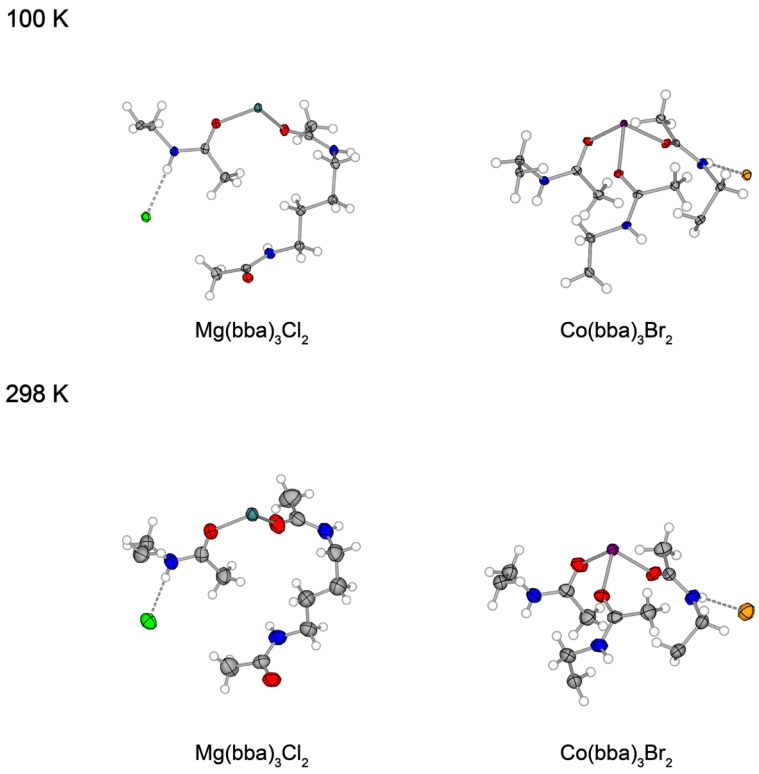

Figure S2. Atomic displacement parameters of the asymmetric unit cells of $M(bba)_3X_2$ at 100 K and ambient temperature drawn at 50% probability level as determined by single-crystal X-ray diffraction. Purple, teal, yellow, green, red, blue, and grey ellipsoids represent Co, Mg, Br, Cl, O, N, and C atoms, respectively. Hydrogen atoms (white spheres) are refined by allowing them to ride on C and N atoms they attached to, and their atomic displacement parameters are omitted for clarity.

Table S1. Crystallographic data for M(bba)$_3$[M′Cl$_4$] networks collected at 100 K.

	Co(bba)$_3$[CoCl$_4$]	**Fe(bba)$_3$[FeCl$_4$]**	**Mn(bba)$_3$[MnCl$_4$]**	**Mn(bba)$_3$[ZnCl$_4$]**	**Mg(bba)$_3$[CoCl$_4$]**	**Mg(bba)$_3$[ZnCl$_4$]**
Formula	$C_{24}H_{48}Cl_4Co_2N_6O_6$	$C_{24}H_{48}Cl_4Fe_2N_6O_6$	$C_{24}H_{48}Cl_4Mn_2N_6O_6$	$C_{24}H_{48}Cl_{4.04}MnN_6O_6Zn$	$C_{24}H_{48}Cl_4CoMgN_6O_6$	$C_{24}H_{48}Cl_4MgN_6O_6Zn$
Temperature (K)	100(2)	100(2)	100(2)	100(2)	100(2)	100(2)
Crystal System	Cubic	Cubic	Cubic	Cubic	Cubic	Cubic
Space Group	$Pa\bar{3}$	$Pa\bar{3}$	$Pa\bar{3}$	$Pa\bar{3}$	$Pa\bar{3}$	$Pa\bar{3}$
a, b, c (Å)	19.2085(4)	19.2987(8)	19.2293(5)	19.1651(9)	19.0748(10)	19.0532(8)
α, β, γ (°)	90	90	90	90	90	90
V (Å^3)	7088.3(12)	7187.6 (9)	7110.3(5)	7039.4(10)	6940.3(11)	6916.8(5)
Z	8	8	8	8	8	8
Radiation, λ (Å)	MoKα, 0.71073	MoKα, 0.71073	MoKα, 0.71073	MoKα, 0.71073	MoKα, 0.71073	MoKα, 0.71073
2Θ Range for Data Collection (°)	4. 742 to 50.008	4. 730 to 54.246	5.19 to 50.052	4.752 to 50.026	4.776 to 50.02	4.78 to 50.03
Completeness to 2Θ	99.9% (2Θ = 50.008°)	99.9% (2Θ = 50.482°)	99.9% (2Θ = 50.052°)	99.9% (2Θ = 50.026°)	99.9% (2Θ = 50.02°)	99.9% (2Θ = 50.03°)
Data / Restraints / Parameters	2094 / 10 / 180	2657 / 16 / 176	2103 / 4 / 163	2170 / 50 / 162	2145/ 54 /1 68	2139 / 6 / 155
Goodness of Fit on F^2	1.159	1.141	1.077	1.071	1.221	1.230
R_1[a], wR_2[b] (I>2σ(I))	0.0382, 0.0749	0.0694, 0.1444	0.0577, 0.0963	0.0389, 0.0825	0.0591, 0.1079	0.0643, 0.1192
R_1[a], wR_2[b] (all data)	0.0417, 0.0762	0.0762, 0.1478	0.1004, 0.1143	0.0480, 0.0872	0.0616, 0.1088	0.0699, 0.1213
Largest Diff. Peak and Hole (e Å^{-3})	0.41 and –0.58	0.97 and –0.58	0.37 and –0.30	0.30 and –0.31	0.31 and –0.29	0.28 and –0.36

[a] $R_1 = \sum||F_o| - |F_c||/\sum|F_o|$. [b] $wR_2 = \{\sum[w(F_o^2 - F_c^2)^2]/\sum[w(F_o^2)^2]\}^{1/2}$.

Table S2. Crystallographic data for $M(bba)_3[M'Cl_4]$ networks collected at ambient temperature

	$Co(bba)_3[CoCl_4]$	**$Fe(bba)_3[FeCl_4]$**	**$Mn(bba)_3[MnCl_4]$**	**$Mg(bba)_3[CoCl_4]$**
Formula	$C_4H_{48}Cl_4Co_2N_6O_6$	$C_4H_{48}Cl_4Co_2N_6O_6$	$C_4H_{48}Cl_4Mn_2N_6O_6$	$C_4H_{48}Cl_4CoMgN_6O_6$
Temperature (K)	298 (2)	298 (2)	298(2)	298(2)
Crystal System	Cubic	Cubic	Cubic	Cubic
Space Group	$Pa\bar{3}$	$Pa\bar{3}$	$Pa\bar{3}$	$Pa\bar{3}$
a, b, c (Å)	19.3687(11)	19.4549(8)	19.447(5)	19.2933(15)
α, β, γ (°)	90	90	90	90
V (Å^3)	7266.1(12)	7363.5(9)	7354(6)	7181.6(17)
Z	8	8	8	8
Radiation, λ (Å)	Synchrotron, 0.41328	MoKα, 0.71073	Synchrotron, 0. 41328	Synchrotron, 0.41328
2Θ Range for Data Collection (°)	2.118 to 31.542	4.682 to 52.774	1.722 to 30.328	1.736 to 28.796
Completeness to 2Θ	100.0% (2Θ = 28.714°)	100.0% (2Θ = 28.714°)	100.0% (2Θ = 28.714°)	100.0% (2Θ = 28.714°)
Data / Restraints / Parameters	2895 / 102 / 194	2518 / 86 / 177	2735 / 379 / 209	3294 / 175 / 178
Goodness of Fit on F^2	1.087	1.054	1.078	1.085
R_1[a], wR_2[b] (I>2σ(I))	0.0430, 0.1301	0.0553 0.1498	0.0473, 0.1582	0.0362, 0.1033
R_1[a], wR_2[b] (all data)	0.0467, 0.1351	0.0640, 0.1614	0.0516, 0.1650	0.0381, 0.1061
Largest Diff. Peak and Hole (e Å^{-3})	0.46 and –0.27	0.43 and –0.23	0.26 and –0.26	0.26 and –0.37

[a] $R_1 = \sum||F_o| - |F_c||/\sum|F_o|$. [b] $wR_2 = \{\sum[w(F_o^2 - F_c^2)^2]/\sum[w(F_o^2)^2]\}^{1/2}$.

Table S3. Crystallographic data for $M(bba)_3X_2$ networks collected at 100 K and ambient temperature.

	$Co(bba)_3Br_2$	**$Co(bba)_3Br_2$**	**$Co(bba)_3Br_2$**	**$Mg(bba)_3Cl_2$**	**$Mg(bba)_3Cl_2$**
Formula	$C_4H_{48}Br_2Co N_6O_6$	$C_4H_{48}Br_2Co N_6O_6$	$C_4H_{48}Br_2Co N_6O_6$	$C_{24}H_{48}Cl_2Mg N_6O_6$	$C_{24}H_{48}Cl_2Mg N_6O_6$
Temperature (K)	100(2)	298(2)	298(2)	100(2)	298(2)
Crystal System	Triclinic	Triclinic	Triclinic	Triclinic	Triclinic
Space Group	$P\bar{1}$	$P\bar{1}$	$P\bar{1}$	$P\bar{1}$	$P\bar{1}$
a (Å)	8.0052(6)	8.0084(8)	8.0007(6)	8.9644(8)	9.0827(8)
b (Å)	9.8297(7)	10.2263(10)	10.2177(9)	9.0475(8)	9.2069(8)
c (Å)	10.7700(8)	10.8308(9)	10.8249(2)	11.1149(10)	11.1253(9)
α (°)	68.122(2)	67.490(2)	67.486(2)	110.220(2)	106.289(2)
β (°)	84.246(2)	83.681(2)	83.647(2)	107.068(2)	110.657(2)
γ (°)	82.492(2)	85.812(2)	85.742(2)	95.235(2)	95.804(2)
V (Å^3)	778.47(10)	811.97(14)	811.97(12)	789.79(12)	814.58(12)
Z	1	1	1	1	1
Radiation, λ (Å)	MoKα, 0.71073	MoKα, 0.71073	Synchrotron, 0. 41328	MoKα, 0.71073	MoKα, 0.71073
2Θ Range for Data Collection (°)	4.842 to 53.536	4.088 to 55.752	2.378 to 34.484	4.166 to 56.55	4.166 to 52.044
Completeness to 2Θ	99.9% (2Θ = 50.484°)	100.0% (2Θ = 50.484°)	91.6% (2Θ = 28.714°)	100% (2Θ = 50.484°)	100% (2Θ = 50.484°)
Data / Restraints / Parameters	3313 / 0 / 181	3893 / 0 / 181	4507 / 0 / 190	3910 / 0 / 181	3214 / 0 / 181
Goodness of Fit on F^2	1.046	1.028	1.112	1.019	1.072
R_1[a], wR_2[b] (I>2σ(I))	0.0240, 0.0458	0.0275, 0.0665	0.0360, 0.1033	0.0392, 0.0935	0.0458, 0.1235
R_1[a], wR_2[b] (all data)	0.00328, 0.0483	0.0370, 0.0702	0.417, 0.1069	0.0503, 0.0994	0.0615, 0.1341
Largest Diff. Peak and Hole (e Å^{-3})	0.58 and –0.36	0.44 and –0.36	0.94 and –0.47	0.41 and –0.23	0.75 and –0.20

[a] $R_1 = \sum||F_o| - |F_c||/\sum|F_o|$. [b] $wR_2 = \{\sum[w(F_o^2 - F_c^2)^2]/\sum[w(F_o^2)^2]\}^{1/2}$.

Table S4. Crystallographic unit cell data confirming successful network syntheses.

	$Co(hmba)_3[Co(NCS)_4]$ experimental	**$Co(hmba)_3[Co(NCS)_4]$ reported**[2]	**$Co(hmba)_3[CoBr_4]\cdot 2EtOH$ experimental**	**$Mn(hmba)_3[MnCl_4]\cdot 2EtOH$ experimental**	**$Co(hmba)_3[CoCl_4]\cdot 2EtOH$ reported**[3]
Temperature (K)	100(2)	293	100(2)	100(2)	293
Crystal System/Bravais lattice	Triclinic P	Triclinic P	Monoclinic C	Monoclinic C	Monoclinic C
a (Å)	11.432(4)	11,528(3)	24.424 (4)	24.397(4)	23.864(3)
b (Å)	11.432(4)	11.791(4)	10.8886(18)	10.975(7)	11.3010(13)
c (Å)	19.820(8)	20.334(4)	20.176(4)	20.125(4)	20.3262(11)
α (°)	93.68(2)	94.01(2)	90	90	90
β (°)	103.58(2)	103.75(2)	102.228(10)	102.70(10)	103.446
γ (°)	111.959(18)	111.80(2)	90	90	90
V (Å^3)	2375.3(17)	2453.08	5243.9(17)	5257(4)	5327.44
Radiation, λ (Å)	MoKα, 0.71073	MoKα, 0.71073	MoKα, 0.71073	MoKα, 0.71073	MoKα, 0.71073
2Θ Range for cell measurement(°)	7.558 to 50.034	N/A	6.080 to 44.794	6.309 to 41.541	N/A
# of reflection used	168	N/A	159	118	N/A

Table S5. Crystallographic unit cell data for density calculations.

	$Mn(bba)_3[ZnCl_4]$	**$Mg(bba)_3[ZnCl_4]$**
Temperature (K)	298(2)	298(2)
Crystal System/Bravais lattice	Cubic P	Cubic P
a, *b*, *c* (Å)	19.339(3)	19.267(2)
α, β, γ (°)	90	90
V (Å^3)	7233(3)	7152.6(8)
Radiation, λ (Å)	MoKα, 0.71073	MoKα, 0.71073
2Θ Range for cell measurement(°)	4.708 to 48.761	6.345 to 43.305
# of reflection used	757	220

Table S6. Comparison of unit cell volumes at 100 K and 298K for $M(bba)_3[M'Cl_4]$. 298K unit cell volume is used for the calculation of volumetric thermodynamic parameters. The density of all compounds are relatively similar at both temperatures. As such, differences in volume change upon melting should not be too drastic among them—assuming their liquid states also have relatively similar density—and likely have a minimal entropic effect, as an expansion or contraction as large as 10–15% would contribute ±5–10 J/mol·K to ΔS_{fus} for most organic molecules.[9,10]

Compound	V (Å^3) 100 K	V (Å^3) RT	% increase
$Mn(bba)_3[MnCl_4]$	7110	7354	3.4
$Mn(bba)_3[ZnCl_4]$	7039	7233	2.8
$Fe(bba)_3[FeCl_4]$	7188	7364	2.5
$Co(bba)_3[CoCl_4]$	7087	7266	2.5
$Mg(bba)_3[CoCl_4]$	6940	7182	3.4
$Mg(bba)_3[ZnCl_4]$	6916	7153	3.9

Table S7. Donor–acceptor (N···Cl) distances and bond angles for hydrogen bonds at 100 K and 298 K in $Co(bba)_3[CoCl_4]$, $Fe(bba)_3[FeCl_4]$, $Mn(bba)_3[MnCl_4]$, and $Mg(bba)_3[CoCl_4]$. Hydrogen bonds of "moderate" strength (donor–acceptor distance < 3.5 Å, bond angle > 120°)[11] are labeled in green. When two-part disorder is present, an average distance and angle weighted by relative occupancy is reported.

Compound	$T_{measurement}$		N1–H1···Cl1	N2–H2···Cl1
$Co(bba)_3[CoCl_4]$	100 K	D···A (Å)	3.368(4)	3.261(3)
		∠(DHA) (°)	128.7	167.3
$Fe(bba)_3[FeCl_4]$		D···A (Å)	3.323(6)	3.236(5)
		∠(DHA) (°)	134.5	165.2
$Mn(bba)_3[MnCl_4]$		D···A (Å)	3.707(5)	3.299(4)
		∠(DHA) (°)	124.09	161.6
$Mg(bba)_3[CoCl_4]$		D···A (Å)	3.696(7)	3.297(6)
		∠(DHA) (°)	127.2	160.5
$Co(bba)_3[CoCl_4]$	298 K	D···A (Å)	3.420(4)	3.288(3)
		∠(DHA) (°)	132.8	163.2
$Fe(bba)_3[FeCl_4]$		D···A (Å)	3.412(4)	3.270(3)
		∠(DHA) (°)	126.0	170.2
$Mn(bba)_3[MnCl_4]$		D···A (Å)	3.756(17)	3.329(12)
		∠(DHA) (°)	124.7	170.2
$Mg(bba)_3[CoCl_4]$		D···A (Å)	3.763(4)	3.342(3)
		∠(DHA) (°)	125.7	160.4

Table S8. Tabulation of (C5–C4–C3–N1) torsion angle φ at 100 K and 298 K for $Co(bba)_3[CoCl_4]$, $Fe(bba)_3[FeCl_4]$, $Mn(bba)_3[MnCl_4]$, and $Mg(bba)_3[CoCl_4]$. A ~170° larger φ is observed for Co and Fe analogs relative to Mn and Mg analogs.

Compound	$T_{measurement}$	φ(°)-part 1[a]	Occupancy-part 1	φ(°)-part 2[a]	Occupancy-part 2	φ(°)-Weighted Average
$Co(bba)_3[CoCl_4]$	100K	192	0.569	288	0.431	233
$Fe(bba)_3[FeCl_4]$		193	0.418	285	0.582	247
$Mn(bba)_3[MnCl_4]$		56	0.754	75	0.246	60
$Mg(bba)_3[CoCl_4]$		58	0.675	74	0.325	63
$Co(bba)_3[CoCl_4]$	298K	202	0.647	290	0.353	233
$Fe(bba)_3[FeCl_4]$		203	0.594	285	0.406	237
$Mn(bba)_3[MnCl_4]$		53	0.665	74	0.335	60
$Mg(bba)_3[CoCl_4]$		58	0.640	67	0.360	61

[a]Part 1 and part 2 refers to the two sets of disordered positions of the bba ligand.

The 170° difference in (C5–C4–C3–N1) torsion angle likely originates from a distortion of the metal octahedron, allowing the bba ligand to adapt a "staggered-like" geometry in the Co and Fe analogs, in contrast to the "eclipsed-like geometry" in the Mn and Mg analogs (Figure S1). Specifically, a ~3 times larger $\angle\sigma_{oct}$ (deviation in cis O–M–O angle from 90°) is found for Co and Fe centers relative to Mn and Mg centers in structures studied in this work (Table S9). Similar deviations in coordination complexes of first row transition metals have been attributed to asymmetrically occupied d orbitals as predicted by crystal field theory (electronic effect), as well as steric and packing effects.[12,13]

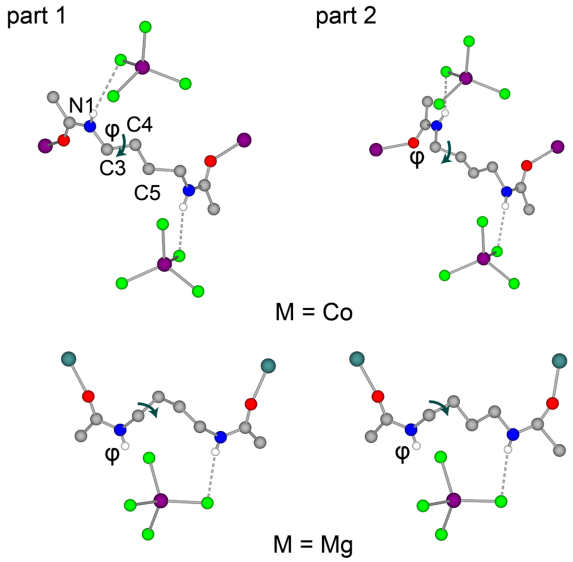

Figure S3. Selected portions of crystal structure demonstrating that the difference in the (C5–C4–C3–N1) torsion angle φ primarily accounts for the extra set of moderate hydrogen bonds in $Co(bba)_3[CoCl_4]$ (top), as the N1–H proton hydrogen bonds with $[CoCl_4]^{2-}$ in the next asymmetric unit. In contrast, in $Mg(bba)_3[CoCl_4]$ the distance from N1-H is much further from another Cl atom (bottom, Table S7). Each ligand was modeled with a two-part disorder, and both parts are shown here. Note that slight differences in other torsion angles within the polymethylene chains were observed, but these do not play a major role in dictating the hydrogen bonding geometry. Purple, blue, red, gray, blue, and green spheres represent Co, Mg, O, C, N, and Cl atoms, respectively. H atoms (other than N-H protons, white spheres) have been omitted for clarity.

Table S9. Cis O–M–O angles at 100 K and 298 K for $M(bba)_3[M'X_4]$ and $M(bba)_3X_2$. Within each series, the Co and Fe analogs (labeled in yellow) have O–M–O angle that deviate more substantially from 90° relative to Mn and Mg analogs, indicating a larger distortion from an ideal octahedron.

Compound	*T* (K)	∠(O–M–O)-1 (°)[a, b]	∠(O–M–O)-2 (°)	$\angle\sigma_{oct}$ (°)
$Co(bba)_3[CoCl_4]$	100	96.61(9)	83.39(9)	6.61(9)
$Fe(bba)_3[FeCl_4]$		96.13(17)	83.87(17)	6.13(17)
$Mn(bba)_3[MnCl_4]$		91.96(14)	88.04(14)	1.96(14)
$Mg(bba)_3[CoCl_4]$		91.74(16)	88.26(16)	1.74(16)
$Co(bba)_3Br_2$	100	93.7 (5)	86.3 (5)	3.7 (5)
$Mg(bba)_3Cl_2$		90.97(9)	89.03(9)	0.97(9)
$Co(bba)_3[CoCl_4]$	298	96.13(9)	83.87(9)	6.13(9)
$Fe(bba)_3[FeCl_4]$		95.69(13)	84.31(13)	5.69(13)
$Mn(bba)_3[MnCl_4]$		91.62(12)	88.38(12)	1.62(12)
$Mg(bba)_3[CoCl_4]$		91.49(9)	88.51(9)	1.49(9)
$Co(bba)_3Br_2$	298	94.18(24)	85.82(24)	4.18(24)
$Mg(bba)_3Cl_2$		91.2 (6)	88.8(6)	1.2(6)

[a]Two crystallographically independent metal sites are present in the cationic framework of $M(bba)_3[M'X_4]$ asymmetric unit cells. Since the disorder of one set of coordinating O atoms around one metal center complicates a comparison of the cis O–M–O angles, the ordered M–O octahedron is used for analysis here (Figure S4). Error reflects uncertainty from structure refinement.

[b]Three crystallographically independent oxygen atoms are present in the cationic framework of $M(bba)_3X_2$, and all three cis O–M–O angles larger than 90° are averaged to give ∠1, while angles smaller than 90° are averaged to give ∠2. Error reflects standard deviation from averaging and uncertainty from structure refinement.

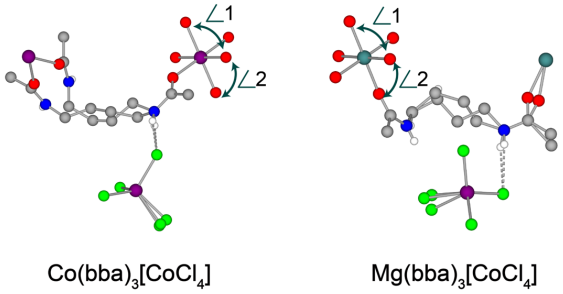

Figure S4. Select portions of crystal structures of $Co(bba)_3[CoCl_4]$ and $Co(bba)_3[MgCl_4]$ showing the metal centers and the cis O–M–O angles used for analysis in Table S9.

Comparison of atomic displacement parameters

Atomic displacement parameters (ADPs) obtained from crystal structure refinement describe the deviation of atoms from their equilibrium positions and can include contributions from residual molecular motion (vibrations, rotations) and static disorder (electron density distributed over two or more nearby sites).[14] Since static disorder creates configurational entropy and residual motion is related to vibrational and rotational entropy, ADPs can provide insight into solid-state entropy. As such, ADPs (or B-factors) have been compared across structures in structural biology and coordination chemistry, to provide insight into protein packing density and relative atomic motions due to Jahn-Teller distortions, respectively.[14, 15] Here, we compare equivalent isotropic displacement parameters (U_{equiv}) in two specific systems: 1) counteranion Cl atoms in the $M(bba)_3[M'X_4]$ compounds and 2) bba ligand atoms in $Co(bba)_3Br_2$ versus the $M(bba)_3[M'X_4]$ compounds. In both cases, trends in U_{equiv} generally agree with trends in ΔS_{fus}, providing insight into the molecular origin of entropy differences.

In order to compare U_{equiv} for Cl2 atoms in $M(bba)_3[M'X_4]$ (M = M′ = Mn, Fe, Co; M = Mg, M′ = Co), Cl2 was modelled both with 1) a freely-refined, single ellipsoid and 2) a symmetry-related 3-part disorder (3 symmetry-related positions, each with 1/3 occupancy). The disorder model slightly improves refinement statistics, but both models lead to similar conclusions with regards to residual motion and positional disorder. Specifically, the size of the single ellipsoid in the first model as well as the area spanned by the 3 disordered positions in the second model both show that Cl2 atoms in $Co(bba)_3[CoCl_4]$ have the least residual motion and/or positional disorder in the solid state, followed by Fe, Mg, Mn analogs (Figure S5).

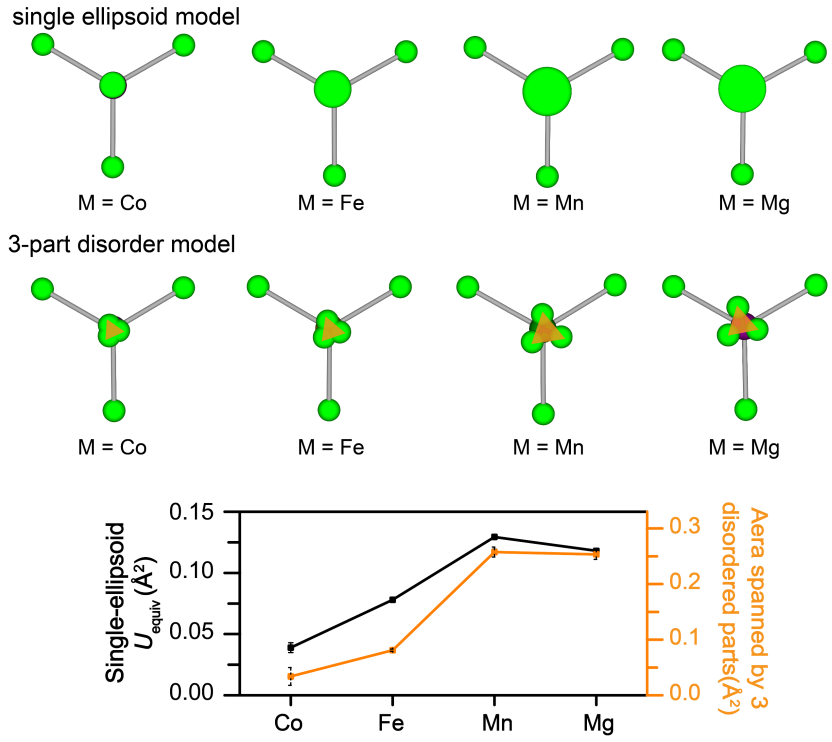

Figure S5. Top: Illustration of the $M'X_4$ counteranion in $M(bba)_3[M'X_4]$ (M = M′ = Mn, Fe, Co; M = Mg, M′ = Co) when Cl2 is refined in "single ellipsoid model" vs in "3-part disorder model" at 100 K. Ellipsoids are only shown for Cl2 atoms in the single ellipsoid model. Bottom: Plot showing correlation between U_{equiv} (equivalent isotropic displacement parameter) for Cl2 modeled as a single ellipsoid (black solid line) and the area spanned by the three Cl2 positions in the disorder model (orange solid line).

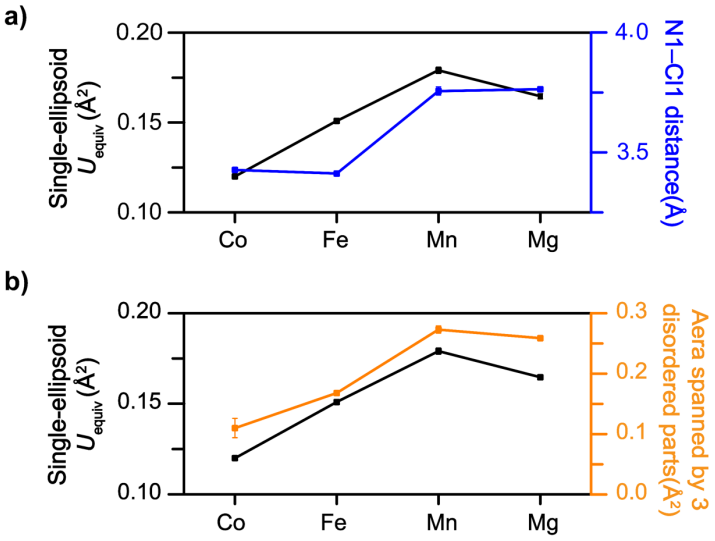

Figure S6. a) U_{equiv} of Cl2 atoms is correlated to N1-Cl1 distances at 298 K in $M(bba)_3[M'X_4]$ (M = M′ = Mn, Fe, Co; M = Mg, M′ = Co). b) Plot showing correlation between U_{equiv} (equivalent isotropic displacement parameter) for Cl2 modeled as a single ellipsoid (black solid line) and the area spanned by the three Cl2 positions in the disorder model (orange solid line) at 298 K. Note that 298 K and 100 K data were collected with two separate crystals and the same trend was observed in U_{equiv}, supporting the fact that the trend we are observing is intrinsic to the compounds and not due to variations in crystal quality.

U_{equiv} values of C, N, and O atoms in the bba ligands of $Mg(bba)_3Cl_2$, $Co(bba)_3Br_2$, and $M(bba)_3[M'Cl_4]$ were compared to similarly probe entropy differences due to residual motion and positional disorder. Care was taken to ensure that comparisons between U_{equiv} reflected intrinsic differences between compounds rather than differences due to crystal quality or data collection methods. Specifically, since the asymmetric unit cells of $M(bba)_3X_2$ and $M(bba)_3(M'Cl_4)$ compounds are different, U_{equiv} of the three sets of crystallographically independent O, N, C_a, C_b, C_c, C_d atoms in the asymmetric unit cell of $Mg(bba)_3Cl_2$ and $Co(bba)_3Br_2$ were averaged to yield one set of representative values. Correspondingly, only the half of the ligand that is actively engaged in forming moderate hydrogen bonds in all three $M(bba)_3[M'Cl_4]$ compounds is considered, which contains the same six atoms. In addition, while the ligand is well modeled without disorder in $Co(bba)_3Br_2$, a two-part disorder model best describes ligand electron density in $M(bba)_3[M'Cl_4]$. Therefore, an average weighted by occupancy was used for bba atoms in $M(bba)_3[M'Cl_4]$. At both 100 K and ambient temperature (Figure S7), U_{equiv} values for bba atoms in $Co(bba)_3Br_2$ are lower than those for $M(bba)_3[M'Cl_4]$. Moreover, data collected from two $Co(bba)_3Br_2$ crystals on different diffractometers resulted in U_{equiv} values that were within experimental uncertainties.

Table S10. U_{equiv} in the single-ellipsoid model and distances/area spanned by the three positions in the disorder model. Errors are from the uncertainties of the crystal structure refinement and propagated accordingly for area calculations.

Single-ellipsoid model		$Co(bba)_3[CoCl_4]$	$Fe(bba)_3[FeCl_4]$	$Mn(bba)_3[MnCl_4]$	$Mg(bba)_3[CoCl_4]$
U_{equiv} (Å^2) Cl2	100 K	0.0390(4)	0.078(1)	0.1294(10)	0.118(2)
	298 K	0.1200(6)	0.1509(13)	0.1792(17)	0.1646(14)
3-part disorder model		$Co(bba)_3[CoCl_4]$	$Fe(bba)_3[FeCl_4]$	$Mn(bba)_3[MnCl_4]$	$Mg(bba)_3[CoCl_4]$
Distance between the 3 positions (Å)	100 K	0.28(4)	0.433(4)	0.771(8)	0.765(8)
	298 K	0.504(16)	0.623(3)	0.794(5)	0.773(4)
Area spanned by the 3 positions (Å^2)	100 K	0.034(16)	0.0812(2)	0.257(9)	0.253(9)
	298 K	0.110(11)	0.168(3)	0.273(6)	0.259(4)

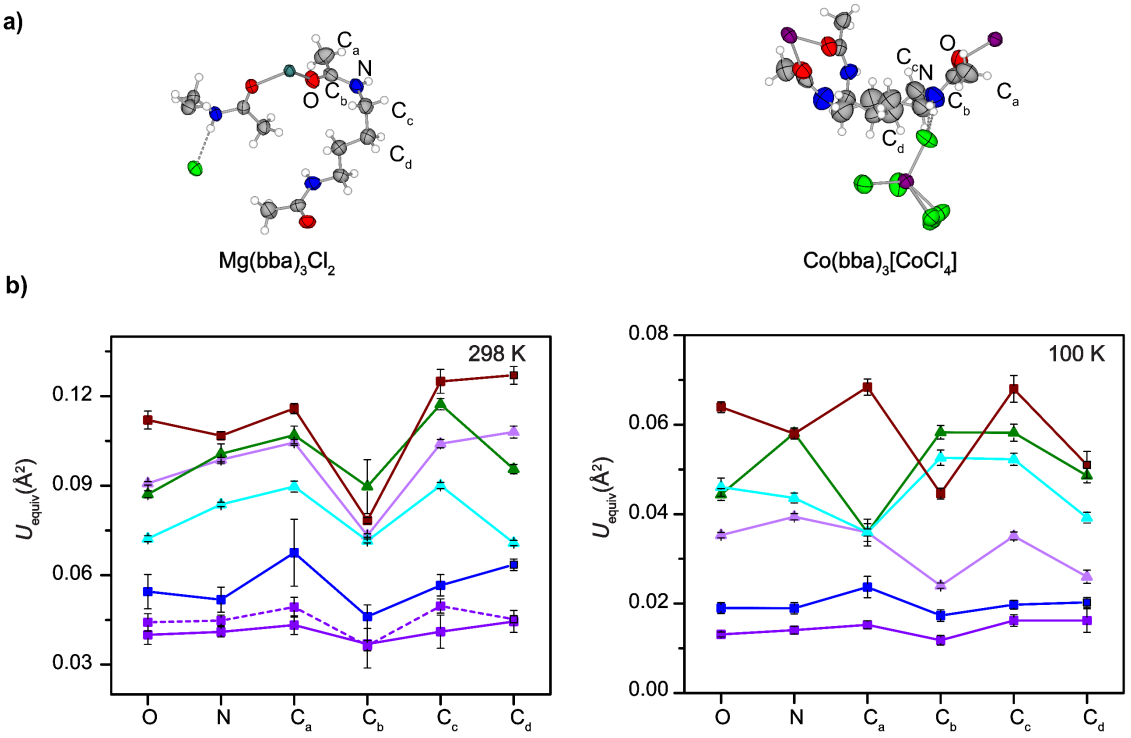

Figure S7. a) The asymmetric unit cell of $Mg(bba)_3Cl_2$ and $Co(bba)_3[CoCl_4]$ with thermal ellipsoids shown at 50% probability level demonstrating relevant atoms for U_{equiv} comparisons. Purple, red, gray, blue, green, and yellow ellipsoids represent Co, O, C, N, Cl, and Br atoms, respectively. Thermal ellipsoids for H atoms (white spheres) are omitted for clarity. b) Comparison of U_{equiv} for the bba ligand atoms in $Mg(bba)_3Cl_2$ (blue), $Co(bba)_3Br_2$ (purple) and $M(bba)_3[M'X_4]$ [M = M′ = Mn (green), Fe (dark red), Co (light purple); M = Mg, M′ = Co (light blue)] at 100 K and 298 K. Independent $Co(bba)_3Br_2$ crystals that were analyzed at the Advanced Photon Source with synchrotron radiation (dashed purple line) and on a laboratory diffractometer using MoK_α source (solid purple line) yielded near identical U_{equiv}. Note that error bars for data points in $Co(bba)_3Br_2$ contain contributions from both 1) standard deviation from averaging the three chains and 2) propagated uncertainties in U_{equiv} from the crystal structure refinement. Error bars for data points in $M(bba)_3[M'Cl_4]$ represented uncertainties (propagated when applicable) in U_{equiv} from the crystal structure refinement. At both temperatures, bba ligands in the $Mg(bba)_3Cl_2$ and $Co(bba)_3Br_2$ have notably lower U_{equiv} values.

Powder X-Ray Diffraction (PXRD)

Powder X-ray diffraction patterns were measured at ambient temperature using a D2 Phaser Bruker AXS diffractometer with $Cu_{K\alpha}$ radiation (λ = 1.5418 Å). When necessary, approximate unit cell dimensions were determined by using a standard peak search followed by indexing with a single value decomposition approach,[16] as implemented in TOPAS-Academic. The unit cell dimensions were then refined by performed a structureless Le Bail refinement in TOPAS-Academic.[17] When single crystals could not be obtained for a given phase, the unit cell volume from PXRD was used for crystallographic densities calculations.

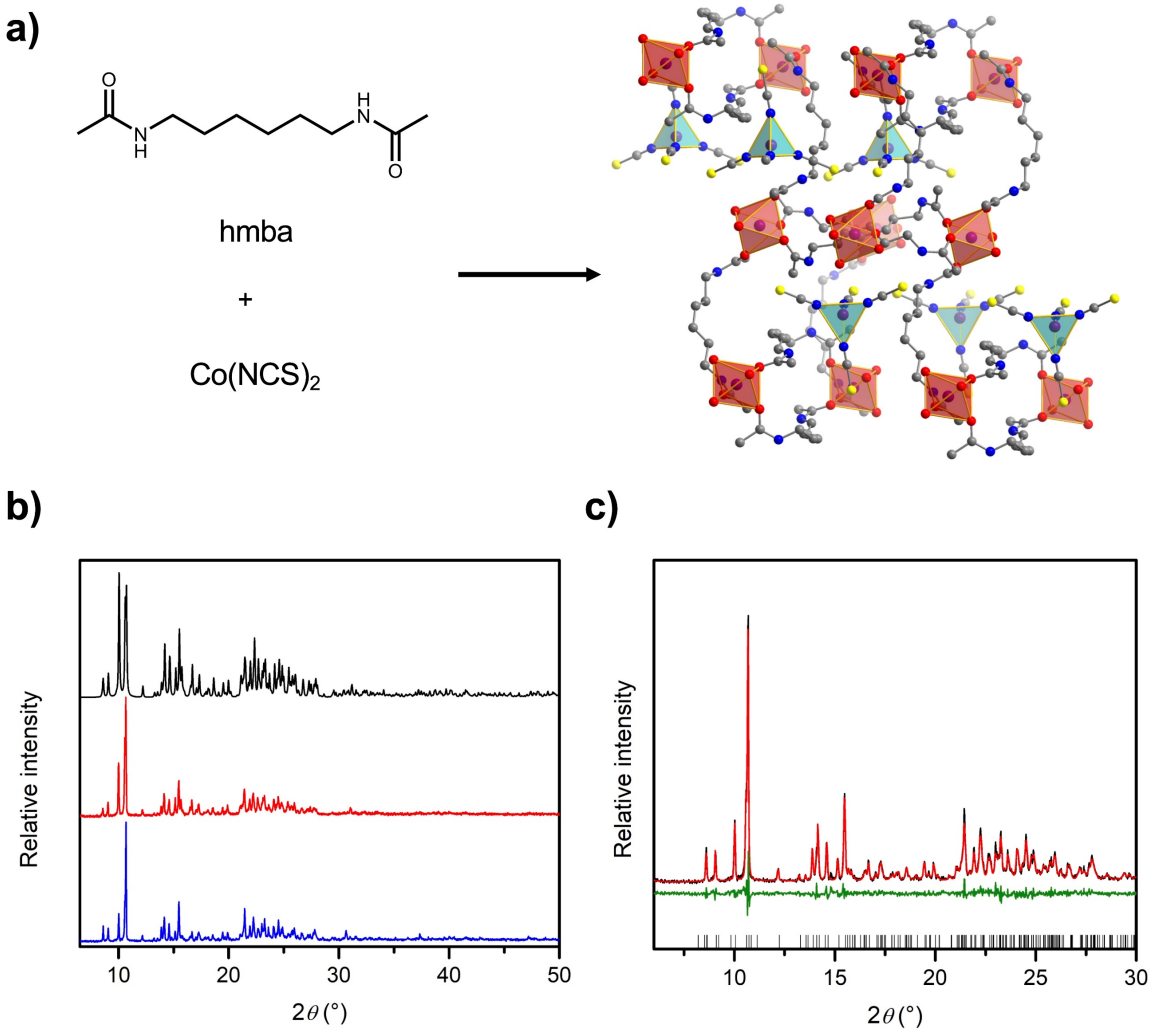

Figure S8. a) Previously reported crystal structure of $Co(hmba)_3[Co(NCS)_4]$.[2] Purple, red, gray, blue, yellow spheres represent Co, O, C, N, S atoms, respectively. H atoms have been omitted for clarity. b) Ambient temperature powder X-ray diffraction patterns of $Co(hmba)_3[Co(NCS)_4]$ before (red) and after (blue) 1 DSC cycle, along with diffraction pattern calculated from the single crystal structure of $Co(hmba)_3[Co(NCS)_4]$ (black). c) Le Bail refinement of recrystallized $Co(hmba)_3[Co(NCS)_4]$ after melt at ambient temperature. Black and red lines correspond to the observed and calculated diffraction patterns, respectively. The green line represents the difference between observed and calculated patterns, and the black tick marks indicate calculated Bragg peak positions based on the refined unit cell. Unit cell: triclinic, $P\bar{1}$, a = 11.5587(9) Å, b = 11.8280(11) Å, c = 20.4115(15) Å, α = 93.982(6)°, β = 103.674 (5)°, γ = 83.627(5) °, V = 2477.0 (4) Å^3, R_{wp} = 8.2 %, R_n = 6.3 %.

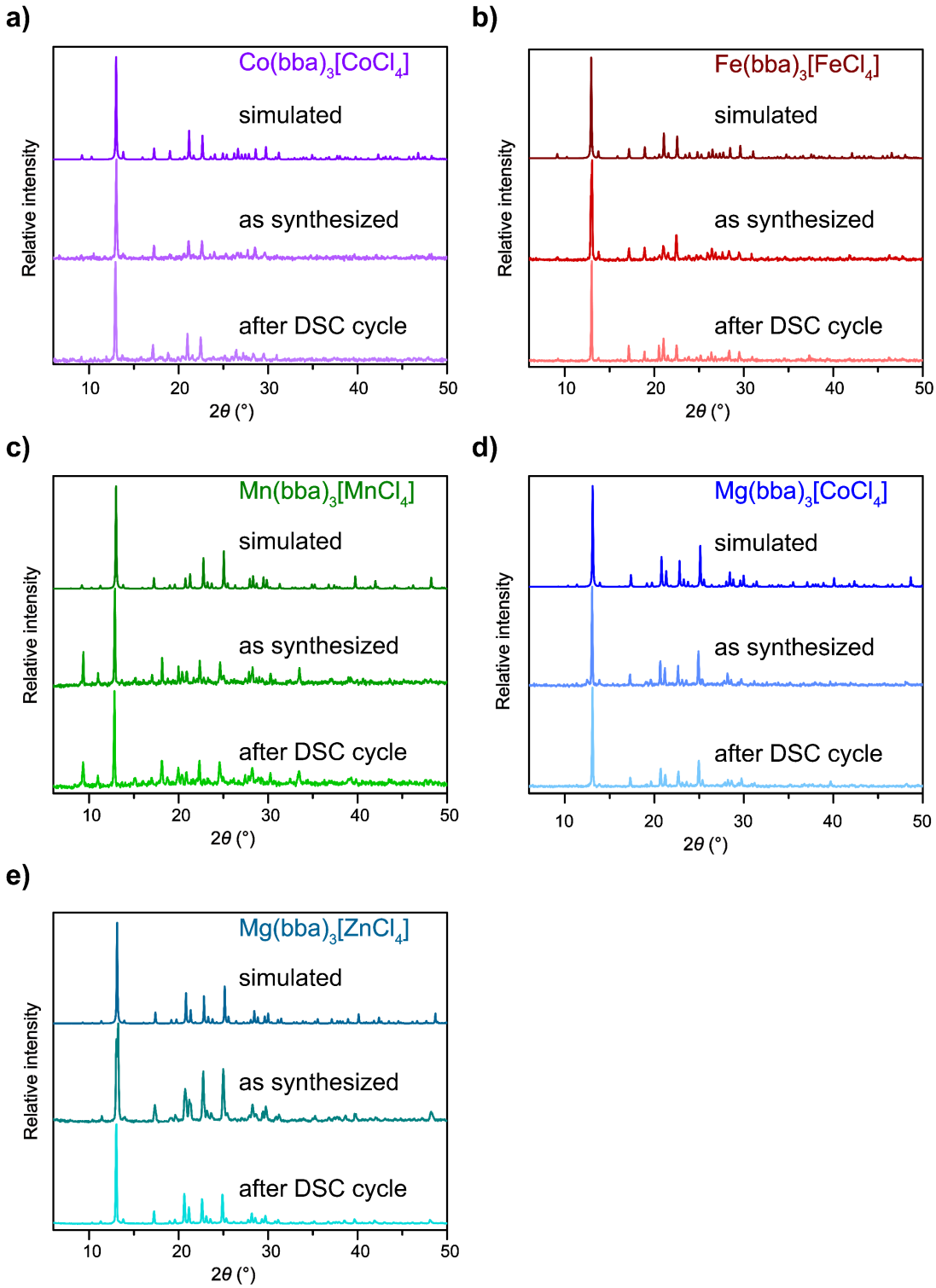

Figure S9. Powder X-ray diffraction patterns of a) $Co(bba)_3[CoCl_4]$, b) $Fe(bba)_3[FeCl_4]$ c) $Mn(bba)_3[MnCl_4]$, d) $Mg(bba)_3[CoCl_4]$, and e) $Mg(bba)_3[ZnCl_4]$ at ambient temperature. In each plot, the top line represents the calculated diffraction pattern from a 100 K crystal structure of each compound. The middle and bottom lines correspond to the diffraction pattern of the as-synthesized compound and of the compound after 1–3 DSC cycles, respectively.

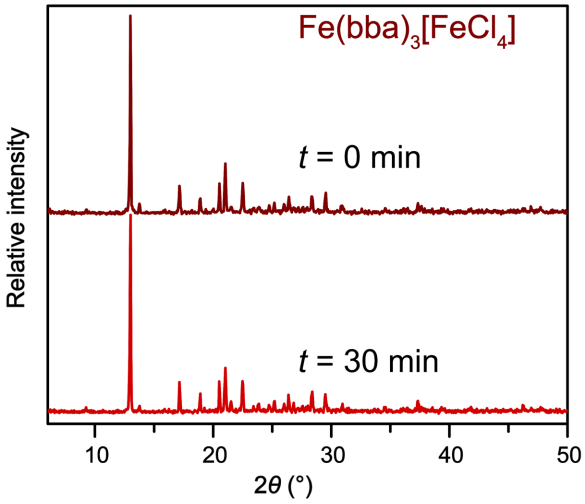

Figure S10. Powder X-ray diffraction patterns of $Fe(bba)_3[FeCl_4]$ at ambient temperature before (top, dark red) and after (bottom, light red) exposure to air for 30 min.

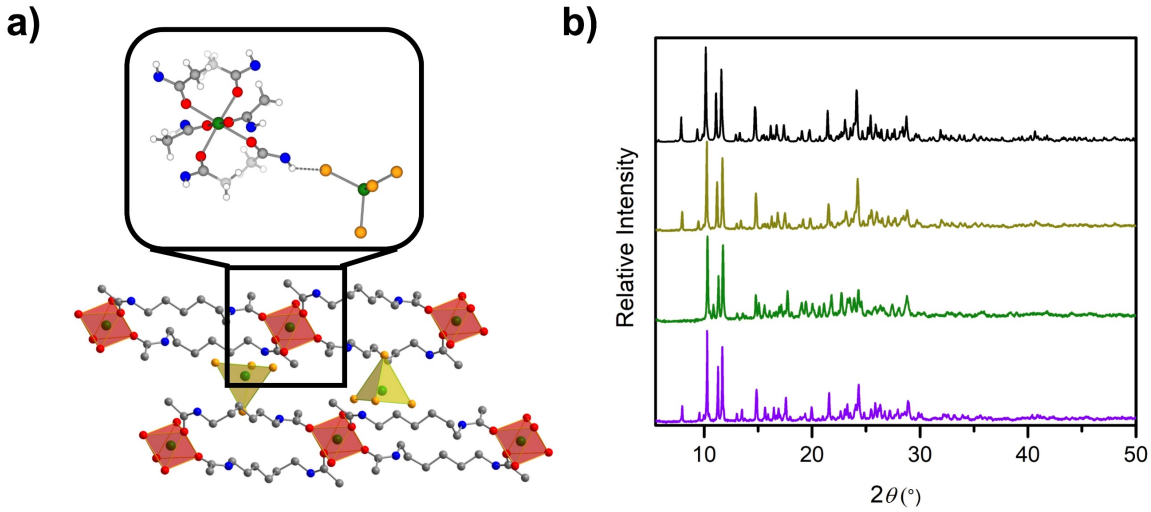

Figure S11. a) Previously reported crystal structure of $Mn(hmba)_3[MnBr_4]$.[3] Green, red, gray, blue, and yellow spheres represent Mn, O, C, N, and Br atoms, respectively. H atoms have been omitted for clarity. Inset: hydrogen bonding geometry between bba N–H proton and $[MnBr_4]^{2-}$ counteranion. White spheres represent H atoms. b) Powder X-ray diffraction patterns of $M(hmba)_3[MX_4]$ at ambient temperature. The black line represents the calculated diffraction pattern from the single crystal structure of $Mn(hmba)_3[MnBr_4]$. The dark yellow, green, and purple lines correspond to the experimentally synthesized $Mn(hmba)_3[MnBr_4]$, $Mn(hmba)_3[MnCl_4]$, and $Co(hmba)_3[CoBr_4]$, respectively.

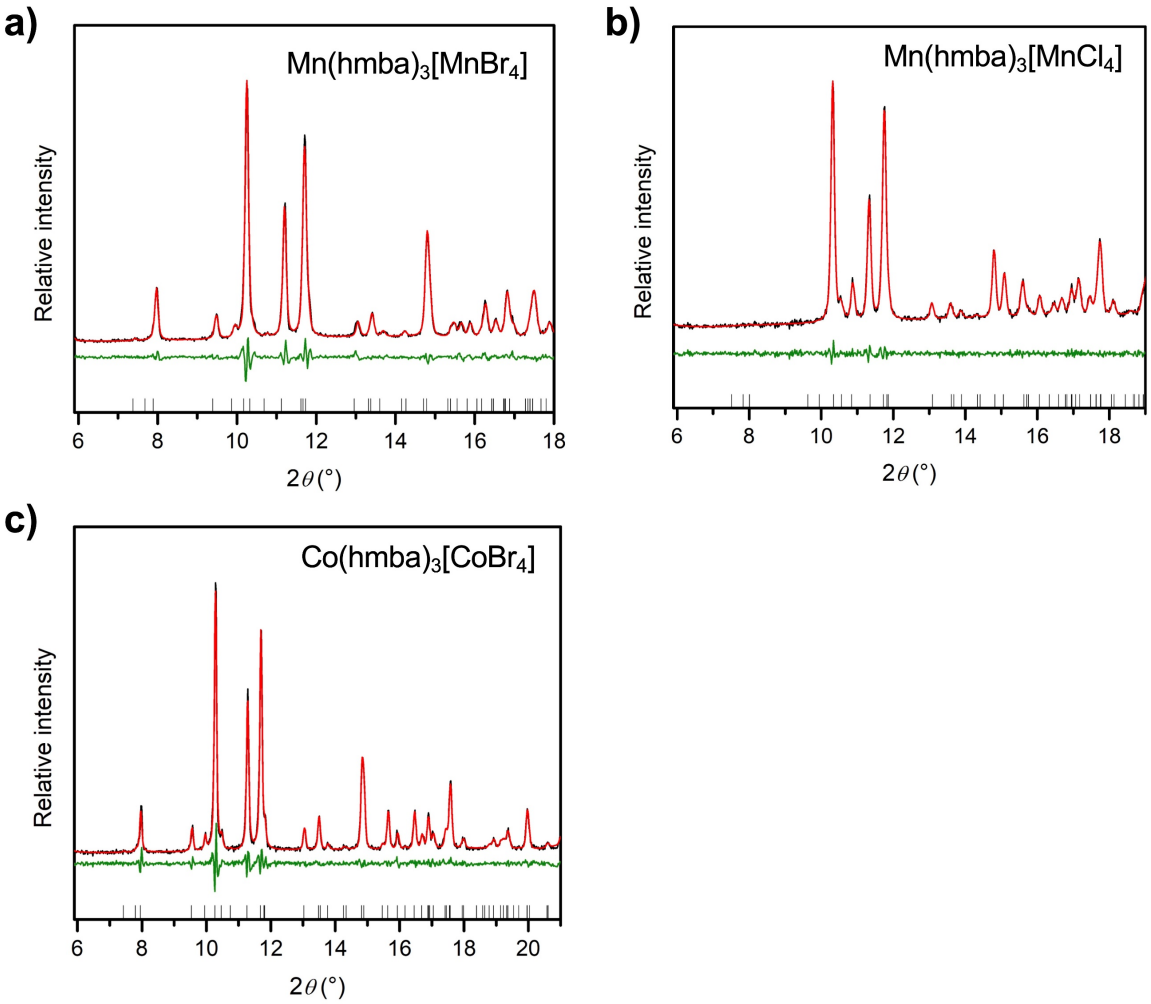

Figure S12. Le Bail refinement of $M(hmba)_3[MX_4]$ frameworks at ambient temperature. In each graph, black and red lines correspond to the observed and calculated diffraction patterns, respectively. The green line represents the difference between observed and calculated patterns, and the black tick marks indicate calculated Bragg peak positions based on the refined unit cell. a) $Mn(hmba)_3[MnBr_4]$, R_{wp} = 5.80 %, R_p = 4.46 %, b) $Mn(hmba)_3[MnCl_4]$, R_{wp} = 3.72 %, R_p = 2.87 %, c) $Co(hmba)_3(CoBr_4)$, R_{wp} = 8.70 %, R_p = 6.82 %. Unit cell parameters are listed in Table S11.

Table S11. Ambient temperature unit cell parameters of the $M(hmba)_3[MCl_4]$ series from Le Bail refinements.

Compound	*a* (Å)	*b* (Å)	*c* (Å)	*α* (°)	*β* (°)	*γ* (°)	*V* (Å^3)	Space Group
$Mn(hmba)_3[MnBr_4]$ literature[3]	11.597(3)	12.652(2)	16.040(2)	72.018(10)	85.26(2)	83.69(2)	2222	$P\bar{1}$
$Mn(hmba)_3[MnBr_4]$ experimental	11.532(2)	12.580(2)	15.961(1)	108.123(8)	94.796(10)	83.671(6)	2184.3(6)	$P\bar{1}$
$Mn(hmba)_3[MnCl_4]$	11.365(2)	12.424(2)	15.876(2)	107.913(9)	93.734(10)	83.768(6)	2136.0(6)	$P\bar{1}$
$Co(hmba)_3[CoBr_4]$	11.422(1)	12.563(2)	15.943(2)	107.831(8)	94.335(9)	83.672(5)	2162.3(5)	$P\bar{1}$

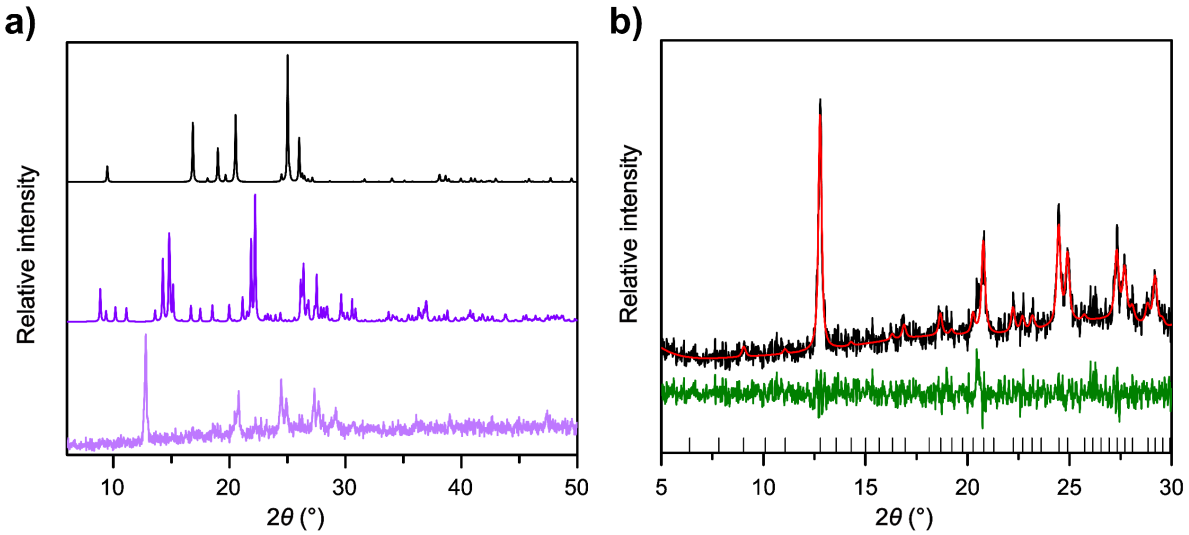

Figure S13. a) Ambient-temperature powder X-ray diffraction patterns of bba ligand (black), $Co(bba)_3Br_2$ (purple), and the new phase formed from $Co(bba)_3Br_2$ (T_m = 120 °C) after 1 DSC cycle and a 120-min isothermal hold at 60 °C (light purple). b) Le Bail refinement of $Co(bba)_3Br_2$ after the DSC cycle and isothermal hold. Black and red lines correspond to the observed and calculated diffraction patterns respectively. The green line represents the difference between observed and calculated patterns, and the black tick marks indicate calculated Bragg peak positions based on the refined unit cell. Unit cell: cubic, $Pa\bar{3}$, $a = b = c$ = 19.485(8) Å, $\alpha = \beta = \gamma$ = 90°, V = 7512(9) Å^3, R_{wp} = 12.90 %, R_p = 10.06 %. Unit cell parameters suggests partial formation of a $Co(bba)_3[CoBr_4]$ phase, which likely adapts the same network structure as $Co(bba)_3[CoCl_4]$, from the melt. In this scenario, 50% of the Co centers from the original phase would bind to bba ligands while the other 50% would form $CoBr_4$, which is consistent with EXAFS analyses (Table S19).

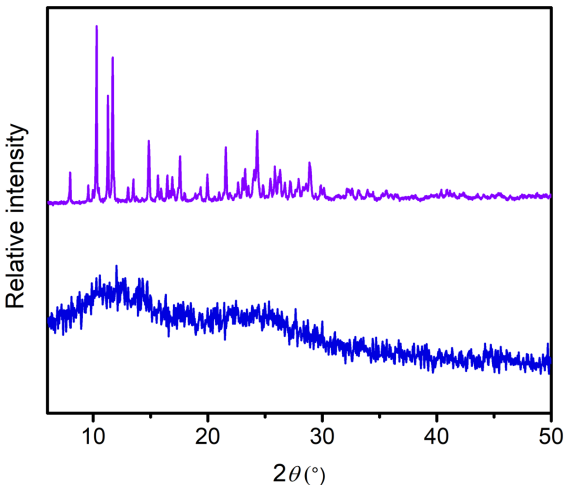

Figure S14. Powder X-ray diffraction patterns of as-synthesized $Co(hmba)_3[CoBr_4]$ (purple) and after cooling the melt to form a glass (blue).

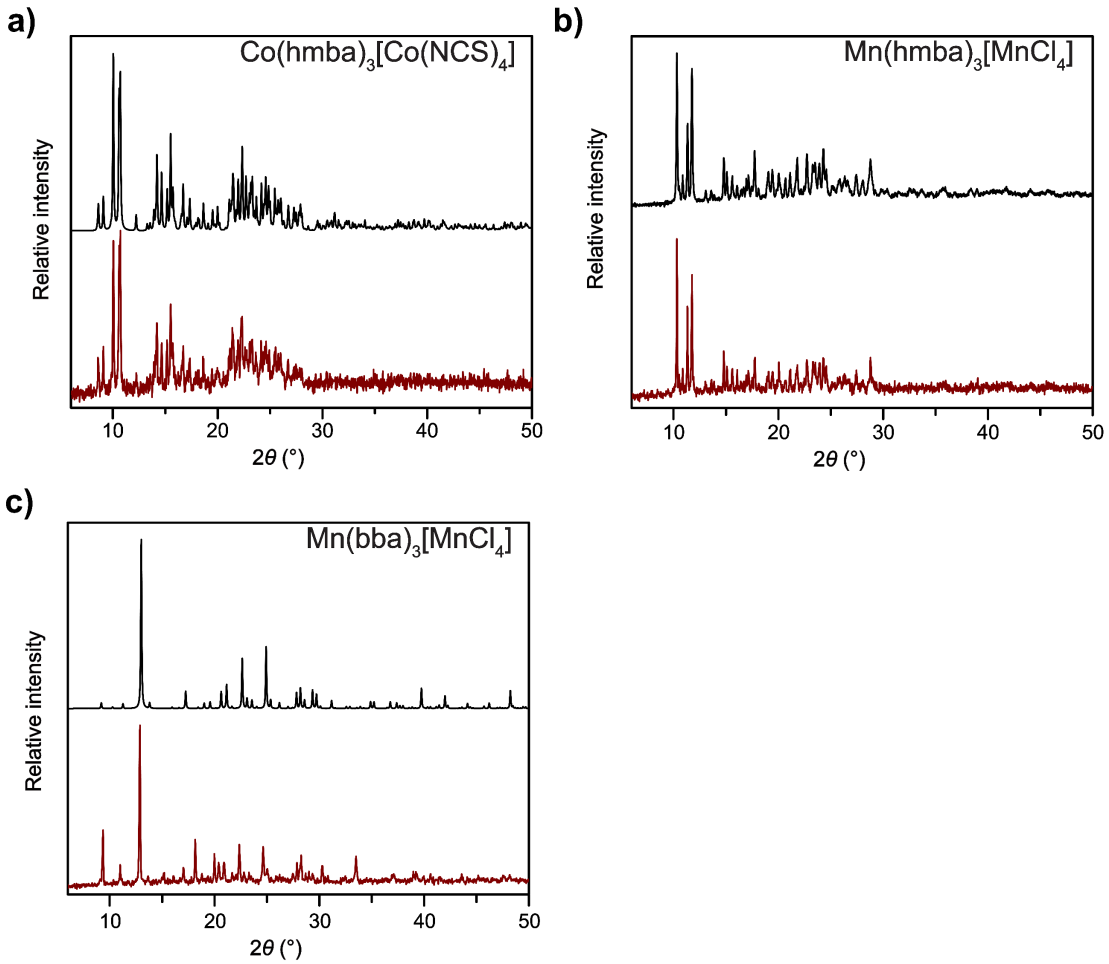

Figure S15. Powder X-ray diffraction pattern of a) $Co(hmba)_3[Co(NCS)_4]$, b) $Mn(hmba)_3[MnCl_4]$, and c) $Mn(bba)_3[MnCl_4]$ synthesized by mechanochemistry (dark red) at ambient temperature. The top black line represents the calculated diffraction pattern from a crystal structure in a) and c) and the experimental powder x-ray diffraction pattern of the solution-phase product in b).

Table S12. Summary of previously reported melting transitions in metal–organic frameworks and coordination polymers.

MOF/CP	Chemical formula[a]	Dimensionality[b]	T_m (°C)[c]	Reversibility	Ref.
ZIF-4	$Zn(Im)_2$[d]	3-D	593	irreversible[j]	18, 19
GIS	$Zn(Im)_2$[e]	3-D	584	irreversible[j]	19
ZIF-76-mbIm	$[Zn(Im)_{1.33}(5\text{-mbIm})_{0.67}]$	3-D	471	irreversible	20
TIF-4	$Zn(Im)_{1.5}(5\text{-mbIm})_{0.5}$[e]	3-D	467	irreversible	19
ZIF-76	$[Zn(Im)_{1.62}(5\text{-ClbIm})_{0.38}]$	3-D	451	irreversible	20
ZIF-62	$Zn(Im)_{2-x}(bIm)_x$[f]	3-D	350–437	irreversible	19, 21, 22
ZIF-UC	$Zn(Im)_{2-x}(xbIm)_x$[g] xbIm = 6-Cl-5-Fbim, 5-Cl-2-mbIm, 5-FbIm, 5-ClbIm	3D	390–432	irreversible	23
	$[Ag(pL2)(CF_3SO_3)]\cdot 2C_6H_6$	3-D	271	irreversible[j]	24
	$[Co(cp)_2][K\{B(CN)_4\}_2]$, $[Co(cp)_2][Na\{N(CN)_2\}_2]$	3-D	167, 373[h]	irreversible	25
	$[Ru(cp)(C_6H_5R)][M\{C(CN)_3\}_2]$	3-D	149	irreversible[k]	25
	$[Cu_8(SNC)_{12}(Phbpy)_4]$	2-D	217	N/A	26
	$[M'(cp)(C_6H_6 \text{ or } cp)][M\{C(CN)_3\}_2]$ (M′ = Rb, Co, M = K)	2-D	205–244	irreversible[j,k]	25
	$Zn(H_2PO_4)_2(HTr)_2$	2-D	184	reversible	27
	$[Ag(mL1)(CF_3SO_3)]\cdot 2C_6H_6$	2-D	169	irreversible	28
	$[\{Zn_2(HPO_4)_2(H_2PO_4)\}(ClbimH^+)_2\cdot(H_2PO_4^-)\cdot(MeOH)]_n$	2-D	148	irreversible	29
	$[Cu_2(SNC)_3(C_nbpy)]$ (n = 2, 4)	2-D	138, 187	N/A	26
	$[Cu(SNC)_2(3\text{-pybpy})]$	1-D	203	N/A	26
	$\{[Co(\mu\text{-NCS})_2(pza)_2]\cdot pza\}_n$ $[Co(\mu\text{-NCS})_2(pza)_2]_n$	1-D	180–220	irreversible	30, 31
	$[Zn_3(H_2PO_4)_6(H_2O)_3]\cdot HbIm$	1-D	164	reversible	27
	$[Zn(HPO_4)(H_2PO_4)_2]\cdot 2H_2Im$	1-D	154	reversible	27
	[Cu(ipym)]	1-D	146 or 185[i]	reversible	32
	$[Zn_3(H_2PO_4)_6(H_2O)_3]\cdot H(2\text{-mbIm})$	1-D	97	reversible	27
	$(C_4C_1py)[Cu(SCN)_2]$	1-D	87	reversible	33

[a]Im = imidazolate; 5-mbIm = 5-methylbenzimidazolate; 5-ClbIm = 5-chlorobenzimidazolate; bIm = benzimidazolate; 6-Cl-5-FbIm = 6-chloro-5-fluorobenzimidazolate; 5-Cl-2-mbIm = 5-chloro-2-methylbenzimidazolate; 5-FbIm = 5-fluorobenzimidazolate; *p*L2 = 1,3,5-tris(4-ethynylbenzonitrile)benzene); cp = cyclopentadiene; *m*L1 = 1,3,5-tris(3-cyanophenylethynyl)benzene; Tr = 1,2,4-triazolate; C_2bpySCN = 1-ethyl-[4,4′-bipyridin]-1-ium thiocyanate; C_2bpySCN = 1-butyl-[4,4′-bipyridin]-1-ium thiocyanate; PhbpySCN = 1-phenyl-[4,4′-bipyridin]-1-ium thiocyanate; 3-pybpySCN = [3,1′:4′,4″-terpyridin]-1′-ium thiocyanate; pza = pyrazinamide, ipym = 2-isoproylimidzaolate; 2-mbIm: 2-methylbenzimidazolate; C_4C_1py = 1-butyl-4-methyl-pyridinium. [b]Here, dimensionality refers to the dimensionality

of the metal–organic coordination network within each compound. [c]Only compounds that melt into a pure liquid state are tabulated here, while compounds that phase separate into a mixture of liquid and solid phases are excluded. For example, $[Ru(cp)(C_6H_5R)][M\{C(CN)_3\}_2]$ (R = Et, Me, M = Rb, K) have been reported to melt incongruently into an ionic liquid $[Ru(cp)(C_6H_5R)][C(CN_3)]$ and a metal salt $M[C(CN)_3]$ over temperature range of 103–215 °C.[25] [d]Before reported melting, a crystalline to amorphous to crystalline transition occurs for the denoted material. [e]Before reported melting, a crystalline to amorphous transition occurs for the denoted material. [f]For frameworks with $x \leq 0.05$, a crystalline to amorphous to crystalline transition occurs prior to melting. [g]Isostructural to ZIF-62, $0.13 \leq x \leq 0.34$. [h]Determined by visual observation. [i]The two isomers of [Cu(ipym)] have different T_m, with the parallel-packing isomer melt at 146 °C and the stranded-helix isomer melting at 185 °C. However, the later converts to the former upon melting and crystallization, and only the melting transition at 146 °C is reversible. [j]Thermal decomposition occurs soon after melting transition, and likely contributes to the irreversibility. [k]Gradual decomposition observed in liquid state, and likely contributes to the irreversibility.

Table S13. Summary of previously reported crystal structures of first-row transition metal networks containing polymethylene bis(acetamide) bridging ligands.

CSD code	Ligand[a]	Metal	Formula	Dimensionality	T_m (°C)	Ref.
QAYTAL	hmba	Co	$Co(hmba)_3[Co(NCS)_4]$	3-D	145–147	2
FEVTEF	hmba	Co	$Co(hmba)_3(CoCl_4)\cdot 2EtOH$	3-D	N/A	3
QAYTIT	hmba	Co	$Co(hmba)_3(HgCl_4)$	3-D	120-122	2
FEVVIM	hmba	Mn	$Mn(hmba)_3(MnBr_4)\cdot 2EtOH$	3-D	N/A	3
FEVWEI	hmba	Mn	$Mn(hmba)_3(MnBr_4)$	2-D	N/A	3
QAYTOZ	hmba	Mn	$Mn(hmba)_3(HgBr_4)\cdot 3CHCl_3$	2-D	158–160	2
QAYTEP	hmba	Nd	$Nd(hmba)_3[Nd(NO_3)_6]\cdot 2CHCl_3$	3-D	232–234	2
FEVYEK	bba[b]	Co	$Co(bba)_3Br_2$	2-D	N/A	3
FEVYIO	eba	Co	$Co(eba)_2(H_2O)_2Br_2$	2-D	N/A	3
OYPZEI	eba[c]	Zn	$Zn(eba)_{1.5}(NO_3)\cdot NO_3$	2-D	N/A	34

[a]hmba = *N*,*N*′-1,6-hexamethylenebis(acetamide), bba = *N*,*N*′-1,4-butaylenebis(acetamide), eba = *N*,*N*′-1,2-ethylenebis(acetamide).

Thermal Characterization

Differential Scanning Calorimetry (DSC)

A Discovery 2500 DSC with an RCS 90 cooling system (TA Instruments) was used to measure the melting temperatures and gravimetric enthalpies for all compounds. The DSC baseline and cell thermal parameters were calibrated using sapphire discs. The temperature and cell constant were calibrated using an indium standard. All DSC samples were prepared under a nitrogen atmosphere using 3–15 mg of sample and were hermetically sealed in aluminum pans (purchased from TA Instruments). Heating and cooling rates of 5 °C/min were used with a 50 mL/min N_2. An empty, aluminum pan hermetically sealed under N_2 was used as a reference.

Determination of T_m and gravimetric ΔH_{fus} (J/g)

Melting temperatures, T_m, and enthalpies of fusion, ΔH_{fus}, were determined using the TA Instrument TRIOS software. Peaks were selected for analysis by defining a temperature range containing the peak of interest. The lower bound and upper bounds of the temperature range were chosen to encompass the phase transition, which starts with a deviation from the baseline and ends with a return to baseline.

Prior to determination of T_m or ΔH_{fus}, a baseline, which models the heat flow in the absence of melting, must be generated to approximate the baseline in the transition region in the absence of a transition.[35,36] TRIOS generates a baseline within the defined temperature range using various options that determine the slope of the lower and higher temperature limits and shape of the baseline. When possible, baselines were generated using mutual tangent slopes at both the upper and lower temperature limits with a sigmoidal baseline, which we found to produce most physically reasonable baselines.[36] Mutual tangents, however, are best determined when the tangent can be made to a well-defined baseline. Since compounds in this study have non-zero vapor pressure upon melting, most samples were heated no more than 15 °C above their melting temperature to avoid pressurizing the cell, giving limited baseline information above the melting endotherm from which to find a mutual tangent. In such cases a mutual tangent was used for the lower temperature limit while a less physical horizontal baseline, which uses the heat flow value at the temperature limit and extrapolates a horizontal baseline, was used for the upper temperature limit.

The extrapolated onset temperature was reported as the melting temperature, as is standard in DSC data analysis, because the onset temperature—unlike the peak temperature—is relatively independent of experimental parameters like the heating rate or sample mass.[35] The onset temperature is determined by identifying the region of the onset melting peak that has the highest slope, defining a tangent to that region, and then extending the tangent to the generated baseline. The intersection between the baseline and the tangent is the onset temperature, and TRIOS reports this value during peak integration. Endotherms were integrated between the upper and lower temperature limits with the baseline subtracted to provide ΔH_{fus} (J/g). If physically reasonable limits were chosen, the onset melting temperatures and ΔH_{fus} did not depend strongly on the choice of the temperature limits, and such variations were within the error of the measurements, which is estimated to be < 0.5% for T_m and < 2% for ΔH_{fus}.[37] Compounds that show an average enthalpy decrease of 5% or less upon each melting and recrystallization cycle are classified as reversible, while compounds that show a greater decrease upon cycling are considered irreversible.[37] Note that 1) given differences in reversibility and recrystallization kinetics, thermodynamics parameters

of the first melting transition are used for comparative analyses; 2) volumetric ΔH_{fus} were calculated from gravimetric quantities using crystallographic densities at ambient temperature.

Table S14. Summary of melting thermodynamics of all compounds reported in this work.

Compound	Dimensionality	T_m (°C)	ΔH_{fus} (J/g)	ΔH_{fus} (kJ/L)	ΔH_{fus} (kJ/mol)	ΔS_{fus} (J/L/K)	ΔS_{fus} (J/mol·K)
$Co(hmba)_3[Co(NCS)_4]$	3-D	144	114	146	108	350	260
$Co(hmba)_3[CoBr_4]$	2-D	106	93	148	97	390	255
$Mn(hmba)_3[MnCl_4]$	2-D	139	116	157	99	380	239
$Mn(hmba)_3[MnBr_4]$	2-D	139	96	148	99	359	240
$Co(bba)_3[CoCl_4]$	3-D	124	101	142	78	359	198
$Fe(bba)_3[FeCl_4]$	3-D	147	105	146	81	348	193
$Mn(bba)_3[MnCl_4]$	3-D	172	103	143	79	322	177
$Mn(bba)_3[ZnCl_4]$	3-D	185	107	151	83	329	182
$Mg(bba)_3[CoCl_4]$	3-D	260	119	163	88	306	166
$Mg(bba)_3[ZnCl_4]$	3-D	262	131	182	98	340	183
$Co(bba)_3Br_2$	2-D	120	172	258	137	658	348
$Mg(bba)_3Cl_2$	2-D	220	231	289	141	586	287

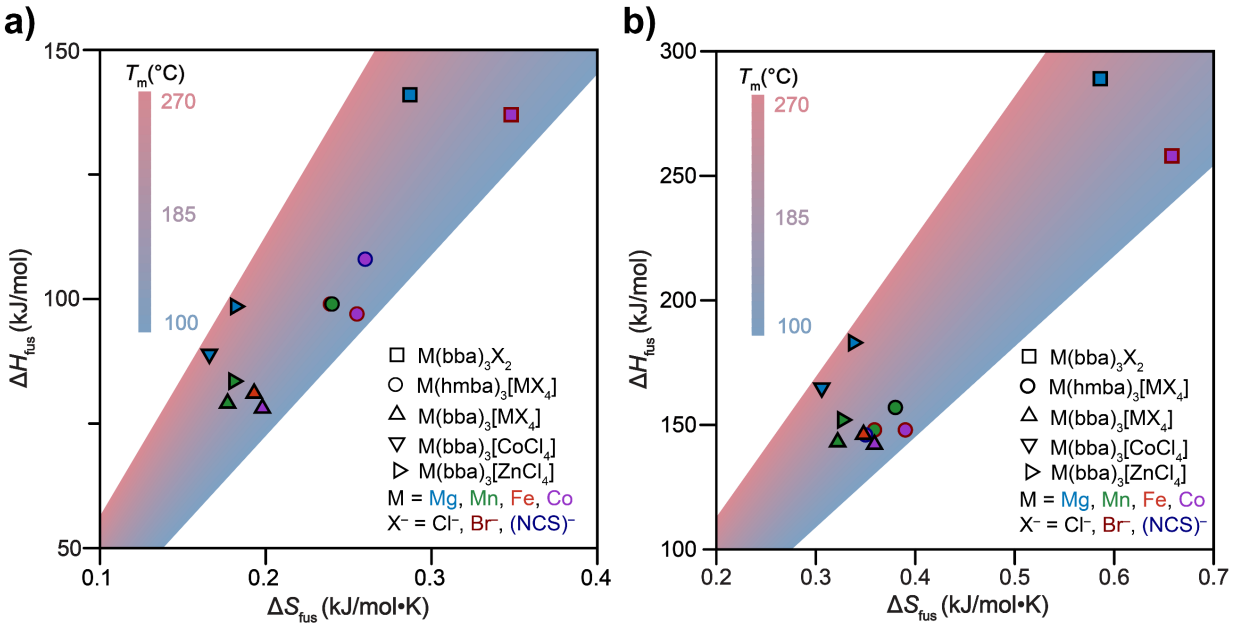

Figure S16. Summary of the enthalpy of fusion, ΔH_{fus}, and entropy of fusion, ΔS_{fus}, for all metal–organic networks reported here on a a) molar basis; b) volumetric basis. The melting temperature, T_m, is indicated by the background color, increasing from blue (100 °C) to red (270 °C). The symbol shape indicates the series of compounds, the symbol color indicates the metal, and border color indicates the counteranion. Note that the volumetric values are calculated from gravimetric values using crystallographic densities.

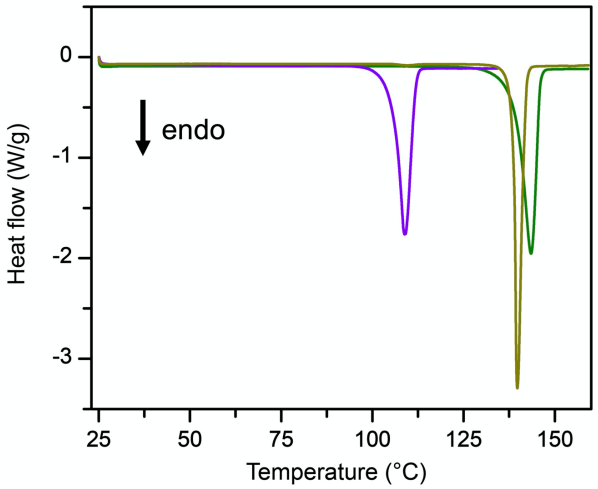

Figure S17. Differential scanning calorimetry traces of the first heating run for $Co(hmba)_3[CoBr_4]$ (purple), $Mn(hmba)_3[MnBr_4]$ (brown), and $Mn(hmba)_3[MnCl_4]$ (green).

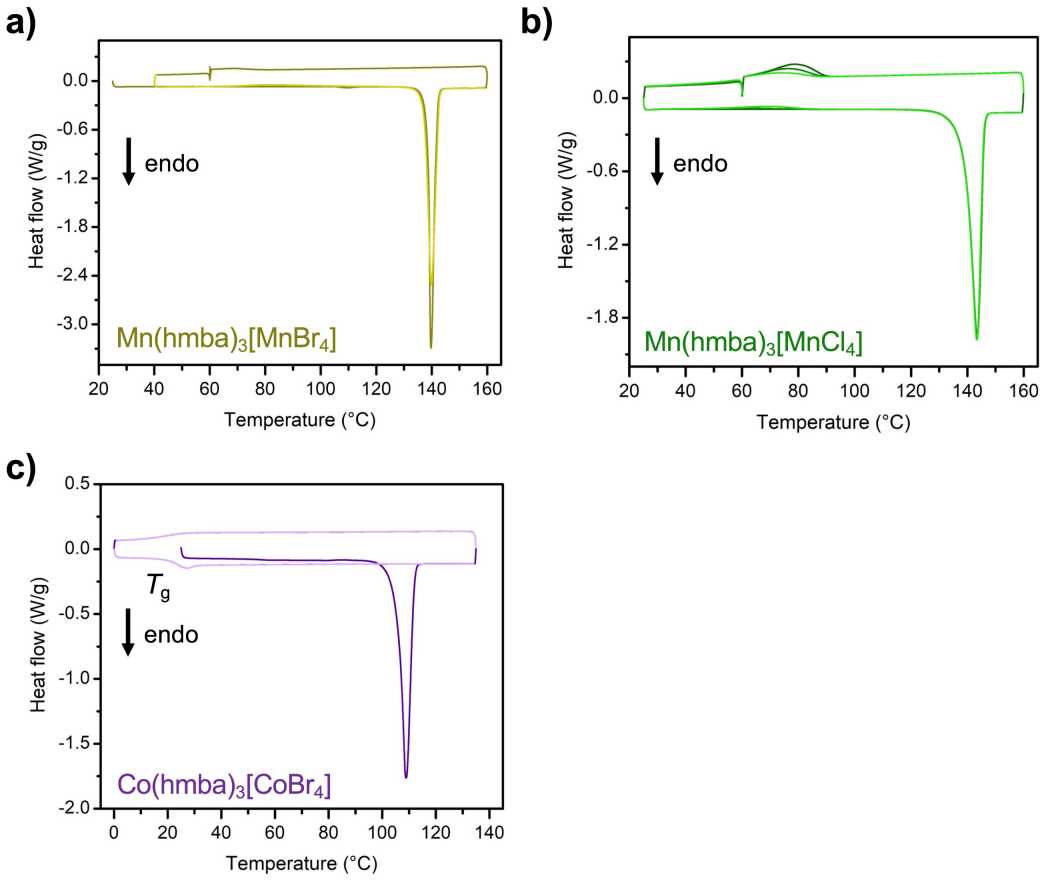

Figure S18. Differential scanning calorimetry traces for a) $Mn(hmba)_3[MnBr_4]$, b) $Mn(hmba)_3[MnCl_4]$, and c) $Co(hmba)_3[CoBr_4]$. Successive heating–cooling cycles are shown progressing from dark (first cycle) to light (final cycle) colors.

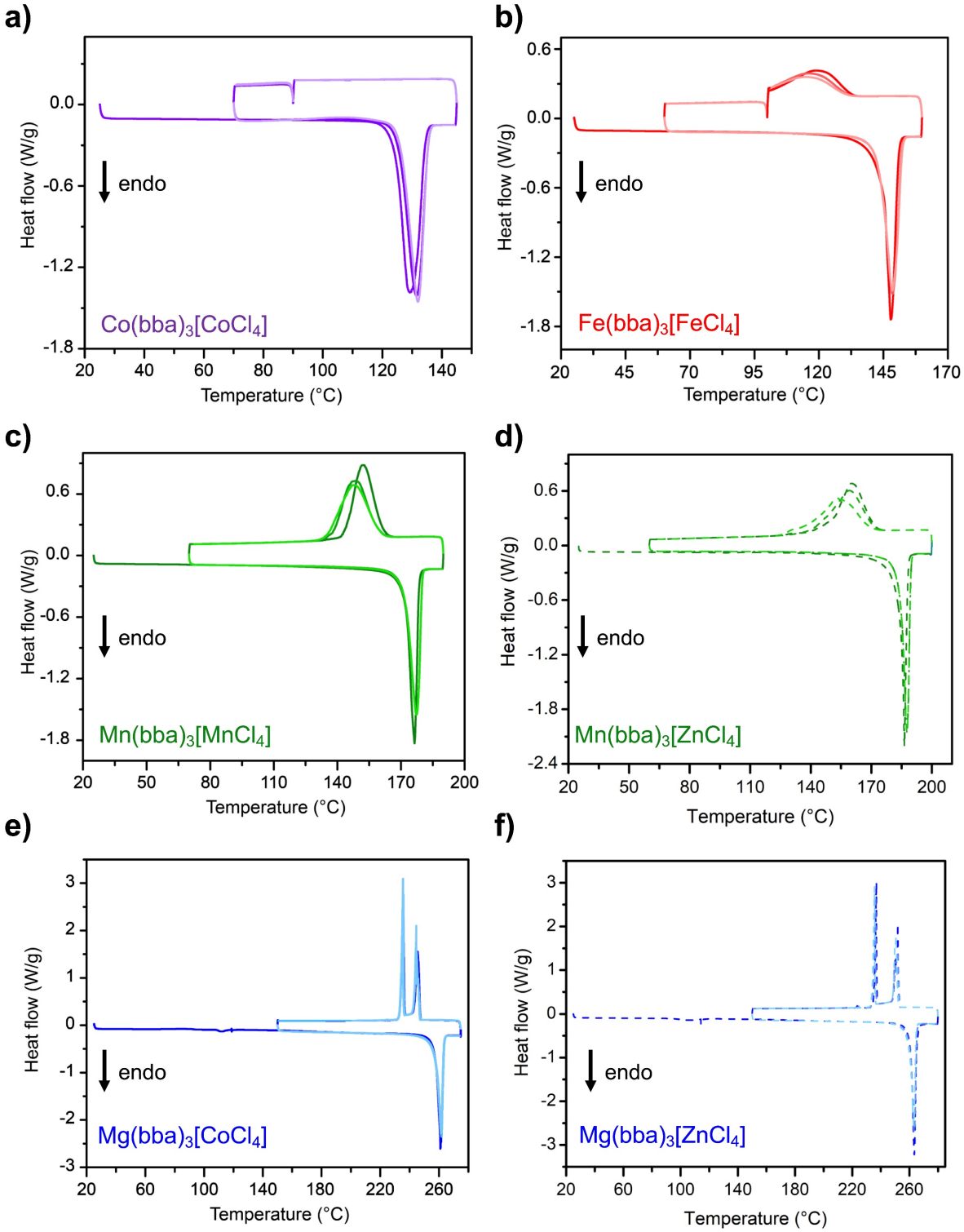

Figure S19. Differential scanning calorimetry traces of $M(bba)_3[M'X_4]$. Successive heating–cooling cycles are shown progressing from dark (first cycle) to light (final cycle) colors. Note that in a) an isothermal hold at 90 °C for 150 min leads to full crystallization; in b) an isothermal hold at 100 °C for 30 min leads to full recrystallization; and in e) and f), the two exothermic peaks on the cooling runs of $Mg(bba)_3[CoCl_4]$ and $Mg(bba)_3[ZnCl_4]$ most likely correspond to crystallization of two portions of the samples that are physically separated, instead of crystallization into two different phases (see Figure S20).

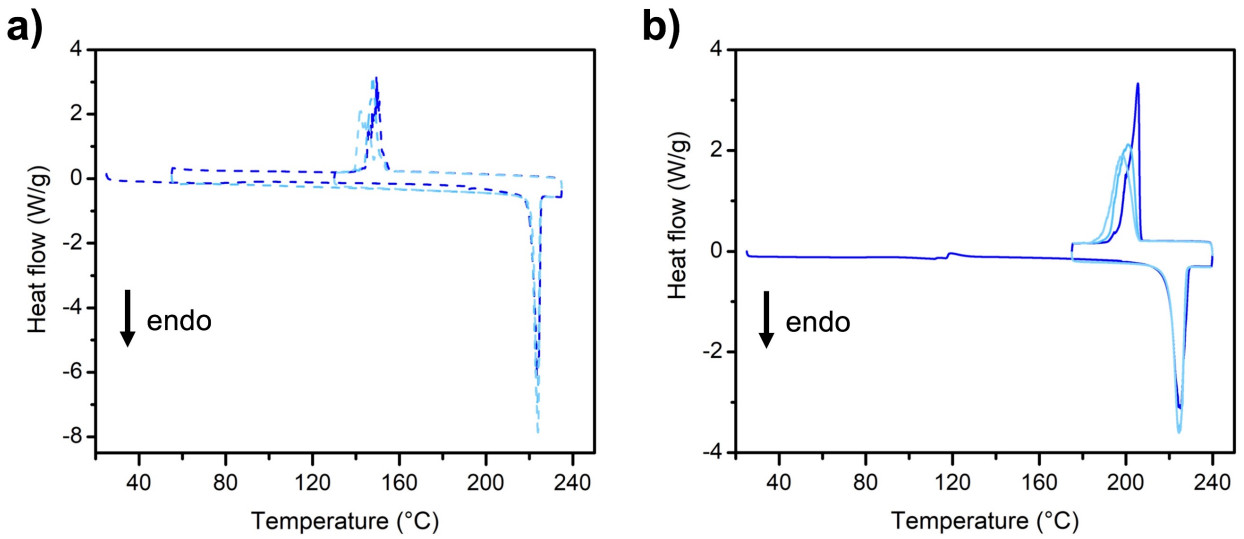

Figure S20. Differential scanning calorimetry traces for a) $Mg(bba)_3[CoCl_4]$ with an isothermal hold at 230 °C for 30 min during cooling and b) $Mg(bba)_3[ZnCl_4]$ with a 2 °C/min cooling rate (in contrast to a 5 °C/min cooling rate for in Figure S19 f). Successive heating–cooling cycles are shown progressing from dark (first cycle) to light (last cycle) colors. In both cases a single exotherm was observed, suggesting that the features in Figure S19e, f are due to portions of the sample that are in different locations of the DSC pan and recrystallize at slightly different times during cooling.

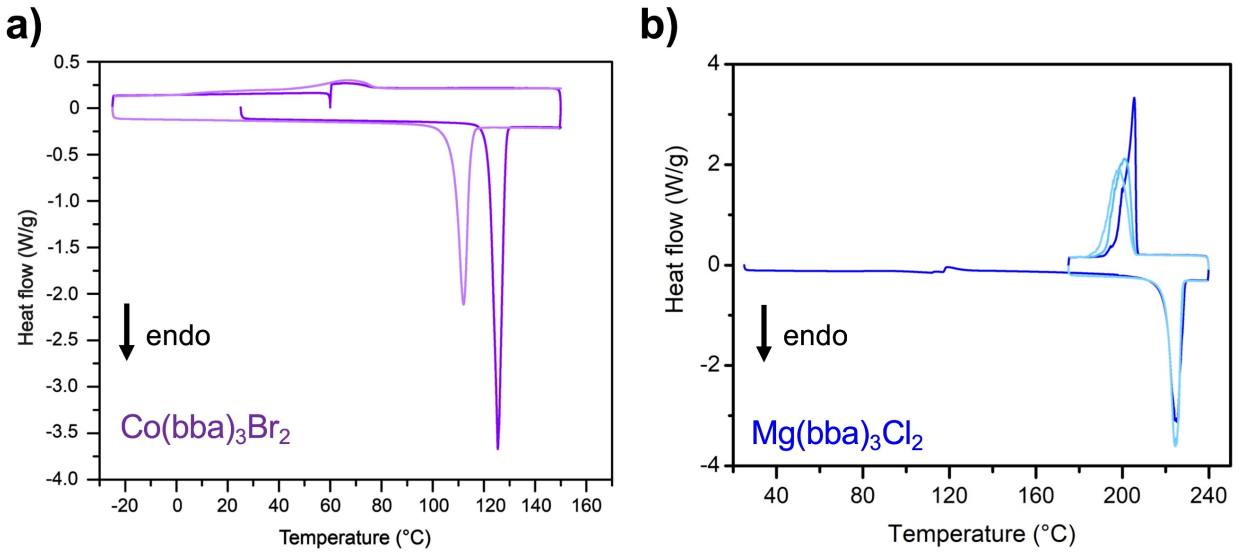

Figure S21. Differential scanning calorimetry traces of a) $Co(bba)_3Br_2$ and b) $Mg(bba)_3Cl_2$. Successive heating–cooling cycles are shown progressing from dark (first cycle) to light (final cycle) colors. While the melting transition of $Mg(bba)_3Cl_2$ is fully reversible, a new phase forms from the melt of $Co(bba)_3Br_2$ as confirmed by PXRD (Figure S13). Note that in a) an isothermal hold at 60 °C for 120 min leads to crystallization of the new phase, and in b), the minor exothermic peak on the first heat likely correspond to a small amount of cold crystallization of the mechanochemically synthesized powder.

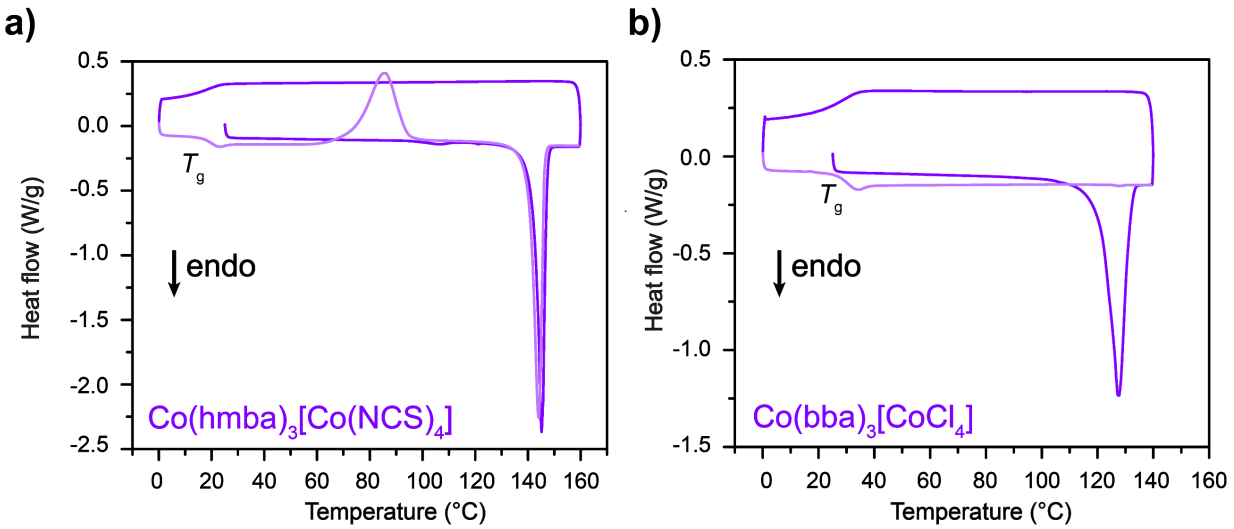

Figure S22. Differential scanning calorimetry traces showing glass transitions for a) $Co(hmba)_3[Co(NCS)_4]$ and b) $Co(bba)_3[CoCl_4]$. The cooling rate for these measurements was 10 °C/min. Successive heating–cooling cycles are shown progressing from dark (first cycle) to light (second cycle) purple. Note that in a) $Co(hmba)_3[Co(NCS)_4]$ undergoes a cold crystallization after the glass transition.

Table S15. Summary of glass transition temperatures, T_g, determined by DSC with cooling rates of 5–20 °C/min. T_g/T_m ratios of all metal–bis(acetamide) liquids are higher than the commonly observed 2/3 value, indicative of their high glass-forming ability.[38]

Compound	T_m (°C)	T_g (°C)	T_g/T_m[a]
$Co(hmba)_3[Co(NCS)_4]$	143	19	0.70
$Co(hmba)_3[CoBr_4]$	106	23	0.78
$Mn(hmba)_3[MnCl_4]$	139	32	0.74
$Mn(hmba)_3[MnBr_4]$	139	28	0.73
$Co(bba)_3[CoCl_4]$	124	30	0.76
$Fe(bba)_3[FeCl_4]$	147	28	0.72

[a]Note: Unit for both T_g and T_m is in kelvin (K).

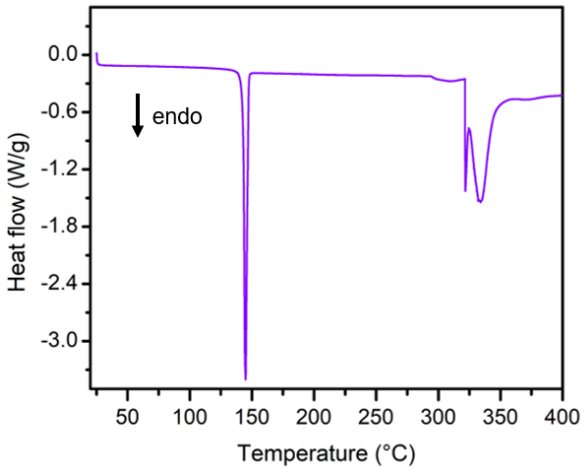

Figure S23. Differential scanning calorimetry trace to evaluate the thermal stability of $Co(hmba)_3[Co(NCS)_4]$. No feature relating to decomposition were observed until above 300 °C.

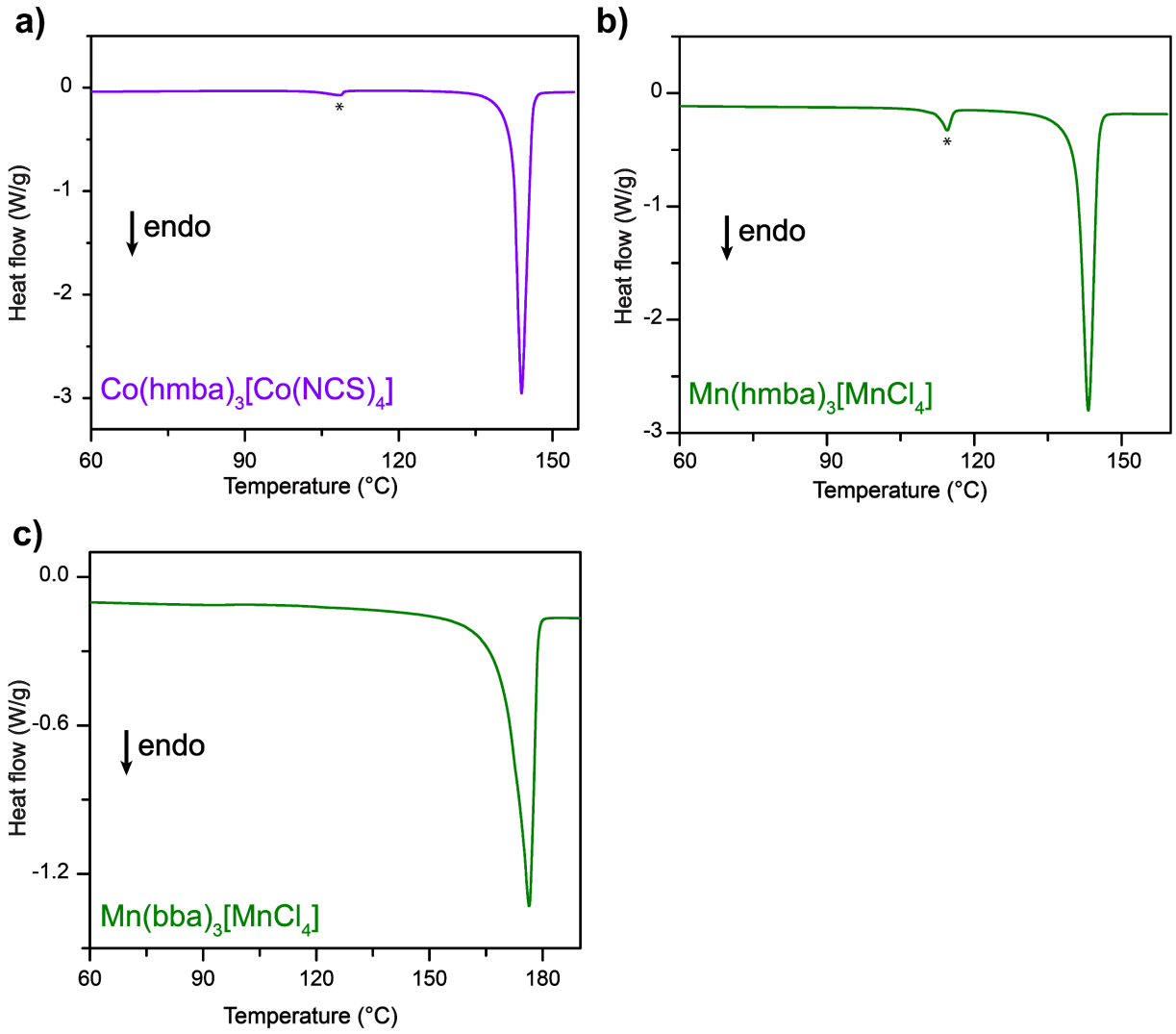

Figure S24. Differential scanning calorimetry traces for mechanochemically synthesized a) $Co(hmba)_3[Co(NCS)_4]$, b) $Mn(hmba)_3[MnCl_4]$, and c) $Mn(bba)_3[MnCl_4]$. For a typical batch, T_m and ΔH_{fus} could be 1–2 °C and 2– 8 % lower, respectively, relative to compounds synthesized solvothermally (Table S14). This could be a result of slightly lower crystallinity of the mechanochemically synthesized powder or a small amount of unreacted ligand impurity (minor peaks marked with * in a and b).

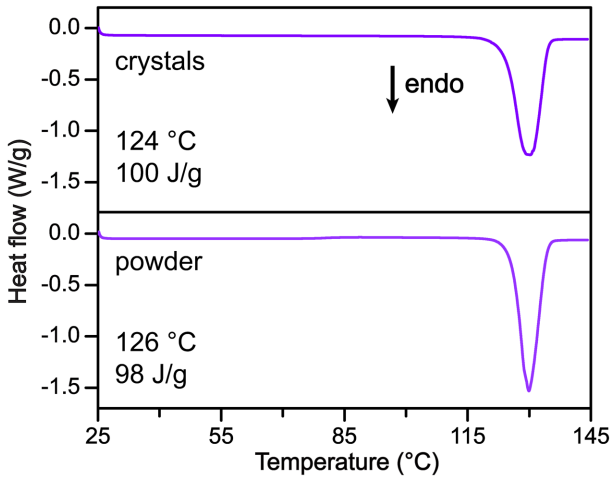

Figure S25. Differential scanning calorimetry traces for $Co(bba)_3[CoCl_4]$ in the form of large crystals (top) and a finely ground powder (bottom). The difference in ΔH_{fus} and peak temperature of the melting endotherms is minimal and within instrumental error. There is, however, a small dependence to the peak shape on particle size, with the endotherm for the powder sample having a narrower full width at half max (FWHM = 6.6 °C for crystals, 5.0 °C for powder), as well as a steeper melting onset leading to a 2 °C higher onset temperature. This is likely due to smaller particle sizes promoting better thermal contact with the DSC pan for a larger fraction of the sample.

Table S16. Summary of FWHM (°C) of the first and second melting endotherms for each compound reported in Figure 3c.

Full width half max of melting endotherm (°C)	$Co(bba)_3[CoCl_4]$	$Fe(bba)_3[FeCl_4]$	$Mn(bba)_3[MnCl_4]$	$Mg(bba)_3[CoCl_4]$
1^{st} melt	6.6	2.7	3.6	3.0
2^{nd} melt	6.1	4.4	5.0	3.2

Thermogravimetric Analysis (TGA)

Samples were loaded into a TGA 550 from TA Instruments in open aluminum pans with a stainless-steel bail under air and heated at a rate of 2–5 °C/min under a 10 mL/min N_2 flow from ambient to 500 °C with an empty aluminum pan/stainless steel bail used as the reference. The TGA mass was calibrated using a series of 3 reference masses, while the TGA temperature was calibrated to the Curie temperature of nickel.

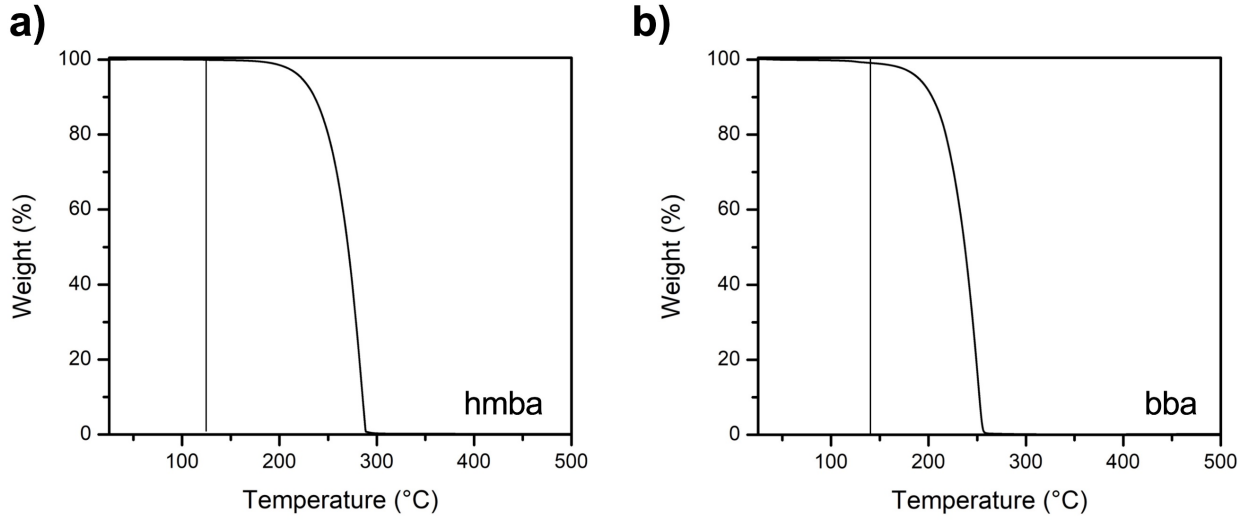

Figure S26. Thermogravimetric analysis of a) *N*,*N*′-1,6-hexamethylenebis(acetamide) (hmba) and (b) *N*,*N*′-1,4-butylenebis(acetamide) (bba) at a heating rate of 5 °C/min. The vertical line indicates T_m as determined by DSC.

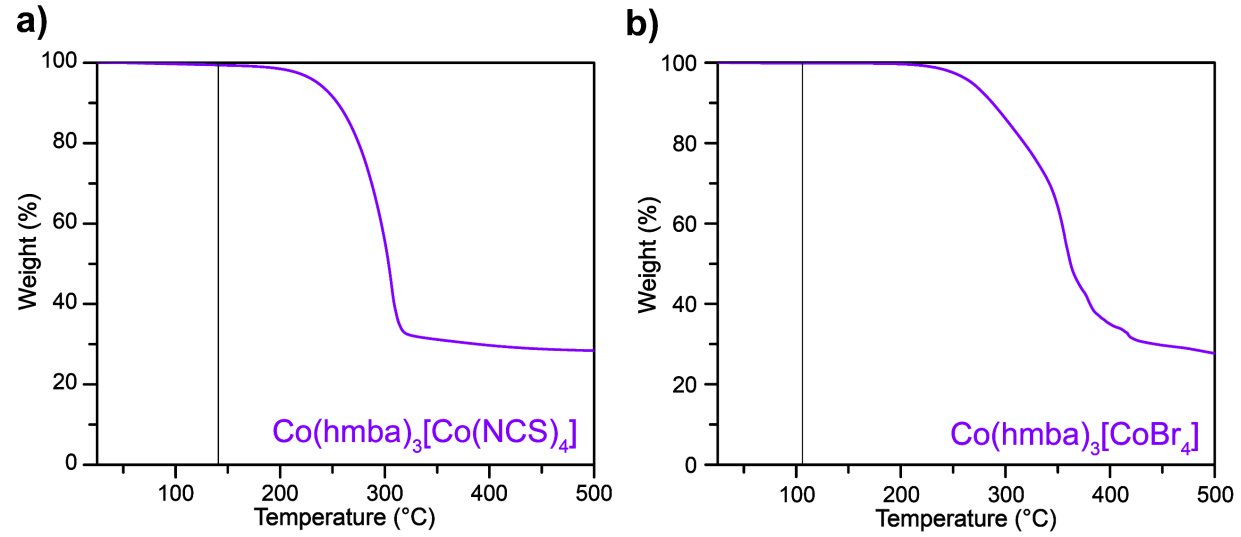

Figure S27. Thermogravimetric analysis of a) $Co(hmba)_3[Co(NCS)_4]$ and b) $Co(hmba)_3[CoBr_4]$ at a heating rate of 5 °C/min. The vertical line indicates T_m as determined by DSC. A decrease of less than 1 wt % was observed at the DSC determined T_m and no significant weight loss was observed until at least 50 °C above T_m of each compound.

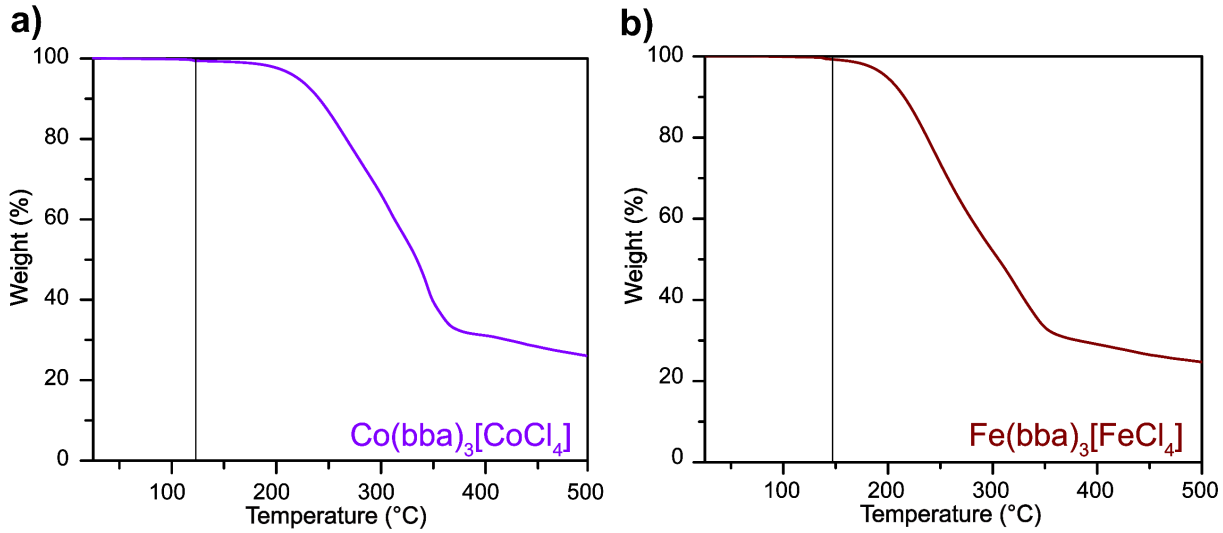

Figure S28. Thermogravimetric analysis of a) $Co(bba)_3[CoCl_4]$ and b) $Fe(bba)_3[CoCl_4]$ at a heating rate of 2 °C/min. The vertical lines indicate T_m as determined by DSC. A decrease of less than 1 wt % was observed prior to the DSC determined T_m of each compound and no significant weight loss was observed until at least 50 °C above T_m for the lower melting $Co(bba)_3[CoCl_4]$ and 25 °C above T_m for the higher melting $Fe(bba)_3[FeCl_4]$.

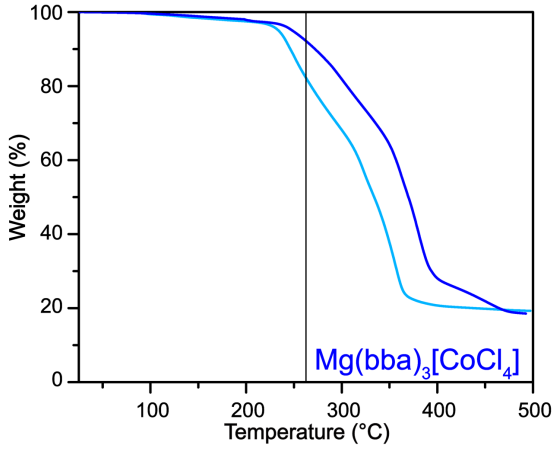

Figure S29. Thermogravimetric analysis of $Mg(bba)_3[CoCl_4]$ at a heating rate of 10 °C/min (dark blue line) and 2 °C/min (light blue line). The vertical line indicates T_m as determined by DSC. A decrease of 7 wt % and 17 wt % prior to the DSC determined T_m was observed at a heating rate of 10 °C/min and 2 °C/min, respectively, demonstrating the impact that the TGA ramp rate can have on the magnitude of weight loss that occurs up to a given temperature. This mass loss is likely due to the volatilization of neutral organic bridging ligands just prior to the melting transition at 260 °C under rapidly flowing N_2. Indeed, $Mg(bba)_3[CoCl_4]$ melts and recrystallizes reversibly without any significant change in enthalpy over at least 3 cycles in a sealed DSC pan (Figure S19), confirming that the mass loss is due to volatilization and not degradation.

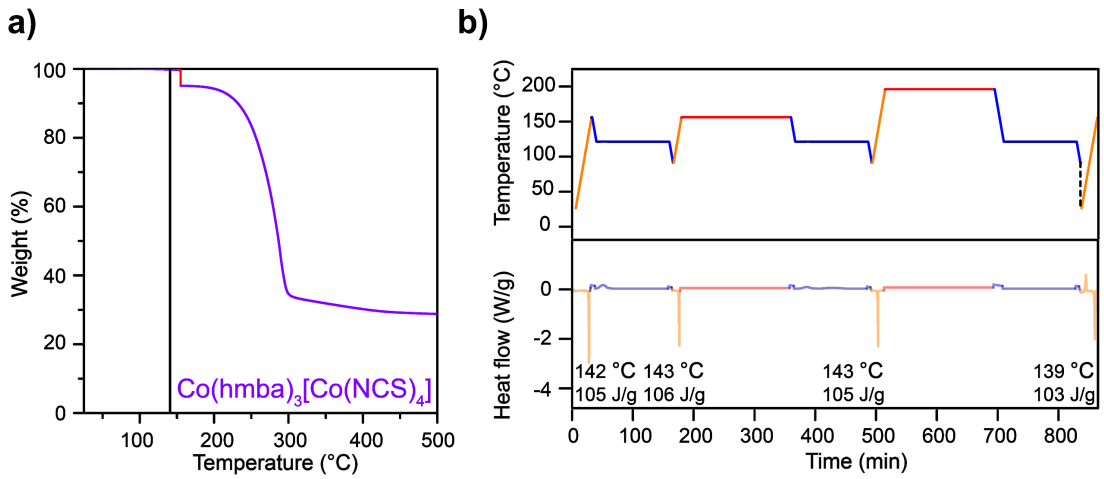

Figure S30. a) Thermogravimetric analysis of $Co(hmba)_3[Co(NCS)_4]$ at a heating rate of 2 °C/min with a 12 h isothermal hold at 155 °C. The vertical line indicates T_m as determined by DSC. b) Thermal stability test of $Co(hmba)_3[Co(NCS)_4]$ by DSC. Top: temperature as a function of time. Bottom: heat flow as a function of time with T_m and ΔH_{fus} labeled for each melting transition. As often observed for mechanochemically synthesized networks (Figure S23), this sample has a slightly lower ΔH_{fus} than reported in Table S14. Here, heating at 5 °C/min, an isothermal hold at $T > T_m$ (at 155 and 195 °C), cooling at 5 °C/min, and an isothermal hold at $T < T_m$ (to allow full recrystallization) are represented by orange, red, blue, and navy lines, respectively. Since minimal recrystallization was observed after the last isothermal hold below T_m, the sample was allowed to sit at room temperature overnight (black dotted line). Importantly, while the liquid does have non-negligible vapor pressure according to the TGA study, reversible melting is observed in sealed environment on DSC after thermal holds at 155 °C and 195 °C for 3h with > 98% of ΔH_{fus} recovered.

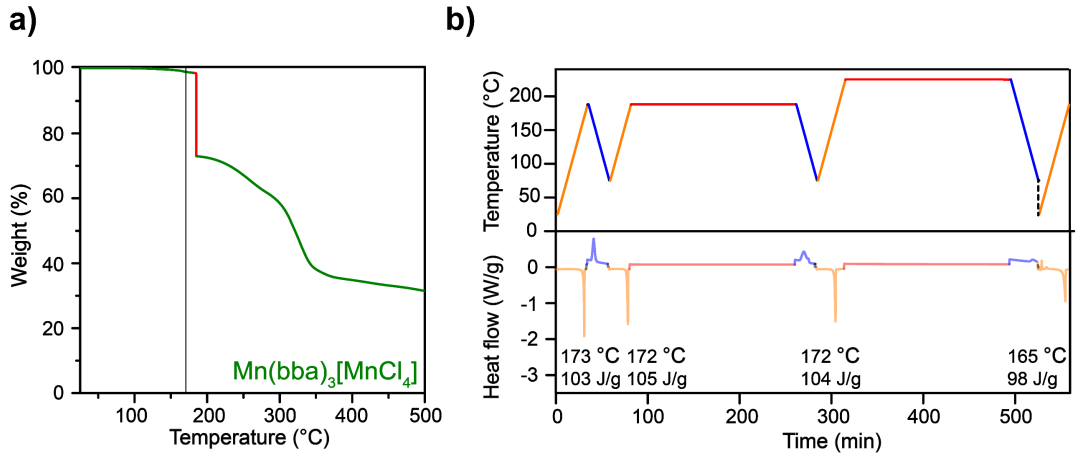

Figure S31. a) Thermogravimetric analysis of $Mn(hmba)_3[MnCl_4]$ at a heating rate of 2 °C/min with a 12 h isothermal hold at 188 °C. The vertical line indicates T_m as determined by DSC and less than 1.5% of weight loss is observed at this temperature. b) Thermal stability test of $Mn(bba)_3[MnCl_4]$ by DSC. Top: temperature as a function of time. Bottom: heat flow as a function of time with T_m and ΔH_{fus} labeled for each melting transition. Heating at 5 °C/min, an isotherm hold at $T > T_m$ (at 188 and 225 °C), and cooling at 5 °C/min are represented by orange, red, and blue lines, respectively. Since minimal recrystallization was observed after the last isothermal hold below T_m, the sample was allowed to sit at room temperature overnight (black dotted line). Importantly, while the liquid does have non-negligible vapor pressure according to TGA study, reversible melting in sealed environment on DSC is observed after thermal holds at 188 °C and 225 °C for 3 h with >95% ΔH_{fus} recovered.

Extended X-ray Absorption Fine Structure (EXAFS)

Variable temperature EXAFS data at the K-edge of Co were collected at beamline 12-BM at the Advanced Photon Source of Argonne National Laboratory.

EXAFS Sample Preparation

Powder samples were sealed in cells that employed spacers made from Al sheets and sealed with Kapton (0.005" thick film, Grainger item #497X99) or PEEK (0.01" thick film, McMaster item # 8504K16) windows. For an example of a sample cell, see Figure S29. The interior length of the sample cell was several hundred microns, which set the sample thickness in the sample cell. To create the cell, a circular hole with a 1/4" inch diameter (larger than the focused X-ray beam spot size) was punched into a piece of Al sheet (Beantown Chemical #222630; thickness = 0.01"), and a Kapton or PEEK window was attached to one side of the Al sheet with double-sided Kapton tape (Electron Microscopy Sciences item #77708-13; thickness 0.004"). Next, the sample was ground with a mortar and pestle under an Ar or N_2 atmosphere, loaded into the sample cell, and flattened and packed using a glass slide. A second piece of Kapton or PEEK window was then attached with a double-sided Al tape to seal the sample. Note that the tape adhesive is rated to be stable up to 400 °C, which is above the melting temperature of both compounds investigated in EXAFS experiments.

EXAFS Experimental Setup

EXAFS experiments were conducted in transmission mode, using gas ionization chamber detectors, with simultaneous collection of foil reference data for Co. A Si(111) water cooled, double crystal, fixed-exit monochromator was used to select energies and the beam was focused to 0.5 × 0.5 mm using a double, flat and toroidal, mirror system. The monochromator was detuned to reduce the intensity of glitches arising from higher order harmonics.

The prepared sample cells were loaded into a temperature controlled Linkam THMS600 stage, which was purged with N_2 gas and cooled with liquid N_2. EXAFS spectra were collected for $Co(bba)_3[CoCl_4]$, $Mg(bba)_3[CoCl_4]$ and $Co(bba)_3Br_2$ at ambient temperature, just below the melting temperature, and just above the melting temperature. In addition, for $Co(bba)_3Br_2$, a spectrum was collected at –5 °C after cooling from the melt. Typically, only one scan, with a collection time of 0.5 s per energy data point, was performed at ambient temperature, but at higher temperatures, two scans were performed and averaged.

The phase of the sample, solid or liquid, was monitored either visually or using wide angle X-ray scattering (WAXS). Specifically, a four-quadrant X-ray detector (MerlinX from Quantum Detectors) was mounted to the transmission detector, downrange from the sample and adjacent to the beam path, to measure diffraction signals from the sample. This setup allowed for the clear observation of X-ray powder diffraction patterns prior to collection of each EXAFS spectrum, confirming whether the sample was crystalline or molten at a given temperature setpoint.

EXAFS spectra and WAXS patterns were initially collected at ambient temperature, followed by heating the Linkam stage to 10 °C below the DSC determined melting point. The sample was then heated to a setpoint 10 °C above the melting point, but frequently melting was not observed at that

temperature. This was likely due to a temperature gradient between the Linkam stage and sample, which could not be easily measured. Therefore, the sample was successively heated by 5–10 °C steps until melting became visually apparent or WAXS patterns showed complete disappearance of the crystalline phase. The temperature was then equilibrated for several minutes, and EXAFS spectra were collected. Sample cells opened after EXAFS data collection showed no signs of degradation.

EXAFS Data Analysis

EXAFS data were analyzed using the IFEFFIT-based Demeter software package and deglitched in Athena prior to further analysis.[39] Reference EXAFS data was collected for Co foil simultaneously with the sample EXAFS signal. The Co reference foil was easily modeled due to its cubic crystal structure, which allows for many paths to be used during fitting with only a small number of fit parameters. A Debye model was used to model the mean square displacement parameters, σ^2, for all scattering paths while the half-path length values, R, for all paths were parameterized to one freely refined isotropic expansion factor, assuming isotropic cubic expansion of the unit cell. In addition, the edge energy shift, ΔE, was freely refined while the degeneracy, or coordination number, N, was fixed to crystallographic values. As described in more detail below, these reference foil fits were then conducted in two ways: 1) fitting to determine the amplitude reduction factor, S_0, and 2) fitting to determine S_0 while also refining an imaginary energy correction, E_i.

The Artemis software, along with Atoms and FEFF6, was used to calculate scattering paths for data modeling.[39,40] In all cases, only first shell scattering around the Co metal centers were considered and the paths were calculated using both crystal structures and the quick first shell tool in Artemis. The quick first shell calculates a first shell scattering path between the absorber and scatterer using the supplied distance by constructing a fictious crystal containing the two elements and keeping only the first single scattering path between the two elements. This supplied distance was approximated using similar structures and then refined.[41] We found that first shell, single scattering fits were sufficient to obtain first shell coordination information in the melt for $Co(bba)_3Br_2$, $Mg(bba)_3[CoCl_4]$, and $Co(bba)_3[CoCl_4]$.

We observed that fits at ambient temperature using S_0 determined from the foil standards produced unphysical results. Specifically, fits that fixed the coordination number, N, to the known solid-state structure while using a fixed S_0 from the foil were poor. Under these conditions, when N was allowed to freely refine for ambient temperature data, it refined to non-physical values above the expected solid-state coordination number. Alternatively, if the room temperature structures with fixed crystallographic N were used as standards to determine S_0 instead of the foil data, this produced S_0 values well outside the normal range of 0.7 to 1.0.[42]

In these cases, modeling E_i as a free parameter in addition to using foil-determined S_0 values produced more physical results for the metal–organic complexes studied here. The procedure we employed was as follows: S_0 was fixed at ambient temperature for the samples, while E_i was freely refined. The choice of S_0 for our sample models, given that the Co foil was modeled both with and without E_i, requires further explanation. Different foil models were used depending on the sample model because S_0 should remain constant for a given metal while E_i may be sensitive to the coordination environment.[43] When E_i is not modeled for the foil, the coordination environment

dependence of E_i may be folded into S_0, which is otherwise primarily metal dependent. Given that the metal coordination environment is very different in the foil and coordination complexes, consistent usage of S_0 and E_i between foils and samples, when possible, was preferred. Therefore, when the foil modelling allowed, S_0 used for sample modeling was fixed to the value from the corresponding foil model that also refined an E_i. For sample ambient temperature fits, E_i was the free to vary from the foil model value and S_0 was fixed. Finally, for higher temperature sample modeling E_i was subsequently fixed to the ambient temperature refined value, using the ambient temperature sample data as internal standards for E_i and foil data as a standard for S_0

Fitting EXAFS Data of $Mg(bba)_3[CoCl_4]$ and $Co(bba)_3Br_2$

Having chosen and fixed S_0 for the sample fits, single scattering path fits were pursued for both complexes with N fixed to crystallographic coordination numbers in the ambient temperature fits while R, σ^2, ΔE, and E_i were freely refined. Specifically, N was fixed to 6 O scatterers for $Co(bba)_3Br_2$ at ambient temperature and 4 Cl scatters for $Mg(bba)_3[CoCl_4]$ at ambient temperature. For data at higher temperatures, E_i was then fixed to the value determined for each compound in the ambient temperature fit, while R, σ^2, ΔE, and N were refined freely. The fitting of the $Co(bba)_3Br_2$ melt and −5 °C data required the addition of a second single scattering path, while the $Mg(bba)_3[CoCl_4]$ melt data could be modelled with only a single scattering path.

Since ligand disorder in $Mg(bba)_3[CoCl_4]$ leads to partial site occupancy in the crystal structure, precluding its use as a theoretical standard in Artemis, the Co–Cl scattering path was calculated using the quick first shell tool with a pathlength estimated from the crystal structure. The higher temperature fits used a fixed E_i and S_0 while R, σ^2, N, ΔE, and a third cumulant (C_3) were freely refined. The resulting fits are shown in Figure S33 and the refinement results are shown in Table S18.

Fitting of both the melt and −5 °C $Co(bba)_3Br_2$ data required the addition of a Co–Br scattering path to the first coordination sphere, which was again calculated using the quick first shell tool with a pathlength estimated from the $Mn(hmba)_3[MnBr_4]$ structure.[3] For both the Co–O and the Co–Br paths, E_i were fixed to the same value determined from the ambient fit, and S_0 was fixed to the value previously determined for the foil. With E_i and S_0 fixed accordingly, each path was then assigned separate freely refined R, σ^2, and N parameters, while both paths were constrained to have the same, freely refined ΔE (Figure S33, Table S19).

The fitting method of using one single E_i mode in the presence of two distinct coordination environments is in contrast to fits of $Co(bba)_3[CoCl_4]$ discussed below, where separate E_i values were employed for the Co–O and Co–Cl centers. The single E_i strategy was used for $Co(bba)_3Br_2$ for two reasons. First, using only one joint E_i for both the Co–O and Co–Br paths produced satisfactory fits. Second, in contrast to $Co(bba)_3[CoCl_4]$, where the separate E_i values were obtained by fitting known standards containing the particular coordination environment, we did not collect data on a sample containing a known Co–Br environment and therefore were unable to obtain an appropriate separate E_i for a known Co–Br coordination center.

Alternative Approaches to Fitting EXAFS Data

To evaluate how different ways of fitting the EXAFS data impacted the refined coordination number changes during the melting and cooling processes, we remodeled the data for all compounds without including E_i during any part of the fitting process and used S_0 values fixed to those from reference foil models refined without refining E_i (Figure S34, Table S20, S21). As mentioned above, the ambient temperature fits with these fixed S_0 values, however, showed poor agreement between the model and experimental spectra when N was fixed at the crystallographic coordination number, 4 for the Co–Cl path in $Mg(bba)_3[CoCl_4]$ and 6 for the Co–O path in $Co(bba)_3Br_2$. Therefore, we allowed N, along with σ^2, ΔE, and R to vary freely at ambient temperature with a fixed S_0. EXAFS data from the melt were then fit using the same free parameters, along with a freely refined C_3 when its inclusion improved the model. The relative percent change in coordination number upon melting was then calculated as $(N_{solid} - N_{melt})/N_{solid}$. A percent change cannot be calculated for the Co–Br path in the melt and −5 °C fits for $Co(bba)_3Br_2$ because a Co–Br path is not present in the ambient temperature model. The percent decreases in coordination number for this S_0-only model produced values for N in the melt that were indistinguishable (within error) from the fitting procedure described above that included both S_0 and E_i, supporting the validity of the models using E_i (Tables S20–22).

Fitting EXAFS Data of $Co(bba)_3[CoCl_4]$

The fitting of $Co(bba)_3[CoCl_4]$ EXAFS data is more challenging compared to $Mg(bba)_3[CoCl_4]$ and $Co(bba)_3Br_2$ because there are two chemically distinct Co metal centers with first shell single-scattering paths, Co–O and Co–Cl, that share very similar scattering path lengths. Since the $Mg(bba)_3[CoCl_4]$ data shows that the N of the Co–Cl path does not change during melting, we are able to model the Co–O scattering signal even though it is lower in intensity than the Co–Cl signal due to the higher electron density of Cl atom relative to O atom. The coupling of fit parameters between the two paths, due to their spatial overlap, combined with the low signal of the Co–O path, however, required slightly different data analysis and fitting strategies to those described above in order to evaluate the coordination environments of Co centers in $Co(bba)_3[CoCl_4]$. Overall, EXAFS data was modeled for the liquid state, along with data of the solid state at ambient temperature and just below melting temperature as internal standards.

The data analysis for $Co(bba)_3[CoCl_4]$ differed from the other EXAFs analyses reported here in the choice of a lower R background, R_{bkg}, a parameter that filters out lower R signals from the Fourier transform of the k-space EXAFS data. This change was required because while the R of the Co–O path is smaller than the Co–Cl path, its amplitude in R-space overlaps with the shoulder of the more strongly scattering Co–Cl path (Figure S35), which compromises the quality of the fit to the Co–O path. As such, the R_{bkg} was lowered to 0.8 Å along with the lower limit of R for fitting. In addition, the upper limit of the fitting range was chosen to be 2.2 Å, which includes most of the Co–Cl and Co–O paths but avoids including higher R, second shell single and multiple scattering paths that contribute more prominently above 2.2 Å.

For data fitting, ligand disorder leading to partial site occupancy in the $Co(bba)_3[CoCl_4]$ crystal structure, similar to $Mg(bba)_3[CoCl_4]$, precluded its use as a theoretical standard in Artemis. Instead, an unpublished crystal structure of an ordered zero-dimensional analog of

$Co(bba)_3[CoCl_4]$, $Co(CH_3CONH_2)_6[CoCl_4]$, was used as a theoretical standard to generate first shell scattering paths instead.

Though the crystallographic coordination numbers of Cl and O scatterers are 4 and 6, respectively, the EXAFS fitting parameter N is an average over all Co metal centers, only half of which contribute to each scattering path. To account for the two distinct Co metal centers, the N of O scatterers was fixed to 3 instead of 6 and the N of Cl scatters was fixed to 2 instead of 4 in the ambient temperature and high-temperature solid-state fits. Both the Co–Cl and Co–O single scattering paths were initially freely refined with one E_i and ΔE shared between both paths, along with R and σ^2 for each path. With this set of free parameters, however, the ambient temperature and high-temperature solid-state fits returned inaccurate distances for the Co–O scattering path and large errors for all free parameters. Although the correlation coefficients returned by the fit between the free parameters were within the limits of acceptability of the Artemis software, we observed that the free parameters of the two scattering paths were highly coupled, presumably due to the spatial overlap of the two paths. A fitting strategy to better model the distinct coordination environments around Co centers was therefore pursued.

The two Co coordination environments in $Co(bba)_3[CoCl_4]$, CoO_6 octahedra and $CoCl_4$ tetrahedra, are present separately in $Co(bba)_3Br_2$ and $Mg(bba)_3[CoCl_4]$, respectively, at ambient temperature. Therefore, with the expectation that E_i may also have a coordination environment dependence, E_i was split into two parameters for the Co–O and Co–Cl paths in $Co(bba)_3[CoCl_4]$, and each was fixed using $Mg(bba)_3[CoCl_4]$ and $Co(bba)_3Br_2$ as standards (Tables S18, 19). Specifically, the E_i of the Co–O path in $Co(bba)_3[CoCl_4]$ was fixed to −0.62 eV, as determined from the ambient temperature fit of $Co(bba)_3Br_2$, and the E_i of the Co–Cl path was fixed to 0.31 eV, as determined from the ambient temperature fit of $Mg(bba)_3[CoCl_4]$.

As our initial determination of E_i is sensitive to the choice of parameters used to model these standards, the choice of these specific E_i values, −0.62 eV for Co–O path and 0.31 eV for Co–Cl path, requires further clarification. First, in our $Co(bba)_3[CoCl_4]$ models a C_3 is not employed for the Co–Cl path, but the E_i reported for the $Mg(bba)_3[CoCl_4]$ fit (Table S18) was determined using a C_3 free parameter. Therefore, to determine an E_i appropriate for the Co–Cl path of $Co(bba)_3[CoCl_4]$, the ambient temperature $Mg(bba)_3[CoCl_4]$ data was refit without C_3 to determine a new E_i of 0.31 eV. Similarly, E_i was determined with and without C_3 for $Co(bba)_3Br_2$, the introduction of which did not alter the fit and returned an E_i of −0.62 eV in both cases.

With E_i fixed accordingly and N fixed to crystallographic values, two fitting methods were attempted at ambient temperature and just below the melting temperature with the free and fixed parameters outlined in Table S17. The primary distinction between the two models is the addition of a C_3 to the Co–O path in the second set of models. In addition, the $R_{Co–Cl}$ remains at the initial distance after free refinement in the second model, so the $R_{Co–Cl}$ is fixed in addition to including C_3. The resulting fits of both models are shown in Figure S35, and the refinement results are shown in Tables S23. Although both models were in good agreement with the experimental data, the inclusion of a C_3 parameter led to a $R_{Co–O}$ that was in better agreement with the expected crystallographic distance and provided a better statistical fit. These ambient temperature and high-temperature solid state models thus validated the use of the two split E_i values and served as internal standards for analysis of the melt data.

To evaluate whether Co–O coordination is maintained in the liquid state, a crucial aspect of the network-forming nature of these liquids, we performed a comparative study using three EXAFS fitting approaches for molten $Co(bba)_3[CoCl_4]$. In each model, $N_{Co–Cl}$ was fixed to 2, as $Mg(bba)_3[CoCl_4]$ EXAFS analysis showed that full coordination of $[CoCl_4]^{2–}$ was maintained upon melting. If all Co–O coordination bonds fully dissociate upon melting and no connectivity is preserved in the liquid state, the Co–Cl path alone should adequately describe first shell scattering signals. As such, we first attempted to fit without a Co–O path. The S_0, E_i, $N_{Co–Cl}$ parameters were fixed as in the ambient and high-temperature solid state fits and $\sigma^2_{Co–Cl}$, ΔE, and $R_{Co–Cl}$ were freely refined. This yielded a visually and statistically poor fit with a high R value of 17%, indicating the necessity of a Co–O path in the melt to satisfactorily fit the data and therefore the existence of Co–O coordination in the liquid state (Figure S35c).

To quantify the extent of Co–O coordination in the melt, the Co–O path was reintroduced for the second and third melt models. As before, the parameters of the Co–Cl and Co–O path can couple, which was exacerbated with the $N_{Co–Cl}$ path being freely refined in the melt, resulting in large errors for all free parameters and unphysically small σ^2 values. To reduce the errors and obtain a better sense of $N_{Co–O}$ in the melt, $\sigma^2_{Co–O}$, which can be highly correlated to N and influence R, was fixed in both models to the value determined in the high-temperature solid state dataset, which should represent a lower limit for σ^2 in the melt assuming that $\sigma^2_{Co–O}$ increases upon further heating and melting. As a higher $\sigma^2_{Co–O}$ would require a larger $N_{Co–O}$ to compensate for amplitude loss, a freely refined $N_{Co–O}$ with a $\sigma^2_{Co–O}$ fixed to the value determined for the high-temperature solid state should therefore represent the lower limit of N in the melt. In addition, the inclusion of C_3 for the Co–O path, though requiring an additional parameter, was observed to similarly improve fitting statistics, as for both solid-state datasets. The treatment of C_3 slightly differed in the second and third melt models, where it was fixed to the high-temperature solid state value in the former and freely refined in the later. Since no statistically significant difference was observed for the quality of the two fits (F-test value <1),[44] both are reported here. A summary of the fixed and free parameters in each fit is provided in Table S17, and the fits and refinement results are shown in Figure S35 and Table S23.

Compared to the first model without a Co–O path, inclusion of the Co–O path significantly improves the agreement between predicted and experimental EXAFS spectra, as evidenced visually (Figure S35) and by F-test values for the second and third models of 36 and 22, respectively. Both models yield consistent results for the Co–O coordination number with $N_{Co–O}$ = 4.8(7) for the second model with a fixed C_3 and $N_{Co–O}$ = 5.3(1.0) for the third model with a freely refined C_3. Given the errors in N that are typical of correlated parameters in EXAFS analysis, the actual average $N_{Co–O}$ in the liquid state is likely an intermediate value between 4.8 and 5.3. The 4.8(7) value is highlighted in the main text as it represents a lower limit and entails smaller error.

Table S17. Summary of fixed and free parameters in fits for $Co(bba)_3[CoCl_4]$ data.

Fits	Fixed Parameters	Free Parameters
Ambient T and high-T solid state without C_3	$E_{i,Co–O}$, $E_{i,Co–Cl}$, S_0, $N_{Co–O}$ $N_{Co–Cl}$	$\sigma^2_{Co–O}$, $\sigma^2_{Co–Cl}$, $R_{Co–Cl}$, $R_{Co–O}$, ΔE
Ambient T and high-T solid state with C_3	$E_{i,Co–O}$, $E_{i,Co–Cl}$, S_0, $N_{Co–O}$ $N_{Co–Cl}$, $R_{Co–Cl}$	$\sigma^2_{Co–O}$, $\sigma^2_{Co–Cl}$, $R_{Co–O}$, ΔE, $C_{3,Co–O}$
Melt no C–O path	$E_{i,Co–Cl}$, S_0, $N_{Co–Cl}$	$\sigma^2_{Co–Cl}$, $R_{Co–Cl}$, ΔE
Melt with fixed C_3	$E_{i,Co–O}$, $E_{i,Co–Cl}$, S_0, $N_{Co–Cl}$, $\sigma^2_{Co–O}$, $C_{3,Co–O}$	$\sigma^2_{Co–Cl}$, $R_{Co–O}$, $R_{Co–Cl}$, ΔE, $N_{Co–O}$
Melt with free C_3	$E_{i,Co–O}$, $E_{i,Co–Cl}$, S_0, $N_{Co–Cl}$, $\sigma^2_{Co–O}$	$\sigma^2_{Co–Cl}$, $R_{Co–O}$, $R_{Co–Cl}$, ΔE, $N_{Co–O}$, $C_{3,Co–O}$

Figure S32. Example EXAFS sample cell using aluminum sheet and Kapton windows. The sample is in supercooled liquid state after running EXAFS experiments at elevated temperature.

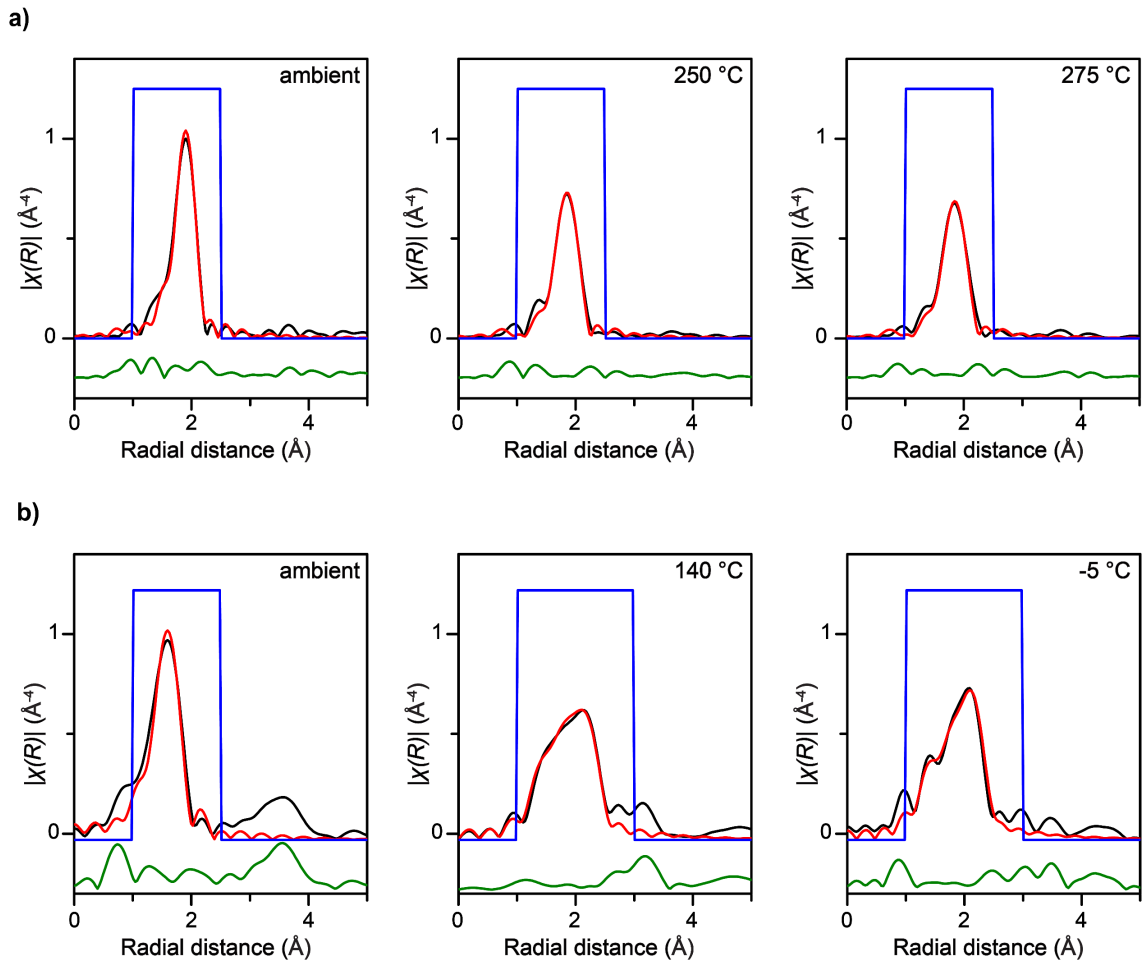

Figure S33. EXAFS models for a) $Mg(bba)_3[CoCl_4]$ (T_m = 260 °C) and b) $Co(bba)_3Br_2$ (T_m = 120 °C) compounds at various temperatures. Black traces correspond to experimental data, while red traces represent the fits, with residuals shown in green. The fitting windows (blue) are chosen from to 1 to 2.5 Å for all $Mg(bba)_3[CoCl_4]$ fits and for the ambient $Co(bba)_3Br_2$. The higher temperature $Co(bba)_3Br_2$ fit uses a window from 1 to 3 Å to enable fitting of the Co–Br scattering path. These fits are performed using a model incorporating an imaginary energy correction, E_i, and a fixed N at ambient temperature, with the results shown in Tables S18, 19.

Table S18. Table of EXAFS fitting parameters, fitting ranges, and fit results for $Mg(bba)_3[CoCl_4]$ in the solid state, both at ambient temperature and 10 °C below the melting temperature, and in the melt, 15 °C above the melting temperature, corresponding to the data in Figure S33a. Standard errors are included for all refined parameters. Here, S_0 values were fit using data from a reference Co foil and then fixed. In addition, the total coordination number was fixed at N = 4 at ambient temperature (based on the known crystal structure) and the imaginary energy correction, E_i, was varied along with other standard fitting parameters. Subsequently, the E_i obtained from ambient temperature data was fixed during fitting of the melt data, while N was freely refined.

***T* (°C)**	**Path**	**σ^2 (Å^2)**	***R* (Å)**	**Δ*E* (eV)**	**S_0**	***N***	**% change of *N***	**E_i (eV)**	**C_3**	**R value (%)**	***k* range (Å^{-1})**	**R range (Å)**
Ambient (solid)	Cl	0.0042(7)	2.294(17)	6.2(1.2)	0.95	4	-	0.3(6)	0.0001(3)	1.43	2.1 to 14.5	1 to 2.5
250 (solid)	Cl	0.0067(12)	2.31(3)	6.6(1.5)	0.95	4.2(5)	5(13)	0.3	0.0004(4)	1.16	2.1 to 12.5	1 to 2.5
275 (melt)	Cl	0.0076(12)	2.31(3)	6.7(1.5)	0.95	4.3(6)	6(15)	0.3	0.0005(4)	1.18	2.1 to 12.5	1 to 2.5

Table S19. Table of EXAFS fitting parameters, fitting ranges, and fit results for $Co(bba)_2Br_2$ in the solid state at ambient temperature, in the melt 20 °C above the melting temperature, and after cooling the melt –5 °C corresponding to the data in Figure S33b. Standard errors are included for all refined parameters. Here, S_0 values were fit using data from a reference Co foil and then fixed. In addition, the total coordination number was fixed at the crystallographic N = 6 at ambient temperature and the imaginary energy correction, E_i, was varied along with other standard fitting parameters. Subsequently, the E_i obtained from ambient temperature data was fixed during fitting of the melt data, while N was freely refined.

***T* (°C)**	**Path**	**σ^2(Å^2)**	***R* (Å)**	**Δ*E* (eV)**	**S_0**	***N***	**% change of *N***	**E_i (eV)**	**C_3**	**R value (%)**	***k* range (Å^{-1})**	**R range (Å)**
Ambient (solid)	O	0.0066(13)	2.078(12)	−0.6(1.7)	0.95	6	-	−0.6(8)	N/A	1.48	2 to 11	1 to 2.5
140 (melt)	O	0.005(3)	1.974(14)	2.0(1.4)	0.95	1.7(3)	−72(5)	−0.6	N/A	0.98	2.6 to 11.25	1 to 3.0
	Br	0.0074(18)	2.392(9)			2.1(5)						
−5 (melt cooling)	O	0.009(4)	2.032(19)	−3.2(1.7)	0.95	2.8(6)	−53(10)	−0.6	N/A	1.66	2.3 to 12	1 to 3.0
	Br	0.006(3)	2.40(1)			1.6(5)						

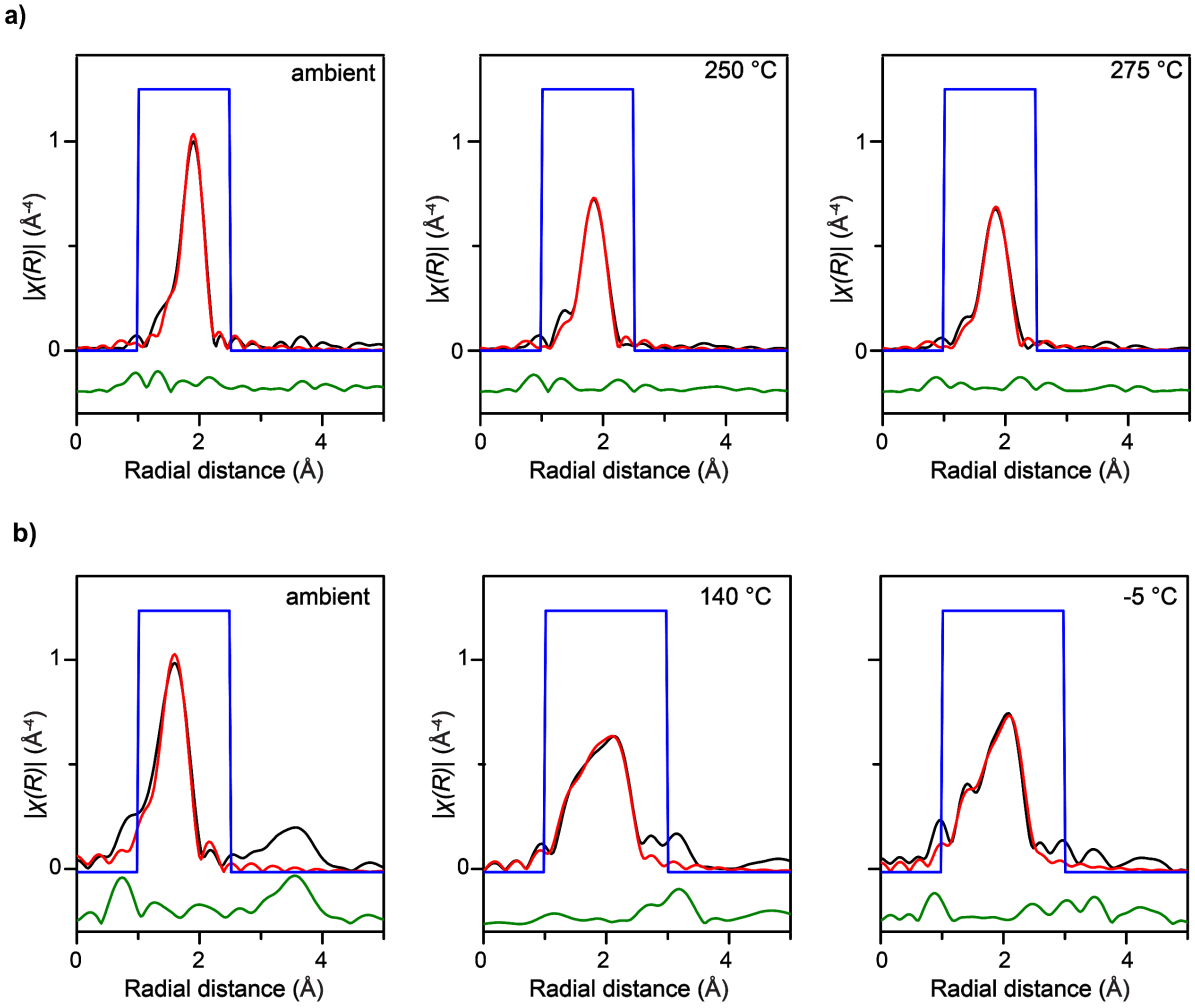

Figure S34. EXAFS models for a) $Mg(bba)_3[CoCl_4]$ (T_m = 260 °C) and b) $Co(bba)_3Br_2$ (T_m = 120 °C) complexes at various temperatures. Black traces correspond to experimental data, while red traces represent the fits, with residuals shown in green. The fitting windows (blue) are chosen from to 1 to 2.5 Å for all $Mg(bba)_3[CoCl_4]$ fits and for the ambient $Co(bba)_3Br_2$. The higher temperature $Co(bba)_3Br_2$ use a window from 1 to 3 Å to enable fitting of the Co–Br scattering path. These fits use S_0, without E_i, and feely refine N at room temperature, with the results shown in Tables S20, 21.

Table S20. Table of EXAFS fitting parameters, fitting ranges, and fit results for $Mg(bba)_3[CoCl_4]$ in the solid state, both at ambient temperature and 10 °C below the melting temperature, and in the melt, 15 °C above the melting temperature, corresponding to the data in Figure S34a. Standard errors are included for all refined parameters. Here, S_0 values were fit using data from a reference Co foil and then fixed. In these fits, fixing the coordination number at 4 at room temperature often gave poor results, so N was freely refined at all temperatures. Though non-physical coordination numbers greater than 4 emerge, the percent changes in N roughly match the coordination number changes observed in the fits using E_i in Table S18.

T (°C)	Path	σ^2 (Å^2)	R (Å)	ΔE (eV)	S_0	N	% change of N	C_3	R value (%)	k range (Å^{-1})	R range (Å)
Ambient (solid)	Cl	0.0043(10)	2.297(17)	6.3(1.2)	0.78	4.8(4)	-	0.0002(3)	1.37	2.1 to 14.5	1 to 2.5
250 (solid)	Cl	0.0065(12)	2.31(3)	6.6(1.4)	0.78	4.9(5)	3(10)	0.0004(3)	1.21	2.1 to 12.5	1 to 2.5
275 (melt)	Cl	0.0074(13)	2.31(3)	6.7(1.5)	0.78	5.1(5)	6(10)	0.0005(4)	1.35	2.1 to 12.5	1 to 2.5

Table S21 Table of EXAFS fitting parameters, fitting ranges, and fit results for $Co(bba)_3Br_2$ in the solid state at ambient temperature, in the melt 20 °C above the melting temperature, and after cooling the melt –5 °C corresponding to the data in Figure S34b. Standard errors are included for all refined parameters. Here, S_0 values were fit using data from a reference Co foil and then fixed. In these fits, fixing N to the crystallographic coordination number often gave poor results, so N was allowed to vary. Though non-physical coordination numbers greater than 6 emerge, the percent changes in N roughly matches the coordination number changes observed in the fits using E_i in Table S19.

T (°C)	Path	σ^2 (Å^2)	R (Å)	ΔE (eV)	S_0	N	% change of N	C_3	R value (%)	k range (Å^{-1})	R range (Å)
Ambient (solid)	O	0.0073(17)	2.079(11)	−0.6(1.0)	0.78	8.2(9)	-	N/A	1.30	2 to 11	1 to 2.5
140 (melt)	O	0.005(3)	1.975(15)	2.0(1.5)	0.78	2.3(5)	−72(7)	N/A	1.06	2.6 to 11.25	1 to 3.0
	Br	0.0077(19)	2.392(9)			2.8(7)					
−5 (melt cooling)	O	0.010(4)	2.033(19)	−3.2(1.7)	0.78	3.8(8)	−54(10)	N/A	1.69	2.3 to 12	1 to 3.0
	Br	0.006(2)	2.40(1)			2.2(6)					

Table S22. Results of N for M–O path across two EXAFS models for $Mg(bba)_3[CoCl_4]$ and $Co(bba)_3Br_2$ at various temperatures. The N values in the S_0-free ambient N model are determined using the percent change in value between the ambient and melt versions of the model.

Compound	Temperature (°C)	S_0 and E_i (Figure S33)	S_0-free ambient N (Figure S34)
$Mg(bba)_3[CoCl_4]$	250	4.2 (5)	4.1 (5)
	275	4.3 (6)	4.3 (5)
$Co(bba)_3Br_2$[a]	140	3.4 (6)	3.4 (7)
	−5	5.6 (1.2)	5.6 (1.2)

[a]The N values for $Co(bba)_3Br_2$ describes the change in 50% of the metal centers that remain in coordination with carbonyl O atoms of bba ligand (Figure S12).

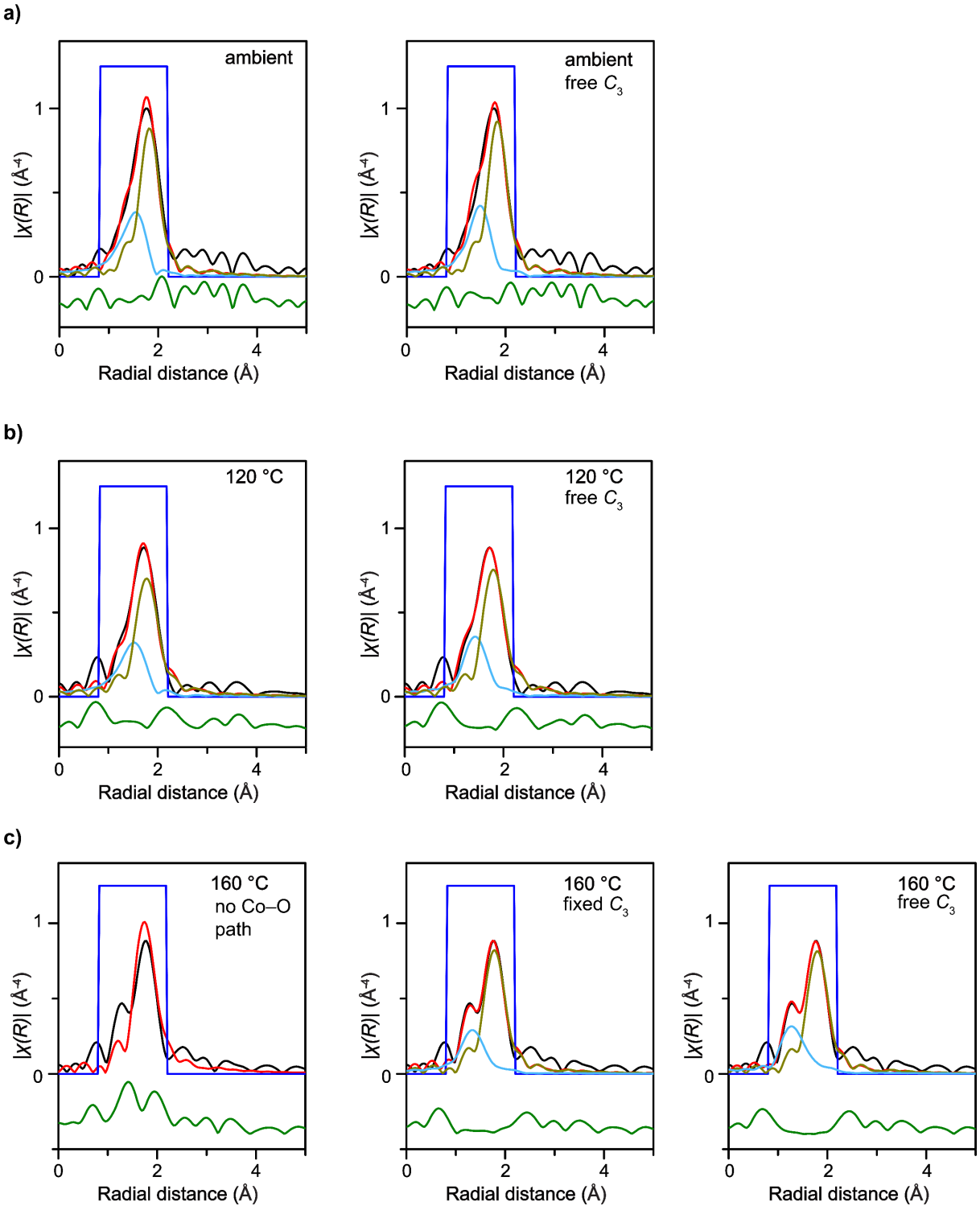

Figure S35. EXAFS models for $Co(bba)_3[CoCl_4]$ (T_m = 124 °C) at a) ambient temperature, b) 120 °C, and c) 160 °C. Black traces correspond to experimental data, while red, blue, and dark yellow traces represent the overall, Co–O, and Co–Cl fits, respectively, and residuals are shown in green. The fitting windows (blue) are chosen from to 0.8 to 2.2 Å for all $Co(bba)_3[CoCl_4]$ fits. These fits are performed using a model incorporating an imaginary energy correction, E_i, and a fixed N at ambient temperature and 120 °C for each path, with the results shown in Table S23.

Table S23. Table of EXAFS fitting parameters, fitting ranges, and fit results for $Co(bba)_3[CoCl_4]$ in the solid state, both at ambient temperature and 4 °C below the melting temperature, and in the melt at 36 °C above the melting temperature, corresponding to the data in Figure S35. Standard errors are included for all refined parameters. Here, S_0 values were fit using data from a reference Co foil and then fixed. In addition, the total coordination number was fixed at $N = 3$ for the Co–O path and at $N = 2$ for the Co–Cl path at ambient temperature as well at 120 °C (based on the known crystal structure), and the imaginary energy correction, E_i, was fixed to values previously determined with similar coordination environment for each path. Two fits were attempted ambient temperature and 120 °C. Fit 2 differed from fit 1 in fixed R for Co–Cl path and freely refined C^3 for Co–O path. In the melt, three different fits were attempted, with fit 1 excluding the Co–O path. Fits 2 and 3 in the melt contain a fixed or freely refined C_3 for Co–O path, respectively, with other fitting parameters kept identical.

T (°C)	Path	σ^2 (Å^2)	R (Å)	ΔE (eV)	S_0	N	% change of N	E_i (eV)	C_3	R value (%)	k range (Å^{-1})	R range (Å)
Ambient (solid)–fit1	O	0.011(5)	2.05(5)	−3.5(3.0)	0.95	3	-	−0.62	N/A	1.89	2.0 to 12.5	0.8 to 2.2
	Cl	0.0040(18)	2.262(15)			2	-	0.31	N/A			
Ambient (solid)–fit2	O	0.011(28)	2.08(4)	−2.5(1.5)	0.95	3	-	−0.62	0.0010(12)	1.71	2.0 to 12.5	0.8 to 2.2
	Cl	0.0037(12)	2.2675			2	-	0.31	N/A			
120 (solid)–fit1	O	0.0136(9)	2.05(7)	−4.1(4.7)	0.95	3	-	−0.62	N/A	1.65	2.0 to 10.75	0.8 to 2.2
	Cl	0.005(3)	2.258(20)			2	-	0.31	N/A			
120 (solid)–fit2	O	0.0127(4)	2.11(4)	−2.6(1.6)	0.95	3	-	−0.62	0.0020(17)	1.19	2.0 to 10.75	0.8 to 2.2
	Cl	0.0043(15)	2.2675			2	-	0.31	N/A			
160 (melt)–fit1	Cl	0.003(2)	2.21(4)	−9.2(4.7)	0.95	2	-	0.31	N/A	16.6	2.2 to 11.5	0.8 to 2.2
160 (melt)–fit2	O	0.0127	2.02(4)	−4.2(2.0)	0.95	4.8(7)	20(12)	−0.62	0.0020	0.57	2.2 to 11.5	0.8 to 2.2
	Cl	0.0042(9)	2.243(12)			3	-	0.31	N/A			
160 (melt)–fit3	O	0.0127	2.08(7)	−2.4(2.9)	0.95	5.3(1.0)	12(17)	−0.62	0.0035(17)	0.54	2.2 to 11.5	0.8 to 2.2
	Cl	0.0043(10)	2.251(16)			3	-	0.31	N/A			

Table S24. Table of EXAFS chi-square values, independent points, and number of variables for $Co(bba)_3[CoCl_4]$ fits reported in Table S23.

T (°C)	χ^2	Independent Points	Number of Variables
Ambient (solid)–fit1	3034	9.0	5
Ambient (solid)–fit2	2664	9.0	5
120(solid)–fit1	5317	7.5	5
120(solid)–fit2	3782	7.5	5
160(melt)–fit1	17709	7.9	3
160(melt)–fit2	699	7.9	5
160(melt)–fit3	513	7.9	6

Pair Distribution Function (PDF) Analysis

Experimental Setup and Data Analysis Methods

Total scattering experiments were carried out on $Co(bba)_3[CoCl_4]$ at the XPD line at NSLS-II at Brookhaven National Laboratory using the rapid acquisition PDF method (RAPDF).[45] A 2D Perkin Elmer amorphous silicon detector was placed 225 mm behind the samples which were loaded in 1-mm borosilicate capillaries. The incident wavelength of the X-rays was $\lambda = 0.1892$ Å. Calibration of the experimental setup was done using nickel as a calibrant. To prepare samples for total scattering experiments, $Co(bba)_3[CoCl_4]$ crystals were ground finely with a mortar and pestle under a N_2 atmosphere and then loaded into the capillaries. In addition to a capillary containing the as-synthesized crystalline powder, a second capillary ("pre-melted") was prepared by heating the sample in a sand bath under a N_2 atmosphere above the $Co(bba)_3[CoCl_4]$ melting temperature in order to reduce sample movement upon melting during variable-temperature data collection. All capillaries were flame-sealed to avoid air exposure. Total scattering data of an empty 1-mm borosilicate capillary was collected to determine the background intensity, which was subtracted from the sample intensity during data processing.

During the variable temperature experiments, both as-synthesized and pre-melted samples were heated using a flowing nitrogen cryostream from 25 °C to 190 °C. X-ray scattering patterns were collected every 3 °C, and the temperature ramp rate between measurements was 8 °C/min. Due to the small size of the cryostream, only a small portion of the capillary is in direct contact with the heat source, which is expected to lead to a temperature gradient within the sample and a sample temperature that is lower than the temperature setpoint of the cryostream.

Raw data were summed and corrected for polarization effects before being integrated along arcs of constant angle to produce 1D powder diffraction patterns using the xPDFsuite program.[46] Corrections for air and Compton scattering were then made to the data and normalizations carried out to obtain the total scattering reduced structure function, $F(Q)$, which was Fourier transformed to obtain the PDF using PDFgetX3 within xPDFsuite.[47] The maximum range of data used in the Fourier transform (Q_{max}, where $Q = 4\pi\sin\theta/\lambda$ is the magnitude of the momentum transfer on scattering) was 21.0 $Å^{-1}$.

Structural modeling for the sample was carried out using the Diffpy-CMI complex modeling framework.[48] The parameters for instrument resolution, Q_{damp} and Q_{broad}, were obtained through refining the calibrant nickel PDF. For this sample, $Q_{damp} = 0.0305$ $Å^{-1}$ and $Q_{broad} = 0.0129$ $Å^{-1}$. The low-r range (1.0–6.0 Å) and the high-r range (6.0–30.0 Å) were fit separately. For the low-r region, molecular models consisted of a series of systematically deconstructed chunks from the crystal model. The parameters varied in the refinement were isotropic thermal displacement parameters (U_{iso}) for each element, isotropic lattice expansion, and global scale factor. Additionally, the following empirical correction to the baseline, $c\left(\frac{1}{e^{\frac{a-r}{b}}} - 1\right)r$, was added where r is interatomic distance and a, b and c are parameters varied in the fitting. This correction was added to correct for inconsistencies in the baseline because of the cut-off of small angle scattering from using the Debye equation to generate PDF for the molecular model.

For the high-r range, we used a crystal model to fit the PDF of the sample. The parameters varied for this model were isotropic thermal displacement parameters for each element, isotropic lattice

expansion, global scale factor, and peak sharpening factor (δ_2). Additionally, the PDF was damped by a spherical characteristic function γ to simulate the effect of finite-sized nanocrystallites.

Description of the PDF Method

The PDF method is a total scattering technique for determining local order in nanostructured materials.[49] The technique does not require periodicity, so it is well suited for studying nanoscale features in a variety of materials.[50,51] The experimental PDF, denoted $G(r)$, is the truncated Fourier transform of the total scattering structure function, $F(Q) = Q[S(Q) - 1]$: [52]

$$G(r) = \frac{2}{\pi}\int_{Q_{min}}^{Q_{max}} F(Q)\, sin(Qr)\, dQ, \quad (1)$$

where Q is the magnitude of the scattering momentum. The structure function, $S(Q)$, is extracted from the Bragg and diffuse components of X-ray, neutron or electron powder diffraction intensity. For elastic scattering, $Q = 4\pi \sin(\theta)/\lambda$, where λ is the scattering wavelength and 2θ is the scattering angle. In practice, values of Q_{min} and Q_{max} are determined by the experimental setup, and Q_{max} is often reduced below the experimental maximum to eliminate noisy data from the PDF since the signal to noise ratio becomes unfavorable in the high-Q region.

Once the experimental PDFs are determined, they can be analyzed directly or through modeling. A powerful approach is simply to compare experimentally determined PDFs from samples under study and from known control samples.[53] A great deal can be learned simply from visual inspection and by taking differences to look for residual signals. Numerical tools that compare the likeness, or degree of correlation, between two curves also give insight.[53, 54] The Pearson correlation coefficient is one such tool.[54]

The PDF gives the scaled probability of finding two atoms in a material a distance r apart and is related to the density of atom pairs in the material.[49] For a macroscopic scatterer, $G(r)$ can be calculated from a known structure model according to

$$G(r) = 4\pi r[\rho(r) - \rho_0],$$

$$\rho(r) = \frac{1}{4\pi r^2 N}\sum_i \sum_{j\neq i} \frac{b_i b_j}{<b>^2}\delta\big(r - r_{ij}\big). \quad (2)$$

Here, ρ_0 is the atomic number density of the material and $\rho(r)$ is the atomic pair density, which is the mean weighted density of neighbor atoms at distance r from an atom at the origin. The sums in $\rho(r)$ run over all atoms in the sample, b_i is the scattering factor of atom i, $<b>$ is the average scattering factor, and r_{ij} is the distance between atoms i and j.

In practice, we use Eqn. 2 to fit the PDF generated from a structure model to a PDF determined from experiment. For this purpose, the delta functions in Eqn. 2 are Gaussian-broadened and the equation is modified to account for experimental effects. PDF modeling, where it is carried out, is performed by adjusting the parameters of the structure model, such as the lattice constants, atom positions and anisotropic atomic displacement parameters, to maximize the agreement between the theoretical and an experimental PDF. This procedure is implemented, for example, in PDF_{GUI}[55] and Diffy-CMI.[48]

PDF Modeling Results

The normalized intensity (background-subtracted) of crystalline and molten $Co(bba)_3[CoCl_4]$ are shown in Figure S36. The high-temperature solid data was obtained by heating the crystalline powder to a cryostream set point of 138 °C, while the molten phase data was obtained by heating the pre-melted sample to a cryostream set point of 188 °C. Since it was not possible to directly measure the sample temperature inside the flame-sealed capillaries, melting was confirmed both visually and by the disappearance of sharp Bragg diffraction peaks. Specifically, the $I(Q)$ plot of the molten phase shows broad peaks, compared to the sharp Bragg peaks in the $I(Q)$ plot of the crystalline solid, which is indicative of full conversion into the liquid state.

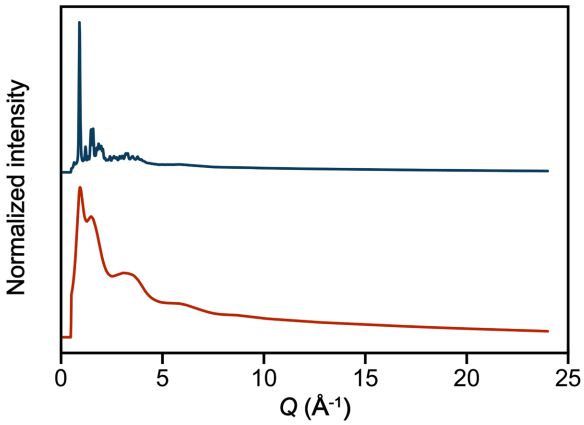

Figure S36. Normalized $I(Q)$ (background subtracted) of high-temperature solid measured at T = 138 °C (top, teal line) and liquid measured at T = 188 °C (bottom, dark red line) for $Co(bba)_3[CoCl_4]$.

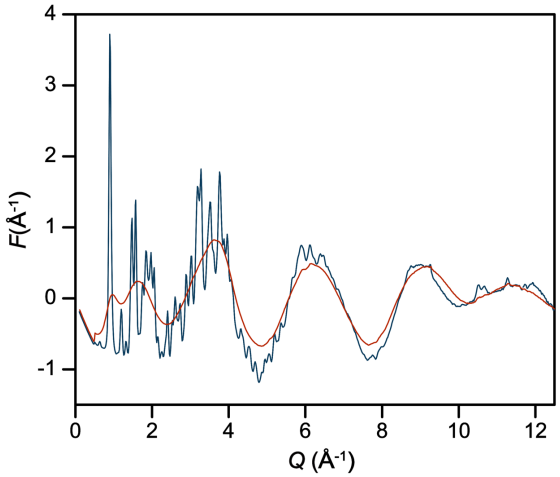

Figure S37. Total scattering reduced form functions ($F(Q)$) of high-temperature solid (teal line) and liquid (dark red line) phases of $Co(bba)_3[CoCl_4]$, with the first sharp diffraction peak (FSDP) at 0.98 $Å^{-1}$ for the liquid and 0.91 $Å^{-1}$ for the high-temperature solid.

The PDFs of crystalline and molten $Co(bba)_3[CoCl_4]$, which is Fourier transformed from the total scattering reduced form functions, $F(Q)$ (Figure S37), are shown in Figure S38a and S38b, respectively. Zoomed-in comparisons of PDF plots at short- and intermediate-range length scales are shown in Figure S39 and S40. In the range of $0 < r < 5.0$ Å (Figure S39), both the PDF of the

liquid and the solid phases share common sharp features that can be attributed to the C–C, C–N, C–O bonds in the bba ligands (~1.4 Å), Co–O coordination bond in the network (2.1 Å), Co–Cl bond in the counteranion (2.3 Å), and Cl–Cl distances (3.7 Å). Because of the similarity in bond lengths of Co–O (2.1 Å) and Co–Cl (2.3 Å) and the much higher electron density of the latter, the two features are not well resolved. The Co–O peak is, however, evident as a subtle shoulder on the low-*r* side of the Co–Cl peak in the solid state. In the liquid state, the two peaks can be more easily resolved as the Co–O peak shifts slightly lower to 2.0 Å, which is consistent with EXAFS results that show a small contraction in the average Co–O bond length as the average coordination number decreases slightly upon melting (Table S23). The similar sharpness and intensity of peak features between 0–5.0 Å in both solid and liquid phases indicates well-preserved local ordering upon melting.

Beyond short-range ordering, the PDF of the solid contains many sharp features up to 80 Å, but the PDF of the liquid phase shows much broader peaks with decreasing intensity with increasing *r*. This is consistent with the formation of a liquid phase with significantly less intermediate and long-range order compared to the solid phase. Residual ordering on these length scales, however, is still evident. Specifically, the total scattering reduced form function ($F(Q)$) plot shows a clear first sharp diffraction peak (FSDP) at 0.98 $Å^{-1}$ in the liquid state (Figure S37). Though broadened and weaker in intensity, its position is only slightly shifted by 0.07 $Å^{-1}$ from that of the high-temperature crystalline state, which suggests a small contraction upon melting and the persistence of some degree of intermediate-range order. Moreover, the intermediate distance regime of the liquid PDF ($5 < r < 30$ Å) contains broad features centered at 8.4 Å and 14.3 Å (Figure S40), which are consistent with nearest and 2nd nearest neighbor Co–Co distances in the parent crystalline structure (Table S25). Importantly, the high-*r* region of the liquid PDF exhibits quasiperiodic oscillations that extend to at least 80 Å. These oscillations are particularly evident when the curve is plotted on an expanded $G(r)$ scale as in the inset of Figure S38b. This is not seen in conventional molecular liquids, which lose all structural correlations by ~10–15 Å,[56,57] and is indicative of extended-range order within this coordination network-forming liquid.

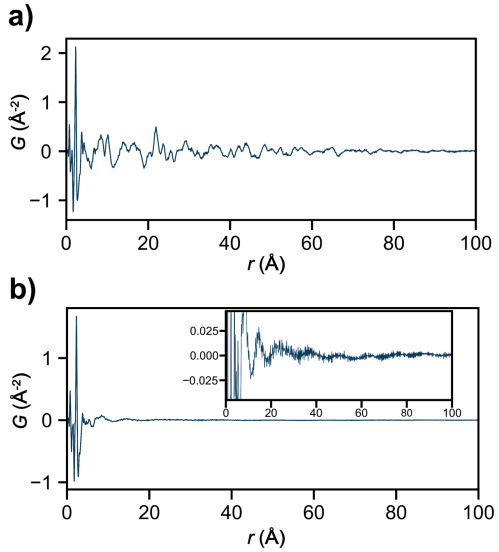

Figure S38. PDF of a) high-temperature solid and b) liquid of $Co(bba)_3[CoCl_4]$. Inset: Expanded view of the PDF between $-0.05 \leq G(r) \leq 0.05$ to highlight oscillations indicative of extended-range order in the liquid.

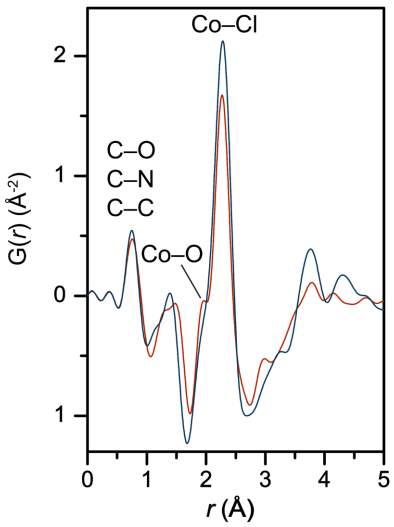

Figure S39. PDF comparisons of the high-temperature solid (blue) and liquid (red) phases of $Co(bba)_3[CoCl_4]$ in the range of $0 \leq r \leq 5$ Å with important peak features assigned.

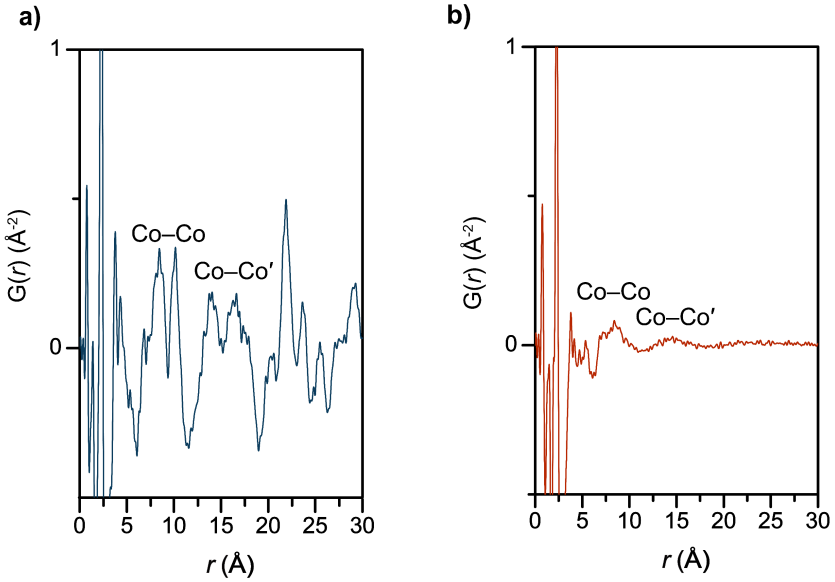

Figure. S40. PDF comparisons of high-temperature solid (blue) and liquid (red) of $Co(bba)_3[CoCl_4]$ in the range of $0 \leq r \leq 30$ Å with correlations that are consistent with nearest neighboring and second nearest neighboring (′) Co–Co distances in the crystal structure indicated.

Table S25.Unique crystallographic distances between nearest and second nearest neighboring Co centers in crystalline solid state of $Co(bba)_3[CoCl_4]$, with Co(+) denotes Co centers in the cationic coordination network and Co(−) denotes Co centers in the $[CoCl_4]^{2-}$ counteranion.

	Nearest Co–Co neighbors		2nd Nearest Co–Co neighbors	
Entry	Description	Distance (Å)	Description	Distance (Å)
1	Co(+)–Co(+)	9.68	Co(+)–Co(+)	13.70
2	Co(+)–Co(−)	7.62	Co(+)–Co(+)	16.77
3	Co(+)–Co(−)	8.16	Co(+)–Co(−)	15.40
4	Co(+)–Co(−)	8.67	Co(+)–Co(−)	15.67
5	Co(+)–Co(−)	9.51	Co(+)–Co(−)	15.94
6			Co(+)–Co(−)	16.21
7			Co(+)–Co(−)	16.47
8			Co(+)–Co(−)	16.73

Fitting of the experimental PDF was carried out to further confirm the structure of the metal–organic network. In the crystal structure of $Co(bba)_3[CoCl_4]$, the bba ligand is disordered over 2 sets of positions, A and B. For the low r range ($1.0 \leq r \leq 6.0$ Å), a molecular model was used in the fitting with molecular components extracted from the crystal structure in three different ways (Figure S41):

(a) A core of octahedral Co coordinated by 6 O atoms, disordered parts A and B of the bba ligand, and the tetrahedral $[CoCl_4]^{2-}$ anion. The PDF of these separate components were incoherently added together as follows: $G_{oct}+3(x_A G_{bba,A})+3(x_B G_{bba,B})+G_{CoCl4}$. The coefficients of 1, 3 and 1 come from the stoichiometry, and x_A and x_B are the fractions of A and B disorder parts, respectively. The values of x_A and x_B were refined in the fitting.

(b) A single octahedral Co center coordinated to 6 bba ligands, along with the $[CoCl_4]^{2-}$ anions arranged in a simple cube. The PDF of the complex with bba ligands in disordered part A and B were incoherently added together in the ratio of x_A A and x_B B.

(c) Starting from the same structure in (b), adding additional octahedral Co centers connected to the center Co center by bba ligands. The PDF of the structural chunk with bba ligands in disordered part A and B were incoherently added together in the ratio of x_A A and x_B B.

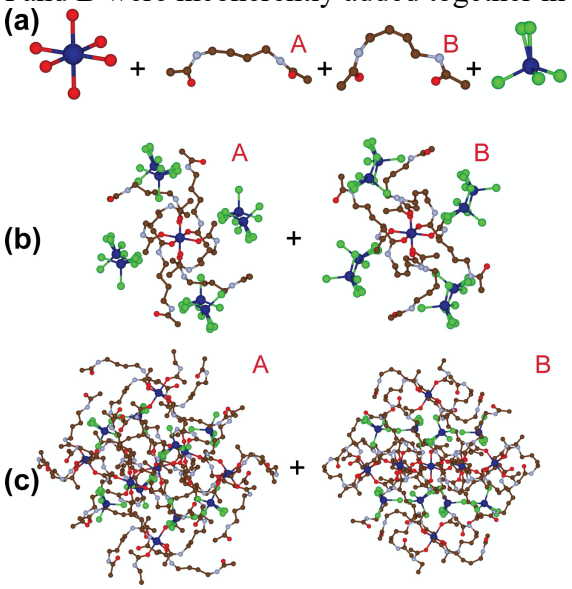

Figure S41. Structural models (a), (b), and (c) used in fitting of low-r region of $Co(bba)_3[CoCl_4]$. A and B corresponds to the two disordered parts of the bba ligand. Blue, red, light gray, brow, and green spheres represent Co, O, N, C, and Cl atoms, respectively.

The results of the fit for the high-temperature solid phase of the metal–organic network are shown in Figure S42. The model with the best fit was model (c) with the bigger chunk of coordination network, with R_w = 0.25, followed by the separate components model (a), with R_w = 0.26. Both model (a) and (c) fit well in the region of 1.0 < r < 4.0 Å, since they both consider C–C, C–N, C–O bonds of the bba ligand at ~1.4 Å, Co–O bonds of the coordination octahedra at 2.1 Å, Co–Cl bonds at 2.3 Å, and the Cl–Cl distance at 3.7 Å. However, between 4.0 and 6.0 Å, model (c) fitted better since this region contains distances between the framework Co centers and other atoms besides the O atom in the bba ligands (i.e., C and N atoms that are further away from the Co centers), which are not contained in the separated components in model (a). As a result, model (c) nicely fits the peaks both at r = 4.3 Å and r = 5.3 Å, corresponding to the Co–N and Co–C distance, respectively, while model (a) fails to do so.

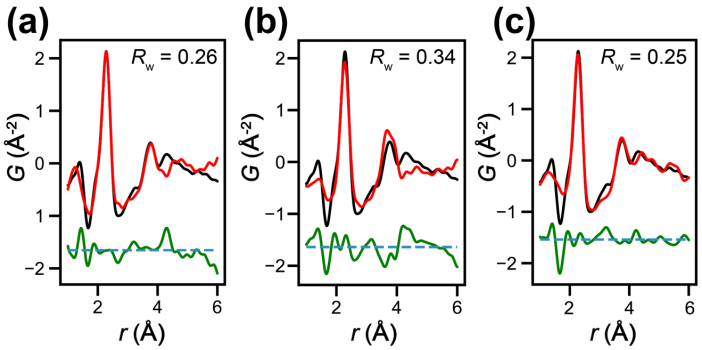

Figure S42. Fitted results for low r region of the PDF of solid $Co(bba)_3[CoCl_4]$ just below its melting temperature with three structural models (a), (b), and (c). Experimental data, calculated PDF, and the difference between them are represented by black, red, and green solid lines, respectively. Blue dotted line corresponds to a theoretical zero-difference line.

The same models are used to fit the PDF of liquid phase, and results are shown in Figure S43. For the liquid phase, model (a) fitted the best among the three models, with R_w = 0.24, as it still nicely captures the main sharp features within the region of 1.0 < r < 4.0 Å. Since model (a) considers M–O coordination octahedra, as well as individual ligands and counteranions, this result is consistent with minimal changes in connectivity around Co centers upon melting. All models seem to fit more poorly in the intermediate range (r > 4.0 Å), where decreases in intermediate-range order are expected in the liquid phase. Model (c), which contains a larger portion of the coordination network through the inclusion of multiple octahedral Co centers, still predicts the intermediate-range peaks at the correct distances as before, while model (a), which only contains a single octahedral Co center, fails to do so. For both the liquid and solid phases, model (b) fits the worst among the three models. In particular, model (b) fits the Cl–Cl distances at 3.8 Å poorly, which can be attributed to the fact that model (b) contains 8 counteranions surrounding only one octahedral complex, overestimating the Cl–Cl peak intensity.

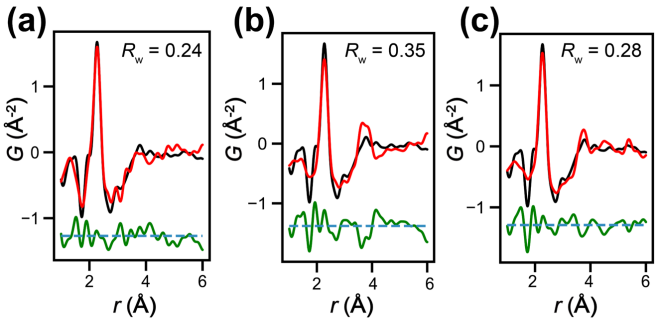

Figure S43. Fitted results for low *r* region of the PDF of liquid $Co(bba)_3[CoCl_4]$ with three structural models (a), (b), and (c). Experimental data, calculated PDF, and the difference between them are represented by black, red, and green solid lines, respectively. Blue dotted line corresponds to a theoretical zero-difference line.

For the high-*r* range, we used a crystal model to fit the solid-state data, and the results are shown in Figure S44 . Major features of the regions are the sharp peak at r = 8.6 Å, corresponding to the Co–Co distance between the octahedral Co centers and the Co atoms in the counteranions, with the Co–Co distance between nearest neighboring Co centers in the coordination network (9.7 Å) appearing as a shoulder. Additional sharp peaks at 13.7 Å and 16.7 Å correspond to the Co–Co distance between the face and body diagonal Co centers in the coordination network, as well as the Co–Co distance between network Co centers and the Co atoms in the next neighboring counteranions (Table S25). In the liquid state, broad peak features centered at similar positions are still visible, as previously discussed, despite the disappearance of majority of sharp features upon melting.

For a well-defined extended network structure, the PDF should exhibit oscillations with periods corresponding to the structural separations in different directions, overlaid with sharp features.[58] In the region r > 11 Å of the solid PDF, there appears to be oscillations with a period of roughly 9.0 Å, which is consistent with nearest neighbor Co–Co distances as discussed above. This result confirms the well-defined extended structure of the solid metal–organic network is maintained at high temperatures. For the liquid, the oscillations present at r > 11 Å extend out beyond 80 Å, but due to the beamstop attenuating the data in the low-Q limit, we cannot make any further direct structural conclusions about the liquid phase. The existence of the oscillations in the high-*r* region of the PDF, however, provides strong evidence that there are density modulations in the liquid, presumably due to partial preservation of the underlying network structure of the crystalline state. Since the period of the oscillations is affected by the beamstop cutoff more than the intrinsic low-Q information that has been lost, it is not possible to infer quantitative information from the periodicity of the oscillations.

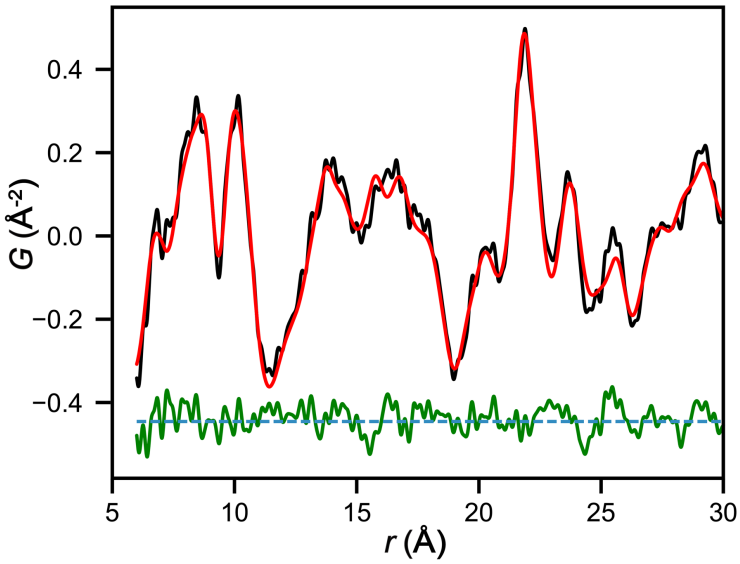

Figure S44. Fitted results for high-*r* region of the PDF of $Co(bba)_3[CoCl_4]$ just below the melting temperature. R_w = 0.18. Experimental data, calculated PDF, and the difference between them are represented by black, red, and green solid lines, respectively. Blue dotted line corresponds to a theoretical zero-difference line.

Variable-Temperature Viscosity Measurements

An electromagnetically spinning viscometer (EMS-1000S) by Kyoto Electronics Manufacturing Co. LTD was used to measure variable-temperature viscosities. Specifically, 200–300 mg of sample was placed in a glass tube with a 2-mm-diameter aluminum ball sitting at the bottom, and each sample was heated to just above its respective melting temperature. During the measurement, the aluminum ball was set to rotate with an input frequency of 1000 Hz. Rotation of the aluminum ball is traced by a red laser, and the viscosity was determined by the reduction in rotational speed. Each measurement was repeated 5–10 times at a given temperature, and the average is reported as the measured viscosity. Standard deviations from multiple measurements are typically < 2 %.

When deviating from an Arrhenius relation ($\eta(T) = \eta_0 \exp\left(\frac{E_a}{RT}\right)$), where E_a is activation energy of the viscous flow and R is the ideal gas constant, the temperature dependence of liquid viscosities can be described by models such as the VFT equation ($\log\eta(T) = \log\eta_\infty + \frac{B}{T-T_0}$) and the MYEGA equation ($\log\eta(T) = \log\eta_\infty + \frac{K}{T}\exp\left(\frac{C}{T}\right)$), where η_∞ is the high temperature asymptote, T_0 is the ideal glass transition temperature where entropy of glass equals the entropy of crystal, and B, K, C are temperature-independent constant. While the VFT equation predicts a viscosity divergence at T_0, MYEGA predicts continuous viscosity change as temperature decreases and has been experimentally considered to yield more physical viscosities when extrapolated to low and high temperature limit.[59,60] Here, the viscosity data of $Co(hmba)_3[CoBr_4]$ is modeled by Arrhenius equation, the VFT equation, and the MYEGA equation (black, red, and blue lines, respectively, Figure S45). Compared to the VFT and MYEGA fits, the inadequacy of the linear Arrhenius fit in describing the temperature dependence of the liquid viscosity when extrapolated to $\infty < T < T_g$, suggesting E_a is temperature dependent.[38] Specifically, at $T = \infty$, both VFT and MYEGA fits yield $log\eta_\infty$ very close to the experimentally observed average obtained by fitting viscosity data of common glass-forming systems to each model,[59] while the Arrhenius fit results in significant underestimation by more than 5 order of magnitude. A similar underestimation of viscosity at the DSC-determined T_g upon cooling of 20 °C (black dotted line, Figure S45) by the Arrhenius model is observed, which should be close to 10^{12} Pa·S according to the rheological definition of a glass transition.[61] Assuming $\eta = 10^{12}$ Pa·S at T_g, the VFT equation predicts a T_g of 20 °C that is consistent with the experimental value (20 °C) while the MYEGA equation predicts a slightly lower T_g of 6 °C. However, this difference are likely due to extrapolation from a relatively narrow range of experimental data and are not a reflection on the accuracy of each model.

Just above T_m ($0.9 < T_m/T < 1.0$), the viscosities of liquid phases of all three metal–bis(acetamide) networks measured here follow a nearly Arrhenius-type temperature dependence. E_a in this temperature range is therefore calculated with Arrhenius fits and is similar for all coordination network-forming liquids (Table S26). This similarity suggests diffusion and structural relaxation in the three liquid phases are likely governed by similar set of molecular interactions right above their respective T_m. However, it is important to note that this E_a cannot sufficiently describe the entire temperature range of $\infty < T < T_g$, and it is possible that the temperature dependance of E_a may differ for each liquid, which could explain, for instance, the different crystallization kinetics of $Mn(bba)_3[MnCl_4]$ and $Co(hmba)_3[Co(NCS)_4]$.

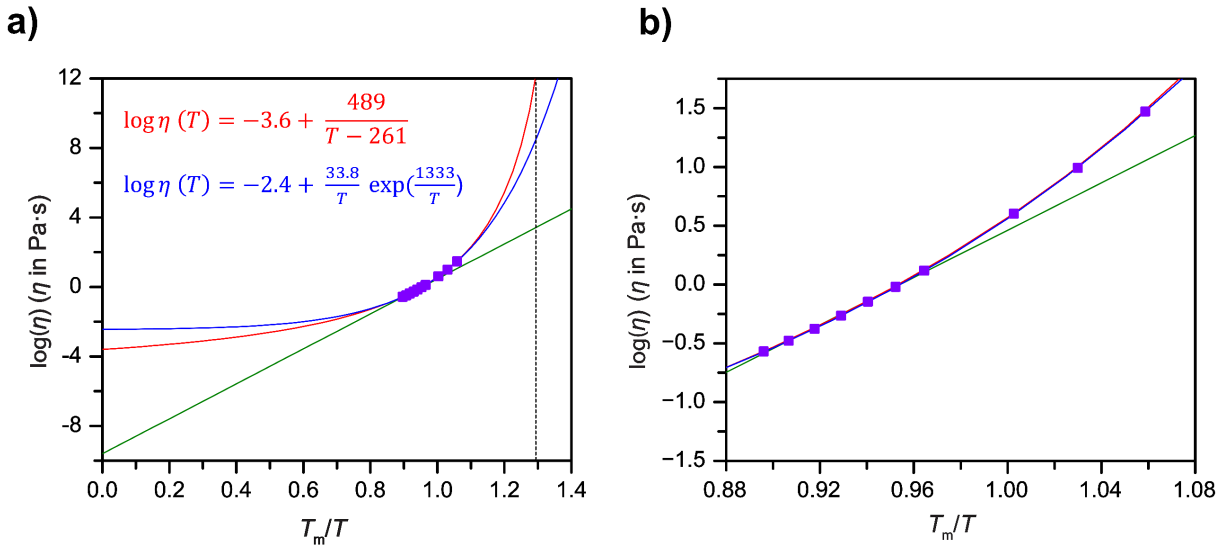

Figure S45. A comparison of the VFT fit (red), MYEGA fit (blue), and Arrhenius fits (green) to the viscosity data of $Co(hmba)_3[CoBr_4]$ (purple squares). (a) Fits extrapolated to the low and high temperature limits. VFT and MYEGA equations with respective fitting parameters are shown in red and blue, correspondingly. The vertical, dotted black line indicates the DSC determined T_g. (b) Fits in the temperature range ($0.88 < T_m/T < 1.08$) over which viscosity data is measured. Both VFT and MYEGA give equally high-quality fits ($r^2 > 0.99$).

Table S26. Summary of E_a at $0.9 < T_m/T < 1.0$ for liquid phases of the three metal–bis(acetamide) networks as determined from Arrhenius fits. Data for the pure hmba and bba ligands is included for comparison.

Compound	***E*$_a$ (kJ/mol)** ($0.9 < T_m/T < 1.0$)
$Co(hmba)_3[CoBr_4]$	77.0 ± 1.3
$Co(hmba)_3[Co(NCS)_4]$	60.0 ± 2.4
$Mn(bba)_3[MnCl_4]$	71.5 ± 4.2
hmba	38.1 ± 0.3
bba	38.5 ± 1.4

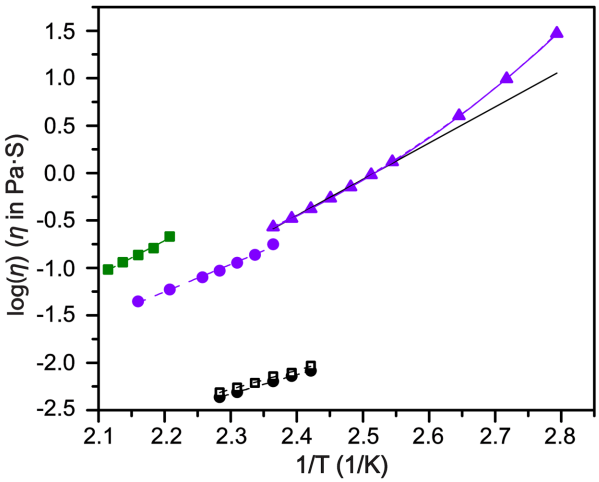

Figure S46. Viscosity data for pure hmba (black circles), pure bba (black squares), $Mn(bba)_3[MnCl_4]$ (green squares), $Co(hmba)_3[Co(NCS)_4]$ (purple circles), and $Co(hmba)_3[CoBr_4]$ (purple triangles) is shown on an absolute temperature scale. The purple dashed and solid lines correspond to the VFT fit for $Co(hmba)_3[CoBr_4]$, respectively, while the solid black line is an Arrhenius fit. For other liquids, Arrhenius fits are plotted as dashed lines.

Table S27. Comparison of the viscosities of the metal–organic liquids reported here to conventional ionic liquids at similar measurement temperatures. The liquid phases of metal–bis(acetamide) networks studied here have significantly higher viscosities, which is indicative of slower structural relaxation and consistent with a more structured liquid.[62]

Compound[a]	Viscosity (mPa·S)	T(K)	Ref
$Co(hmba)_3[Co(NCS)_4]$	178	423	this study
$Co(hmba)_3[CoBr_4]$	270	423	this study
$Mn(bba)_3[MnCl_4]$	214	453	this study
hmba	6.4	423	this study
bba	7.2	423	this study
[bmmim][BF_4]	66	343	62
[bmim][PF_6]	45	343	62
[bmim][BF_4]	24	343	62
[bmmim] [Tf_2N]	22	343	62
[SEt_3] [Tf_2N]	11	343	62
[bmpyr][Tf_2N]	10.7	450	63
[bmim][Pf_2N]	7.86	450	63
[bmim][Tf_2N]	4.69	450	63
[hmim][Tf_2N]	3.83	430	64

[a]bmmim = 1-butyl-2,3-dimethylimidazolium, bmim = 1-butyl-3-methylimidazolium, Tf_2N = bis(trifluoromethylsulfonyl)imide; SEt_3 = triethylsulfonium; bmpyr = 1-butyl-1-methylpyrrolidiunium; Pf_2N = bis(perfluoroethylsulfonyl)imide; hmim = 1-hexyl-3-methylimidazolium.

Table S28. Comparison of the viscosities metal–organic liquids reported here to select glass-forming ionic liquids near T_m. The coordination network-forming liquids have comparable or higher viscosity near T_m, indicative of their high glass-forming ability.

Compound[a]	Viscosity (mPa·S)	T (K)	T_m (K)	Ref
$Co(hmba)_3[Co(NCS)_4]$	178	423	417	this study
$Co(hmba)_3[CoBr_4]$	1313	393	379	this study
$Mn(bba)_3[MnCl_4]$	214	453	445	this study
$[bmmim][BF_4]$	84	283	271	62, 65
$[bmim][PF_6]$	231	288	284	62, 65
$[bmim][BF_4]$	164	313	310	62, 65

Fourier-Transformed Infrared Spectroscopy (FTIR)

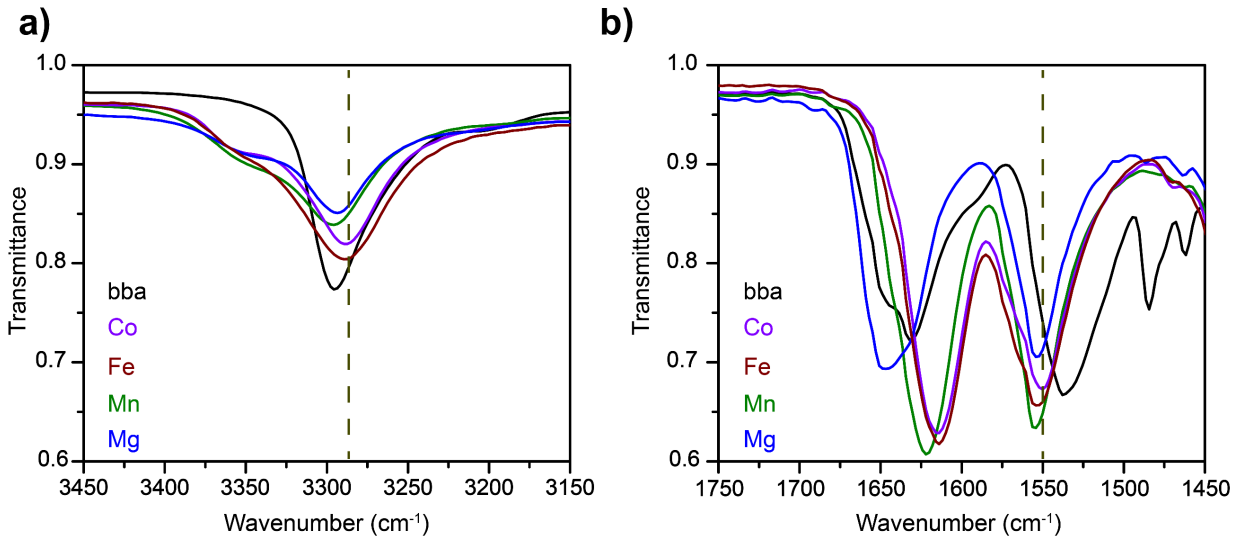

Figure S47. FTIR spectra for the bba ligand (black), $Co(bba)_3[CoCl_4]$ (purple), $Fe(bba)_3[FeCl_4]$ (dark red), $Mn(bba)_3[MnCl_4]$ (green), and $Mg(bba)_3[CoCl_4]$ (blue). Both $Co(bba)_3[CoCl_4]$ and $Fe(bba)_3[FeCl_4]$ have more red-shifted peaks for a) N-H stretch relative to Mn and Mg analogs, while $Co(bba)_3[CoCl_4]$ has the most red-shifted peak for b) N-H bend as highlighted with the gray dashed lines.

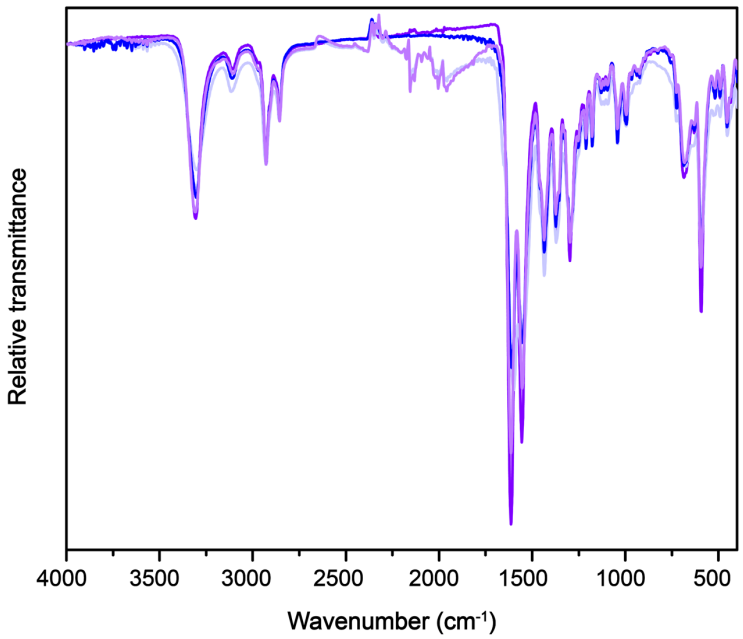

Figure S48. Variable temperature FTIR spectra of $Co(hmba)_3[CoBr_4]$. The transmittance of all spectra were normalized to the C-H stretch at 2928 cm^{-1}. Spectra were taken while heating from ambient temperature (dark purple) to 95 °C (11 °C below T_m; purple) and 118 °C (12 °C above T_m; light purple). The melt was then cooled to 40 °C, and the spectrum of the resulting supercooled liquid is shown in blue. The consistency of peak positions suggests that hydrogen bonding interactions in the solid state are largely preserved in the liquid and supercooled liquid state.

NMR Spectra

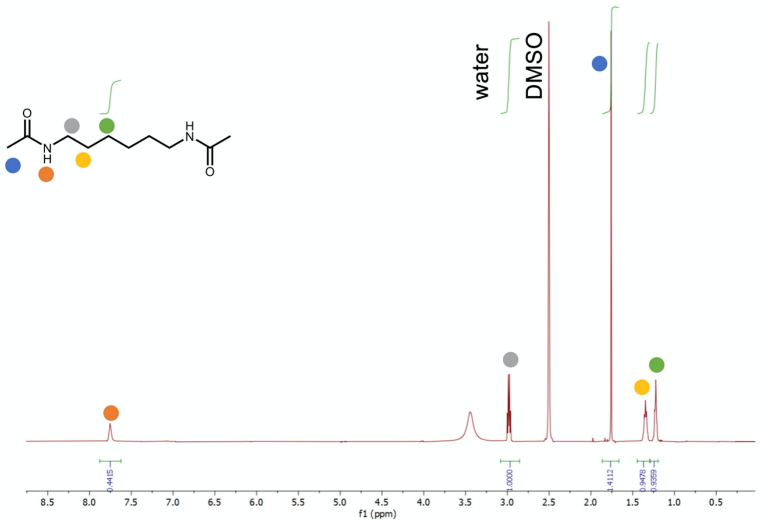

Figure S49. ^{1}H NMR spectrum in DMSO-d_6 of $Co(hmba)_3[CoBr_4]$ after storage at ambient temperature for 1-2 weeks. Only hmba signals are detected, indicating that all lattice solvent has been released.

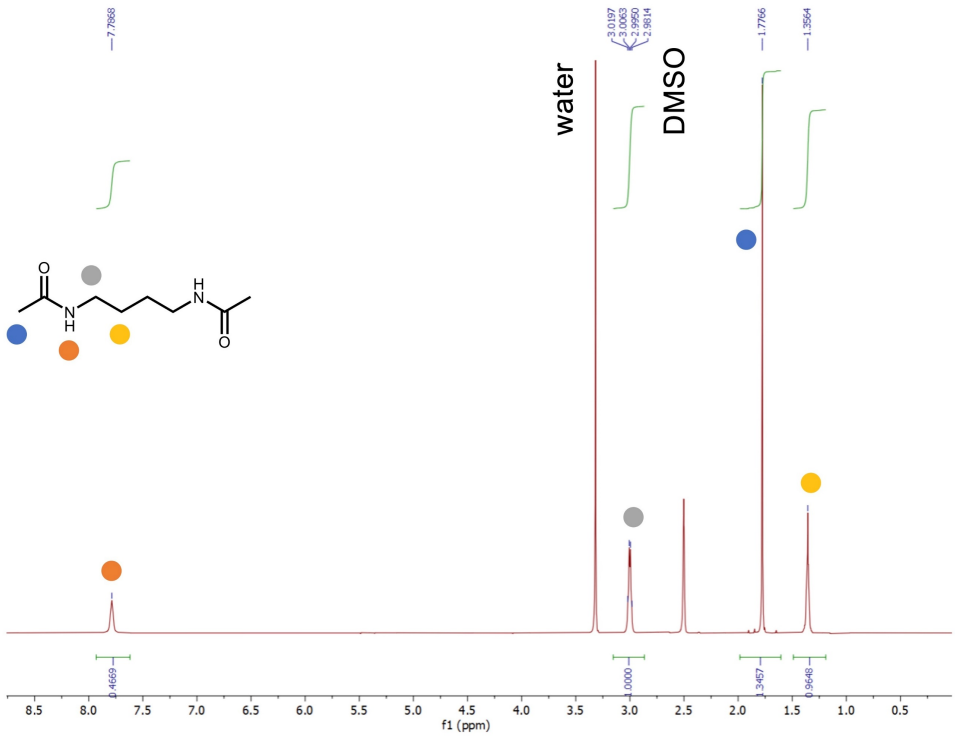

Figure S50. ^{1}H NMR spectrum in DMSO-d_6 of *N*,*N*′-1,4-butylenebis(acetamide) (bba).

References

(1) Li, Q.; Wang, P.; Deng, Y. Amide Exchange Reaction: A Simple and Efficient CuO Catalyst for Diacetamide Synthesis. *RSC. Adv*. **2016**. *6*. 40890–40894.

(2) Chatterton, N. P.; Goodgame, D. M. L.; Grachvogel, D. A.; Hussain, I.; White, A. J. P.; Williams, D. J. Influence of the Counteranion on the Formation of Polymeric Networks by Metal Complexes of Hexamethylenebis(acetamide). *Inorg. Chem*. **2001**, *40*, 312–317.

(3) Goodgame, D. M. L.; Grachvogel, D. A.; Hussain, I.; White, A. J. P.; Williams, D. J. Formation of Polymeric Network Arrays by Complexes of Manganese(II) or Cobalt (II) with Alkane Chain Linked Bis(amide) Ligands of Biological Relevance. *Inorg. Chem.* **1999**, *38*, 2057–2063.

(4) Bruker Analytical X-ray Systems. *SAINT and APEXT 2 Software for CCD Diffractometers* (2000).

(5) Sheldrick, G. M. SHELXT – Integrated Space-Group and Crystal-Structure Determination. *Acta. Crystallogr. Sect. Found Adv.* **2015**, *71*, 3–8.

(6) Sheldrick, G. M. A Short History of SHELX. *Acta. Crystallogr. Sect. Found Crystallogr.* **2008**, *64*, 112–122.

(7) Sheldrick, G. M. Crystal Structure Refinement with SHELXL. *Acta. Crystallogr. Sect. C Struct. Chem.* **2015**, *71*, 3–8.

(8) Dolomanov, O. V.; Bourhis, L. J.; Gildea, R. J.; Howard, J. A. K.; Puschmann, H. OLEX2: A Complete Structure Solution, Refinement and Analysis Program. *J Appl Crystal.* **2009**, *42*, 339–341.

(9) (a) Yalkowsky, S. H. Estimation of Entropies of Fusion of Organic Compounds. *Ind. Eng. Chem. Fundam.* **1979**, *18*, 108–111.

(10) Jain, A.; Yang, G.; Yalkowsky, S. H. Estimation of Melting Points of Organic Compounds. *Ind. Eng. Chem. Res.* **2004**, *43*, 7618–7621.

(11) An *Introduction to Hydrogen bondin*g, Jeffrey, G. A. Oxford University Press: Oxford, 1997.

(12) Wildner, M. On the Geometry of Co(II)O_6 Polyhedra in Inorganic Compounds. *Z. Kristallogr. Cryst. Mater.* **1992**, *202*, 51–70.

(13) Harding, M. M. The Geometry of Metal–Ligand Interactions Relevant to Proteins. II. Angles at the Metal Atom, Additional Weak Metal–Donor Interactions. *Acta Cryst.* **2000**, *D56*, 857–867.

(14) Brügi, H. B.; Dunitz, J. D. From Crystal Statics to Chemical Dynamics. *Acc. Chem. Res.* **1983**, *16*, 153–161.

(15) Gallagher, T.; Alexander, P.; Bryan, P.; Gilliland, G. L. Two Crystal Structures of the B1 Immunoglobulin-binding Domain of Streptococcal Protein G and Comparison with NMR. *Biochemistry*, **1994**, *33*, 4721–4729.

(16) Coelho, A. Indexing of Powder Diffraction Patterns by Interactive Use of Single Value Decomposition. *J. Appl. Crystallogr.* **2003**, *36*, 86–95.

(17) Coelho, A. *TOPAS-Academic*, version 4.1; Coelho Software: Brisbane, Australia, 2007.

(18) Bennett, T. D.; Tan, J-C.; Yue, Y.; Baxter, E.; Ducati, C.; Terrill, N. J.; Yeung, H. H. -M.; Zhou, Z.; Chen, W.; Henke, S.; Cheetham, A. K.; Greaves, G. N. Hybrid Glasses from Strong and Fragile Metal–Organic Framework liquids. *Nat. Commun.* **2015**, *6*, 8079

(19) Bennett, T. D.; Yue, Y.; Li, P.; Qiao, A.; Tao, H.; Greaves, N. G.; Richards, T.; Lampronti, G. I.; Redfern, S. A. T.; Blanc, F.; Farha, O. K.; Hupp, J. T.; Cheetham, A. K.; Keen, D. A. Melt-Quenched Glasses of Metal–Organic Frameworks. *J. Am. Chem. Soc.* **2016**, *138*, 3484–3492.

(20) Zhou, C.; Longley, L.; Krajnc, A.; Smales, G. J.; Qiao, A.; Erucar, I.; Doherty, C. M.; Thornton, A. W.; Hill, A. J.; Ashling, C. W.; Qazvini, O. T.; Lee, S. J.; Chater, P. A.; Terrill, N. J.; Smith, A. J.; Yue, Y.; Mail, G.; Keen, D. A.; Telfer, S. G.; Bennett, T. D. Metal–Organic Frameworks Glasses with Permanent Accessible Porosity. *Nat. Commun*., **2018**, *9*, 5042.

(21) Widmer, R. N. W., Lampronti, G. I.; Anzellini, S.; Gaillac, R.; Farsang, S.; Zhou, C.; Belenguer, A. M.; Palmer, H.; Kleppe, A. K.; Wharmby, M. T.; Redfern, S. A.; Coudert, F-X.; MacLeod, S.

G.; Bennett, T. Pressure Promoted Low-Temperature of Metal–Organic Frameworks. *Nat. Mater.*, **2019**, *18*, 370–360.

(22) Frentzel-Beyme, L.; Kloß, M.; Kolodzeiski, P.; Pallach, R.; Henke, S. Meltable Mixed-Linker Zeolitic Imidazolate Frameworks and Their Microporous Glasses: From Melting Point Engineering to Selective Hydrocarbon Sorption. *J. Am. Chem. Soc.* **2019**, *14131,* 12362–12371.

(23) Hou, J.; Gómez, M. L. R.; Krajnc, A.; McCaul, A.; Li, S.; Bumstead, A. M.; Sapnik, A. F.; Deng, Z.; Lin, R.; Chater, P. A.; Keeble, D. S.; Keen, D. A.; Appadoo, D.; Chan, B.; Vicki, Chen.; Mali, G.; Bennett, T. D. Halogenated Metal–Organic Framework Glasses and Liquids. *J. Am. Chem. Soc.* **2020**, *142*, 3880–3890.

(24) Das, C.; Horike, S. Crystal Melting and Vitrification Behaviors of the Three-Dimensional Nitrile-Based Metal–Organic Framework. *Faraday Discuss*, **2021**, Advanced Article, 10.1039/D0FD00003E.

(25) Kimata, H.; Mochida, T. Crystal Structures and Melting Behaviors of 2D and 3D Anionic Coordination Polymers Containing Organometallic Ionic Liquid Components. *Chem. Eur. J.*, **2019**, *25*, 10111–10117.

(26) Nagarkar, S. S.; Kurasho, H.; Duong, N. T.; Nishiyama, Y.; Kitagawa, S.; Horike, S. Crystal Melting and Glass Formation in Copper Thiocyanate Based Coordination Polymers. *Chem. Commun*. **2019**, *55*, 5455–5458.

(27) Umeyama, D.; Horike, S.; Inukai, M.; Itakura, T.; Kitagawa, S. Reversible Solid-to-Liquid Phase Transition of Coordination Polymer Crystals. *J. Am. Chem. Soc*. **2015**, *137*, 864–870.

(28) Das, C.; Ogawa, T.; Horike, S. Stable Melt Formation of 2D Nitrile-Based Coordination Polymer and Hierarchical Crystal–Glass Structuring. *Chem. Commun.* **2020**, *56*, 8980–8983.

(29) Inukai, M.; Nishiyama, Y.; Honjo, K.; Das, C.; Kitagawa, S.; Horike, S. Glass-Phase Coordination Polymer Displaying Proton Conductivity and Guest-Accessible Porosity. *Chem. Commun.*, **2019**, *55*, 8528–8531.

(30) Prananto, Y. P. Coordination Polymer of M(II)-Pyrazinamide (M = Co, Cd) with Double End-to-End Thiocyanate Bridge. IOP. Conf. Ser.: Mater. Sci. Eng. **2018**, *299*, 012032

(31) Bumstead, A. M. ; Thorne, M. F.; Bennett, T. D. Identifying the Liquid and Glassy States of Coordination Polymers and Metal–Organic Frameworks. *Faraday Discuss.* **2020**, DOI: 10.1039/d0fd00011f.

(32) Su, Y-J.; Cui, Y-L.; Wang, Y.; Lin, R-B.; Zhang, W-X.; Zhang, J-P.; Chen, X-M. Copper(I) 2-Isopropoylimidazolaye: Supramolecular Isomerism, Isomerization, and Luminescent Properties. *Cryst. Growth Des.*, **2015**, *15*, 1735–1739.

(33) Spielberg, E. T.; Edengeiser, E.; Mallick, B.; Havenith, M.; Mudring, A-V. (1-Butyl-4-methyl-pyridium)[$Cu(SCN)_2$]: A Coordination Polymer and Ionic Liquid. *Chem. Eur. J.* **2014**, *20*, 5338–5345.

(34) Alexandru, M-G.; Jitaru, I.; Madalan, A. M.; Andruh, M.; Aggregation of Two Different Coordination Polymers by Reacting Zinc Nitrate and Cadmium Chloride with N, N'–Ethylenebisacetamide, *J. Coord. Chem.*, **2011**, *64*, 3333–3341.

(35) Höhne, G.; Hemminger, W.; Flammersheim, H. J. *Differential Scanning Calorimetry*; Springer Verlag: Berlin, Germany, 1996.

(36) Gabbott, P. A Practical Introduction to Differential Scanning Calorimetry, In *Principles and Applications of Thermal Analysis*; Gabbott P. A. Ed.; Blackwell Publishing Ltd: Oxford, 2008; pp. 1–50.

(37) McGillicuddy, R. D.; Thapa, S.; Wenny, M. B.; Gonzalez, M. I.; Mason, J. A. Metal–Organic Phase-Change Materials for Thermal Energy Storage. *J. Am. Chem. Soc.* **2020**, *142*, 19170–19780.

(38) Greaves, G. N.; Sen, S. Inorganic Glasses, Glass-forming Liquids and Amorphizing Solids, *Adv. Phys.* **2007**, *56*, 1–166.

(39) Ravel, B.; Newville, M. ATHENA, ARTEMIS, HEPHAESTUS: Data analysis for X-ray absorption spectroscopy using IFEFFIT. *J. Synchrotron Radiat.* **2005**, *12*, 537–541.
(40) Zabinsky, S. I.; Rehr, S. I.; Ankudinov, A.; Albers, S. I.; Eller, M. J. Multiple-Scattering Calculations of X-Ray-Absorption Spectra. *Phys. Rev. B.* **1995**, *52*, 2995–3009.
(41) Understanding the Quick First Shell Tool in Artemis, bruceravel.github.i/demeter/artug/extended/qfs.html (accessed 10/10/2020).
(42) Newville, M. Fundamentals of XAFS. *Rev. Mineral. Geochem.* **2014**, *78*, 33–74.
(43) Kelly, S. D.; Bare, S. R.; Greenlay, N.; Azevedo, G.; Balasubramanian, M.; Barton, D.; Chattopadhyay, S.; Fakra, S.; Johannessen, B.; Newville, M.; Pena, J.; Pokrovski, G. S.; Proux, O.; Priolkar, K.; Ravel, B.; Webb, S. M. Comparison of EXAFS Foil Spectra from around the World. *J. Phys.: Conf. Ser.* **2009**, *190*, 012032.
(44) Frank, P.; Benfatto, M.; Qayyam, M.; Hedman, B.; Hodgson, K. O. A High-resolution XAS Study of Aqueous Cu(II) in Liquid and Frozen Solutions: Pyramidal, Polymorphic, and Non-centrosymmetric. *J. Chem. Phys.* **2015**, *142*, 084310.
(45) Chupas, P. J.; Qiu, X.; Hanson, J. C; Lee, P. L.; Grey, C. P.; Billinge, S. J. L. Rapid-Acquisition Pair Distribution Function (RA-PDF) Analysis. *J. Appl. Crystallogr.* **2003**, *36*, 1342–1347.
(46) Yang, X.; Juhás. P.; Farrow, C. L.; Billinge, S. L. J. xPDFsuite: An End-to-End Software Solution for High Throughput Pair Distribution Function Transformation, Visualization and Analysis. 2015, arXiv:cond-mat/1402.3163. arXiv.org e-Print archive. https://arxiv.org/abs/1402.3163 (accessed Nov 3, 2020).
(47) Juhás. P.; Davis, T; Farrow, C. L.; Billinge, S. J. L. PDFgetX3: A Rapid and Highly Automatable Program for Processing Powder Diffraction Data into Total Scattering Pair Distribution Functions. *J. Appl. Crystallogr.* **2013**, *46*, 560–566.
(48) Juhás. P.; Farrow, C. L.; Yang, X.; Knox, K. R.; Billinge, S. J. L. Complex Modeling: A Strategy and Software Program for Combining Multiple Information Sources to Solve Ill Posed Structure and Nanostructure Inverse Problems. *Acta Crystallogr. A*, **2015**, *71*, 562–568.
(49) Egami, T.; Billinge, S. J. L. *Underneath the Bragg Peaks: Structural Analysis of Complex Materials*, 2nd ed.; Elsevier: Amsterdam, 2012.
(50) Billinge, S. J. L. Nanoscale Structural Order from the Atomic Pair Distribution Function (PDF): There's Plenty of Room in the Middle. *J. Solid State Chem.* **2008**, *181*, 1695–1700.
(51) Billinge, S. J. L; Kanatzidis, M. G. Beyond Crystallography: The Study of Disorder, Nanocrystallinity and Crystallographically Challenged Materials with Pair Distribution Functions. *Chem. Commun.* **2004**, 749–760.
(52) Farrow, C. J.; Billinge, S. J. Relationship Between the Atomic Pair Distribution Function and Small-Angle Scattering: Implications for Modeling of Nanoparticles. *Acta. Cryst.* **2009**, *A65*, 232–239.
(53) Billinge, S. J. L.; Dykhne, T.; Juhás. P.; Božin, E. S.; Taylor, R.; Florence, A. J.; Shankland, K. Characterisation of Amorphous and Nanocrystalline Molecular Materials by Total Scattering *CrystEngComm*, **2010**, *12*, 1366–1368.
(54) Dykhne, T.; Taylor., R.; Florence, A.; Billinge, S. J. L. Data Requirements for the Reliable Use of Atomic Pair Distribution Functions in Amorphous Pharmaceutical Fingerprinting. *Pharm. Res.* **2011**, *28*, 1041–1048.
(55) Farrow, C. J.; Juhás. P.; Liu, J. W.; Bryndin, D.; Božin, E. S.; Proffen, Th.; Billinge, S. J. L. PDFfit2 and PDFgui: Computer Programs for Studying Nanostructure in Crystals. *Phys: Condens. Matter* **2007**, *19*, 335219.
(56) Powles, J. G. The Structure of Molecular Liquids by Neutron Scattering. *Adv. Phys.*, **1973**, *22*, 1–56.

(57) Hanse, J-P.; McDonal, I. R. Molecular Liquids. In *Theory of Simple Liquids*, 3rd Ed.; Elsevier: Amsterdam, 2006; pp.. 341–392.
(58) Nguyen, A. I.; Allsburg, K. M. V.; Terban, M. W.; Bajdich, M.; Oktawiec, J.; Amtawong. J.; Ziegler, M. S.; Dombrowski, J. P.; Lakshmi, K. V.; Drisdell, W. S.; Yano, J.; Billinge, S. J. L.; Tilley, T. D. Stabilization of Reactive Co_4O_4 Cubane Oxygen-Evolution Catalysts with Porous Frameworks. *Proc. Natl. Acad. Sci. U.S.A.* **2019**, 116, 11630–11639.
(59) Hecksher, T.; Nielsen, A. I.; Olsen, N. B.; Dyre, J. C. Little Evidence for Dynamic Divergences in Ultraviscous Molecular Liquids. *Nat. Phys.* **2008**, 4, 737–741.
(60) Zheng, Q.; Mauro, J. C. Viscosity of Glass-Forming Systems. *J. Am. Ceram. Soc.* **2017**, *100*, 6–25.
(61) Greaves, G. N.; Sen, S. Inorganic Glasses, Glass-forming Liquids and Amorphizing Solids, *Adv. Phys.* **2007**, *56*, 1–166.
(62) Okoturo, O. O., VanderNoot, T. J. Temperature Dependence of Viscosity for Room Temperature Ionic Liquids. *J. Electroanal. Chem.* **2004**, *568*, 167–181.
(63) Liu, H.; Maginn, E.; Visser, A. E.; Bridges, N. J.; Fox, E. B., Thermal and Transport Properties of Six Ionic Liquids: An Experimental and Molecular Dynamics Study, *Ind. Eng. Chem. Res.* **2012**, *51*, 7242–7254.
(64) Kandil, M. E.; Marsh, K. N.; Goodwin, A. R. H., Measurement of the Viscosity, Density, and Electrical Conductivity of 1-Hexyl-3-methylimidazolium Bis(trifluorosulfonyl)imide at Temperatures between (288 and 433) K and Pressures below 50 MPa. *J. Chem. Eng. Data* **2007**, *52*, 2382–2387.
(65) Fredlake, C. P.; Crosthwaite, J. M.; Hert, D. G.; Aki, S. N. V. K.; Brennecke, J. F. Thermophysical Properties of Imidazolium-Based Ionic Liquids. *J. Chem. Eng. Data*, **2004**, *49*, 954–964.